# EX-VIVO BIOMIMETIC INTERFACES FOR SCREENING ENGINEERED NANOMATERIALS

By

Ying Liu

#### A DISSERTATION

Submitted to
Michigan State University
in partial fulfillment of the requirements
for the degree of

Chemical Engineering-Doctor of Philosophy

2015

#### **ABSTRACT**

## EX-VIVO BIOMIMETIC INTERFACES FOR SCREENING ENGINEERED NANOMATERIALS

By

#### Ying Liu

Engineered nanomaterials (ENM) have attractive functional properties and are increasingly being used in commercial products. However, the potential health risks induced by ENM are poorly understood and difficult to evaluate. Since the first step in ENM toxicology pathway is to interface with cell membranes to trigger biological effects, improved methods are needed to measure ENM-biomembrane interactions. Therefore, the overall objective of my doctoral dissertation is to develop robust, high throughput nano-structured biosensors, to elucidate mechanisms of surface interaction between ENM and biomembrane, to evaluate ENM kinetics and performance, to predict ENM induced health risk, and to provide guideline for bio-safety design of nano-products with desired functions.

The first generation of higher throughput interface was developed by accelerating the interface-assembly process and enhancing stability of a planar bilayer lipid membrane (pBLM). The diameter of a classical planar BLM is ~500 µm. The novel planar BLM developed for this project was fabricated on nanopores (~700 nm) drilled through silicon nitride thin film using focused ion beam lithography. Electrophysiology and electrochemical impedance spectroscopy was used to validate functionality of the nanopore pBLM. Then, transient current spikes induced by silica nanoparticles and integral conductance induced by carboxylate multi-wall carbon nanotubes, across gigaohm nanopore pBLM, were measured.

As a result, the second generation of high throughput biomimetic interface, tethered BLM on gold electrode was developed with enhanced stability and ion reservoir. Another advantage of tethered BLM is that it can be integrated onto complementary metal—oxide—semiconductor based microsystem with on-chip electrochemical detection.

Here, pore forming activities of functionalized silica nanoparticles, functionalized polystyrene nanoparticles (PNP) and functionalized polypropargyl glycolide nanoparticles (PGL) were characterized using high insulating tethered BLM. Electrical resistance trajectory was analyzed using empirical exponential model, providing dynamic information of ion leakage induced by various nanoparticles. Coupled with statistical hierarchical clustering post-analysis, the tethered BLM method could distinguish between nanoparticles based on size, charge and/or surface functional groups.

As a result, a mechanistic kinetic model was developed to predict interaction kinetics of ENM with model BLM and to assess biosensor performance. A 9 parameter model was designed using MATLAB and R, and then simplified into a 3 parameter model. The model developed helps elucidate molecular processes responsible for time-evolved electrochemical signal changes in tethered BLM. The model uses two kinetic constants to describe the rates of ENM binding to, and lipid removal from, the interface. The model was fit to membrane resistance,  $R_m$  vs. time data for interaction of a tethered BLM with two types of ENM: PGL and functionalized polystyrene nanoparticles. The model was able to predict diverse trends in the  $R_m$  vs. time data, including a continuous decrease (PNP) in  $R_m$  and an initial increase (PGL) in  $R_m$  followed by a decrease. The model also predicted that the biosensor is so sensitive that the interaction involving only  $10^{-8}\%$  of bulk nanoparticles could generate measurable changes in the biosensor output.

Copyright by YING LIU 2015 DEDICATED TO MY PARENTS

#### **ACKNOWLEDGEMENTS**

I have harvested a lot throughout the years at MSU pursuing my Ph. D degree. However, I would not have made it without the help and support of so many people. First, I would like to thank my advisor R. Mark Worden for the opportunity to join his lab, to work in a multidisciplinary team, and for his guidance and support to become an independent researcher. I would also like to thank my committee members: Scott Calabrese-Barton, S. Patrick Walton, Greg M. Swain, for their time and suggestions.

Part of this dissertation is the result of collaborative work with colleagues in our NANOGO team. Therefore, I want to thank Gregory L. Baker for the help in synthesizing customizable engineered nanoparticles, Andrew Mason for the help in designing electrode array chips, Daniel A. Jones for the help with mass spectrometry and Phillip M. Duxbury for the help in revising my manuscript.

I would also like to express my appreciation and gratitude to people who have helped me with different aspects of my research: Zhen Zhang for statistical consultancy, Kathy Welsh for the help with atomic force microscopy, Alexander Negoda for the help with planar lipid bilayer workstation, Per Askeland for training me in focused ion beam and sputter coating techniques.

Special thanks to my parents for their unconditional love, support and words of encouragement. When I am truly touched, I am wordless. But, I know I would not be where I am without my parents. Confucius said:" While his parents are alive, the son may not go abroad to a distance. If he does go abroad, he must have a fixed place to which he goes." Thank you Mom and Dad for letting your only daughter travel half the earth, and pursue her dream.

Finally, I wish to extend my sincere gratitude to all my family and friends for being there for me during the past few years.

## TABLE OF CONTENTS

LIST	Γ OF T	ΓABLES	X
LIST	Γ OF I	FIGURES	xi
KEY	TO A	ABBREVIATIONS	. XV
1.	INTR	ODUCTION	1
1.1		Aotivation and Objectives	
1.2		Research Problem Definition	
1.3		Background	
	1.3.1.		
	1.3.2.	• •	
	1.3.3.	C	
2.		INTERACTION WITH SILICA NANOPARTICLES	
2.1		Abstract	
2.2	2. I	ntroduction	. 18
2.3	3. N	Materials and Methods	. 19
	2.3.1.	Materials	
	2.3.2.	Fabrication and characterization of silica-core nanoparticles	
	2.3.3.	Preparation of liposome	
	2.3.4.	Preparation of polydimethylsiloxane (PDMS) slab	. 21
	2.3.5.	Formation of tBLM biomimetic interface	. 21
	2.3.6.	Electrochemical characterization of tBLM and ENM-BLM interaction	
	2.3.7.	Topological characterization of tBLM	. 24
	2.3.8.	Statistical analysis	
2.4	4. R	Results and Discussion	. 27
	2.4.1.	Characterization of dispersed silica-core nanoparticles prior to exposure	e to
	tBLM		. 27
	2.4.2.	Electrochemical characterization of tBLM	. 28
	2.4.3.	AFM imaging of tBLM	. 28
	2.4.4.	Surface functional group effects of silica-core nanoparticles on membra	ıne
	resista	nce of tBLM	
	2.4.5.	Effects of tBLM exposure on aggregation of silica-core nanoparticles	. 36
2.5	5. (	Conclusions	
3.	tBLM	I INTERACTION WITH PNP	. 40
3.1		Abstract	
3.2		ntroduction	
3.3	3. N	Naterials and Methods	
	3.3.1.	Characterization of functionalized PNP	. 42
	3.3.2.	Fabrication of tBLM	. 43

3.3.3.	EIS characterization of tBLM	43
3.3.4.		
3.3.5.		
3.4. F	Results	
3.4.1.		
3.4.2.		
3.4.3.		
3.4.4.		
3.4.5.	• •	
3.4.6.		
	Discussion	
	Conclusions	
0.00		0 .
4. INTI	EGRATION OF MINIATURIZED BIOSENSOR ARRAY WITH A	
<b>MULTI-C</b>	HANNEL IMPEDANCE EXTRACTION CIRCUIT	67
<b>4.1.</b> A	Abstract	67
4.2. I	ntroduction	67
	Materials and Methods	
4.3.1.	Fabrication of miniaturized electrode	70
4.3.2.	Design of fully integrated muti-channel impedance extraction circuit	chip
4.3.3.	Incorporation of gramicidin protein into tBLM biosensor array platfo	rm 71
4.3.4.	COOH MWNT interaction with tBLM biosensor array platform	71
4.4. I	Results and Discussion	72
4.4.1.	Electrochemical characterization of gramicidin ion channel incorpora	ited
bioser	nsor performance	
4.4.2.	Electrochemical characterization of tBLM-nanoparticle interaction by	y
comm	nercial potentiostat and MIED	74
4.5.	Conclusions	76
	ELOPMENT OF NANOPORE PBLM ON SILICON NITRIDE FOR	
	GATING ENM-BLM INTERACTIONS	
	Abstract	
	ntroduction	
	Materials and Methods	
5.3.1.		
5.3.2.	$\mathcal{U}$	-
	ed ion beam (FIB)	
5.3.3.	1	
5.3.4.		
	Results and Discussion	
5.4.1.		
5.4.2.	1 1	
5.5.	Conclusions	89
6. DEVI	ELOPMENT OF A MATHEMATICAL MODEL DECRIBING	
	ELUPMENT OF A MATHEMATICAL MODEL DECKIBING	00

6.1.	.1. Abstract		90		
<b>6.2.</b>	6.2. Introduction		91		
6.3. Materials and Methods		rials and Methods		92	92
6.4.	Ma	93			
6.5.		sults and Discussion			
6.:		Model validation			
6.:	5.2.	Statistical analysis	105		
		onclusions			
7. C	ONCI	LUSIONS	110		
REFE	RENC	CES	113		

## LIST OF TABLES

Table	<b>2.1:</b> Ljung box test p values for control groups at different number of lags 32
Table	<b>3.1:</b> Mobile phase flow gradient for UPLC-MS analysis: solvent A (10 mM NH <sub>4</sub> CH <sub>3</sub> COO) and B (50% CH <sub>3</sub> OH and 50% CH <sub>3</sub> CN). The percentage represents the volumetric ratio of solvent A over solvent B
Table	<b>3.2:</b> Effective diameter of COOH and amidine PNP in 10 mM KCl measured by dynamic light scattering at 25 °C
Table	<b>3.3:</b> Zeta potential of COOH and amidine PNP in 10 mM KCl measured by Phase analysis light scattering at 25 °C
Table	<b>4.1:</b> Comparision of BLM posassium sensors
Table	<b>6.1:</b> Kinetic constants of functionalized PNP. The number after PNP stands for size of PNP while the last number shows the replication
Table	<b>6.2:</b> Kinetic constants of functionalized PGL. The number after PGL shows the replication

## LIST OF FIGURES

Figure	1.1: Schematic diagram of electrochemical cell used to characterize pBLM formed across pore separating two reservoirs containing 20 mM KCl and 20 mM HEPES buffer
Figure	<b>1.2:</b> Schematic diagram of liposome as one type of model membranes
Figure	<b>1.3:</b> Schematic formation of tBLM on gold electrode via self-assembly followed by liposome rupture
Figure	<b>1.4:</b> Modes for Interaction of different types of ENM with model BLM
Figure	<b>2.1:</b> EIS measurement setup. 23
Figure	<b>2.2:</b> (A) Modified Randles equivalent circuit that consists of an electrolyte solution resistance R <sub>S</sub> , a membrane capacitance, C <sub>m</sub> , a membrane resistance, R <sub>m</sub> , and a constant-phase element, which dominates the hydrophilic spacer region. (B) Experimental and predicted EIS spectra of tBLM formed on 0.45 cm <sup>2</sup> gold. Left vertical axis: log of impedance (Z) magnitude (diamonds). Right vertical axis: minus phase angle (squares). Solid curves are impedance curves simulated from modified Randles equivalent circuit using Zview software
Figure	<b>2.3:</b> Size distribution (A) and zeta potential (B) of silica-core nanoparticles prior to exposure to tBLM. An asterisk indicates significant difference between effective diameter or zeta potential of carboxylic acid or bare silica and amine silica.
Figure	2.4: AFM images of tBLM in DI water (A) and bare gold (B)
Figure	2.5: Membrane resistance time profiles during tBLM interaction with 300 $\mu$ g/mL bare and functionalized silica-core nanoparticles in 10 mM KCl. The addition of (A) an aliquot of water (control), (B) carboxyl functionalized silica, (C) amine functionalized silica, (D) bare silica, and (E) amine functionalized silica nanoparticles was performed immediately after first $R_m$ recorded for each replicate. Open points are experimental values, and curves are optimized exponential model fits.
Figure	<b>2.6:</b> Hierarchical clustering dendrogram resulting from Ward's method analysis of Figure 5 data. Parameters for dendrogram in were analyzed (A) from data in Figures 2.5 (A)-(D), and (B) from data in Figures 2.5 (A), (B), (D). and (E). The sequence of clustering steps is shown below the line, and the AU p-value for each clustering step is shown above the line. The vertical axis is a measure of the distance between the members of each clustered set

<b>Figure 2.7:</b> (A) Effective diameter of silica-core nanoparticles prior to and after interaction with tBLM, measured by DLS. An asterisk indicates signific difference of effective diameter of silica nanoparticles between before tBl exposure and after. (B) Effective diameter of bare silica nanoparticles un various conditions by DLS. The asterisk indicates the size of bare silica measured in the presence of tBLM is significantly higher than that measured in all ot conditions.	cant LM der der ther
<b>Figure 3.1:</b> Experimental and equivalent circuit-predicted EIS spectra of the tBI formed on 0.48 cm <sup>2</sup> gold. Left vertical axis: log of impedance magnitudiamonds). Right vertical axis: minus phase angle (squares). Solid curves impedance curves simulated by the equivalent circuit using Zview software	ude are
<b>Figure 3.2:</b> $R_m$ profiles over time during tBLM interaction with 100 µg/mL PNP in mM KCl. (A): 100 nm COOH PNP, (B): 20 nm COOH PNP, (C): 23 nm Amid PNP and (D): 120 nm Amidine PNP. $R_m$ was extracted from EIS data fitted equivalent circuit model. Three replicates were done, labeled as open diamon squares and triangles. All solid curves were fitted $R_m$ by a time depend exponential model as $R_m$ =a*exp(b*t)+c where a, b and c represent initial $R_m$ , a constant and final $R_m$ after addition of PNP	line by nds, lent rate
<b>Figure 3.3:</b> Rate parameter (A) and R <sub>m</sub> % (B) extracted using an exponential decay most and calculated from R <sub>m</sub> profiles of COOH or amidine PNP interaction with tBl in 10 mM KCl, respectively. The asterisk indicates statistical difference in a parameter b or R <sub>m</sub> % when comparing two different sizes of PNP functionali with either COOH or amidine. The pound sign indicates statistical difference rate parameter b or R <sub>m</sub> % when comparing 20 nm COOH PNP and 23 nm amid PNP or comparing 100 nm COOH PNP and 120 nm amidine PNP	LM rate zed e in line
<b>Figure 3.4:</b> Hierarchical clustering dendrogram of 20 and 100 COOH, as well as 23 and 120 nm amidine PNP interaction with tBLM. Distances between objects who forming the clusters were calculated by Euclidean distance. Ward's method was used to evaluate distances between clusters and to determine which clusters should be linked together at each step.	hen was ters
<b>Figure 3.5:</b> Size distribution of COOH and amidine PNP in 10 mM KCl prior to after tBLM exposure for 5 hrs, measured by DLS at 25 °C. (A): 20 nm COO PNP; (B) 100 nm COOH PNP; (C): 23 nm Amidine PNP and (D): 120 Amidine PNP.	OH nm
<b>Figure 3.6:</b> Images of PDMS reservoir containing functionalized PNP after exposure tBLM for 5 h: (A) 23 nm Amidine PNP; (B) 120 nm Amidine PNP; (C) 20 COOH PNP; (D) 120 nm COOH PNP.	nm
<b>Figure 3.7:</b> Size distribution of amidine PNP at different concentrations of DO liposome in 10 mM KCl, measured by DLS at 25 °C. (A): 23 nm Amidine PNP 0 min; (B) 23 nm Amidine PNP at 300 min; (C): 120 nm Amidine PNP at 0 min;	P at

	and (D): 120 nm Amidine PNP at 300 min. Residue concentration of DOPC liposome was <1.3 µM when tBLM was interacting with functionalized PNP while at all other concentrations of DOPC liposome, amidine PNP did not contact a tBLM.
Figure	<b>3.8:</b> Peak area of DOPC at m/z=786.6 analyzed by UPLC-MS. DOPC lipids were extracted from functionalized PNP after exposure to tBLM and bare gold for 5 h as well as from the solution where PNP was not added in the presence of tBLM. A and C in the x axis labeled stand for amidine and COOH, respectively 55
Figure	<b>4.1:</b> Electrochemical biosensor array microsystem concept with fluid delivery to an electrode array on the top of a silicon integrated circuit
Figure	<b>4.2:</b> Impedance spectrum of gramicidin embedded tBLM in presence of KCl Inset is a magnified plot of the R <sub>m</sub> -dominated frequency range
Figure	<b>4.3:</b> Membrane resistance R <sub>m</sub> versus KCl concentration. Inset is a magnified plot in concentration range of blood potassium
Figure	<b>4.4:</b> EIS spectra taken prior to and after addition of 200 μg/mL MWNT to tBLM formed on micro-electrode
Figure	<b>5.1:</b> SEM image of nanopore on Si <sub>3</sub> N <sub>4</sub> window. The horizontal (H1) and vertical (V1) diameters are 727.0 nm and 794.4 nm, respectively
Figure	<b>5.2:</b> Experimental and fitting impedance spectrum taken prior to and after nanopore pBLM formation on silicon nitride window. Log of impedance magnitude: squares and circles for nanopore pBLM and nanopore, respectively. Minus phase angle: diamonds and triangles for nanopore pBLM and nanopore, respectively. All blue curves are impedance data fitted by Zview
Figure	<b>5.3:</b> Trace of gramicidin (20 nM in ethanol) channel incorporated in nanopore pBLM in 20 mM KCl and 20 mM HEPES
Figure	<b>5.4:</b> (A) Current vs time profile of pBLM composed of lipid mixture (POPC:POPE=3:1) without (in pink) and with (in black) 300 μg/mL PEG terminated silica NPs in 20 mM KCl and 20 mM HEPES at -80 mV, respectively (B) Corresponding histogram for (A).
Figure	<b>5.5:</b> (A) Current vs time profile of DOPC pBLM without (in pink) and with (in black) 20 μg/mL F-MWNT in 20 mM KCl and 20 mM HEPES at +50 mV. (B) Corresponding histogram for (A)
Figure	<b>6.1:</b> R <sub>m</sub> profiles over time during tBLM interaction with 100 μg/mL PNP in 10 mM KCl. (A): COOH PNP (20 nm), (B): COOH PNP (100 nm), (C): Amidine PNP (23 nm) and (D): Amidine PNP (120 nm). R <sub>m</sub> was extracted from EIS data fit by equivalent circuit model. Three replicates were done, labeled as open

empirical exponential model and by the mechanistic model, respectively 100
Figure 6.2: $R_m$ profiles over time during tBLM interaction with 100 µg/mL functionalized PGL in 100 mM KCl. (A): OH PGL (128 nm), (B): COOH PGL (100 nm) and (C): NH <sub>2</sub> PGL (94 nm). $R_m$ was extracted from EIS data fit by equivalent circuit model. Three replicates were done, labeled as open diamonds, squares and triangles. All solid curves were fit $R_m$ by the mechanistic model 102
<b>Figure 6.3:</b> Hierarchical clustering dendrogram of COOH (20 and 100 nm) and amidine PNP (23 nm and 120 nm) interaction with tBLM. Distances between objects when forming the clusters are calculated by Euclidean distance. Analysis of parameters extracted from mechanistic model was performed by evaluating distances between clusters using Ward's method
<b>Figure 6.4:</b> Hierarchical clustering dendrogram of COOH, OH, and NH <sub>2</sub> PGL interaction with tBLM. Distances between objects when forming the clusters are calculated by Euclidean distance. Analysis of parameters extracted from mechanistic model was performed by evaluating distances between clusters using the Ward's method

#### **KEY TO ABBREVIATIONS**

## **Chemicals**

ENM Engineered nanomaterials

Ag/AgCl Silver/silver chloride

CaCl<sub>2</sub> Calcium chloride

DI water Deionized water

DOPC 1,2-dioleoyl-*sn*-glycero-3-phosphocholine

DPPTE 1,2-dipalmitoyl-*sn*-glycero-3-phosphothioethanol

EDTA Ehtylenediamine tetraacetic acid

DMF Dimethylformamide

HEPES 4-(2-hydroxyethyl)-1-piperazineethanesulfonic acid

KCl Potassium chloride

NaCl Sodium chloride

NP Nanoparticles

PGL Polypropargyl glycolide

PEG Polyethylene glycol

DPhPC 1, 2-diphytanoyl-*sn*-glycero-3-phosphocholine

POPC 1-palimotoyl, 2-oleoyl -sn-glycero-3-phosphocholine

POPE 1-palimotoyl, 2-oleoyl -sn-glycero-3-phosphoethanolamine

PNP Polystyrene nanoparticles

NH<sub>4</sub>C<sub>2</sub>H<sub>3</sub>O<sub>2</sub> Ammonium acetate

CH<sub>3</sub>OH Methanol

CH<sub>3</sub>CN Acetonitrile

PEG Polyethylene glycol

MWNT Multiwall carbon nanotubes

## **Symbols**

A Electrode area

A<sub>d</sub> Defect area

A<sub>bu</sub> Bilayer area in upper leaflet

A<sub>du</sub> Defect area in upper leaflet

A<sub>bl</sub> Bilayer area in lower leaflet

A<sub>dl</sub> Defect area in lower leaflet

C<sub>m</sub> Membrane capacitance

R<sub>m</sub> Membrane resistance

CPE Constant phase element

l Half bilayer thickness

t Time

Z Impedance

ENM penetration depth

Non-tethering lipid fraction in lower leaflet of tBLM

Z<sub>W</sub> Warburg impedance

M	Phase delay
ω	Frequency
$R_{u}$	Upper leaflet resistance
$R_l$	Lower leaflet resistance
	Resistivity
$\mathbf{k}_2$	Absorption rate constant
$k_3$	Lipid removal rate constant
$n_1$	ENM concentration in the bulk solution
$n_2$	Number of defects
$n_3$	Number of complexes
$\mathbf{k}_2$	Absorption rate constant
$k_3$	Lipid removal rate constant
$R_{bu}$	Continuous bilayer resistance in upper leaflet resistance
$R_{bl}$	Continuous bilayer resistance in lower leaflet resistance
$R_{du}$	Defect resistance in upper leaflet resistance
$R_{dl}$	Defect resistance in lower leaflet resistance
b	Bilayer resistivity
d	Defect resistivity
$V_n$	Volume of total free lipids
$V_{nl}$	Volume of free lipids in lower leaflet
$V_{nu}$	Volume of free lipids in upper leaflet

V<sub>cu</sub> Free lipid volume captured by ENM in upper leaflet

V<sub>cl</sub> Free lipid volume captured by ENM in lower leaflet

## **Terminologies**

BLM Bilayer lipid membrane

tBLM Tethered bilayer lipid membrane

pBLM Planar bilayer lipid membrane

SAM Self assembled monolayer

sBLM Supported BLM

CMOS Complementary-symmetry metal—oxide—semiconductor

LOD Limit of detection

#### Instrumentation

AFM Atomic force microscopy

CV Cyclic voltammetry

CHI CH Instruments

DLS Dynamic light scattering

EIS Electrochemical impedance spectroscopy

FIB Focused ion beam

UPLC-MS Ultra performance liquid chromatography-Mass spectrometry

#### 1. INTRODUCTION

## 1.1. Motivation and Objectives

With booming application of nanotechnology, engineered nanomaterials (ENM) exhibit desirable electronic, catalytic and photonic properties and are rapidly being introduced into diverse commercial products [1-4]. However, considerable evidence has been obtained through in-vitro [5] and in-vivo [6, 7] studies that ENM can cause significant health risks [8, 9]. The ENM can enter the body through multiple pathways, interact with cells and then induce cytotoxicity in a variety of ways, including disrupting membranes, denaturing proteins, triggering oxidative stress, inducing inflammation, etc. Currently, methods to assess health effects of ENM and to rapidly screen ENM for likely health risks are inadequate [10].

For ENM to trigger toxicity, they must interact with cell membranes [11]. A wide variety of interaction mechanisms are possible; the ENM could bind to the membrane, aggregate around the membrane, remove lipids from the membrane, compress the membrane, become stably embedded in the membrane, pass through the membrane, create dynamic pores in the membrane, and be endocytosed by the membrane, etc. [12]. ENM physicochemical properties such as concentration, size, surface charge, shape, chemical functionalities, heterogeneity, hydrophobicity or hydrophilicity and surface ligand arrangement, are likely to strongly influence its interactions with biomembranes [11].

In spite of the importance of ENM-biomembrane molecular interactions, there is little knowledge and poor understanding about the mechanism by which nanoparticles interact with cell membranes and about how they may lead to toxicity. Therefore, improved methods to characterize them are needed, for many of these studies have shown contradictory results on the same test substance due to lack of standardized testing procedures. A comprehensive understanding of molecular interactions between ENM and cell membranes is also needed to study ENM toxicity and develop ENM-based biomedical technologies [13]. There are several challenges associated with ENM toxicity studies using in-vivo or in-vitro assays. One of them arises from the inherent complexity of cell biomembranes, which are composed of a fluid lipid bilayer with a variety of embedded proteins, carbonhydrates, and other accessory molecules. The integrity of biomembrane contributes functionalities needed for vital membrane involved processes, including recognition, communication, energy generation, and selective molecular transport [14, 15]. Furthermore, biomembrane composition and function varies between different parts of a cell and in different cell types [16]. As a result, the inherent complexity and diversity of intact biomembranes make it difficult to carry out well defined experiments, to test hypotheses about the role of specific biomembrane components during ENM-biomembrane interactions and to interpret experimental results from different laboratories. To overcome these disadvantages, a nanostructured interface containing a bilayer lipid membrane (BLM) and the minimum number of other membrane constituents provides a promising, bottom-up approach to study ENMbiomembrane interactions. The composition of BLM interface can be customized to mimic desired biomembrane functions.

The overall objective of this work is to develop a fundamental understanding of how ENM interact with biomembrane, and to evaluate potential health risk of ENM. More specifically, the proposed research aims at (1) developing robust, reproducible model membrane platforms suitable for characterization of ENM-BLM interactions by electrochemical and electrophysiological techniques, (2) developing mathematical models to predict ENM activities against biomembrane and thereby potential toxicity, (3) developing methods that not only can characterize biomembrane-ENM interaction but also are adaptable to high throughput mode for screening ENM libraries.

#### 1.2. Research Problem Definition

The projects presented in this thesis focused on two different platforms of synthetic BLM that are employed to provide a mimetic biomembrane environment: tethered bilayer lipid membrane (tBLM) and planar lipid bilayer membrane (pBLM). The pBLM based nanostructured biomimetic interfaces were originally used in characterization of ion channels [17], ionophores [18] and toxins [19] with high sensitivity on the order of picosiemons. Recently, the pBLM based assays have migrated to tBLM based platforms which are involved in a variety of transmembrane ion flex studies [20, 21] as well as in characterizing ENM interactions with biomembrane [22]. The tBLM system overcomes several disadvantages associated with traditional BLM systems. Firstly, it provides a hydrophilic spacer layer to serve as an ion reservoir to allow ions to enter and egress. Secondly, tBLM has enhanced stability over classical pBLM. Thirdly, formation of tBLM is through molecular self assembly instead of requiring manual procedures and skilled technicians. All these advantages make tBLM more promising in adaption to high throughput applications. So, we adapted tBLM method to miniaturized electrode array coupled with lab-designed EIS acquisition chip for ENM studies.

On the other hand, given that the pBLM system has its own merit of high sensitivity and is capable of detecting single channel, the development of a new generation of pBLM

platforms with improved stability and robustness is also needed [23-25]. Then, dynamics of interactions between ENM and pBLM can be characterized and analyzed according to electrical signature profiles following ENM exposure. In particular, the integration of microfluidic channel into pBLM system allows formation of pBLM and delivery of ENM in an automated mode, which can potentially accelerate screening ENM libraries. Therefore, one project in the thesis focused on developing a nanopore based pBLM system using lithography technique. The newly developed nanopore pBLM was further characterized and validated for ENM studies in order to achieve the goal of higher throughput.

The key target studied in the presented projects is nanomaterials, more specifically, ENM. Nanotechnology has advanced fabrication of ENM in ways that ENM can be customized with desired properties and functions [13]. Therefore, ENM are being increasingly added into commercial applications in the area of sensors, cosmetics, diagnostics and drug delivery [4, 26, 27]. As a result, human are increasingly being exposed to nanomaterials in daily life, providing an incentive to understand the mechanisms by which nanomaterials interact with cell membranes. In this work, a wide variety of ENM, ranging from lab-fabricated nanoparticles, nanotubes, nano-sized polymers to commercialized nanomaterials, was used to investigate how ENM influenced ENM-BLM interactions. In the dynamic process of ENM-BLM interaction, the effects are determined by ENM properties including concentration, shape, size, surface charge, chemical functionalities, angle of curvature, porosity and surface crystallinity, heterogeneity, hydrophobicity or hydrophilicity and surface ligand arrangement [11]. Main forces governing interfacial interactions include hydrodynamic interactions due to

convection, electrodynamic interactions such as van der Waals forces, electrostatic attraction or repulsion and solvent interactions [11]. Although nanoparticles, in general, are internalized and translocated into cells via endocytosis [15], it is still not clear that the role of ENM properties in interactions between ENM and lipid bilayer without assistance of other membrane accessory molecules. Accordingly, effects of size, surface charge, and chemical functionalities were investigated in the projects to understand how each of these factors played a part in ENM interactions with BLM.

As a selective and insulating barrier, cell membranes can block ion flow, which is reflected by electrical properties of cell membranes. Such electrical property due to certain substances can be characterized and measured by electrochemical impedance spectroscopy (EIS) [28] and electrophysiology techniques [17], which is an another advantage of using nanostructured interfaces containing a BLM to mimic desired biomembrane functions to study ENM-biomembrane interactions. Therefore, electrical properties were main indicators and parameters measured in investigating ENM-BLM interaction, allowing establishing hierarchically assorted ENM libraries according to distinct patterns of electrical signatures.

Other than experimental protocols, numerous attempts have been made to interpret experimental EIS data based on potential and/or concentration gradient [29-32]. These models tend to study dynamics of ion transport but lack of ability to identify transport dynamics of ionophore such as gramicidin and valinomycin, both of which could interact with BLM. Therefore, a mathematical model that can describe ENM transport, ENM-BLM interaction, and BLM integration/deformation is needed. The presented kinetic model in the dissertation was designed to help explain dynamic trajectory of ENM-BLM

interactions, better understand the mechanisms by which ENM-BLM interactions are dominated and determined and predict the fate of ENM after exposure to BLM.

#### 1.3. Background

#### 1.3.1. Model bilayer lipid membranes

Biological membranes, composed of a fluid phospholipid bilayer with embedded proteins, carbohydrates, and their complexes, are vital components for prokaryotic and eukaryotic organisms [33]. Cell membranes are not only selective barriers dominating the transport of materials into and out of the cell but also are in a dynamic state contributing in many cellular activities such as recognition, communication and catalytic functions [34]. Moreover, there is wide variation of biomembrane composition between different cell types, and biomembrane dynamics is in transient state, far from homogeneous [35]. Both of the inherent complexity and diversity of intact biomembranes make it difficult to perform experiments in well-defined conditions and thereby even harder to identify the role of specific biomembrane components during ENM-biomembrane interactions. Accordingly, the use of a biomimetic membrane that has a well-controlled composition provides an excellent tool to elucidate biomembrane function mechanisms [36].

Since the pioneering work back in the 1960s, the first generation of experimental bilayer lipid membrane systems, planar bilayer lipid membrane (pBLM), has been developed and extensively used as a model of biomembranes [18, 37-39]. A pBLM is usually formed by painting or brushing a small amount of solution containing lipids across an aperture (0.1-2 mm in diameter) between two aqueous solutions, shown in Figure 1.1. The quality of pBLM formed can be determined by measuring its electrical properties. A good unmodified pBLM typically has a membrane resistance on the order

of  $10\sim100~M~cm^2$ , a membrane specific capacitance around  $0.5~\mu F/cm^2$ , and a dielectric breakdown voltage above 100~mV [16].

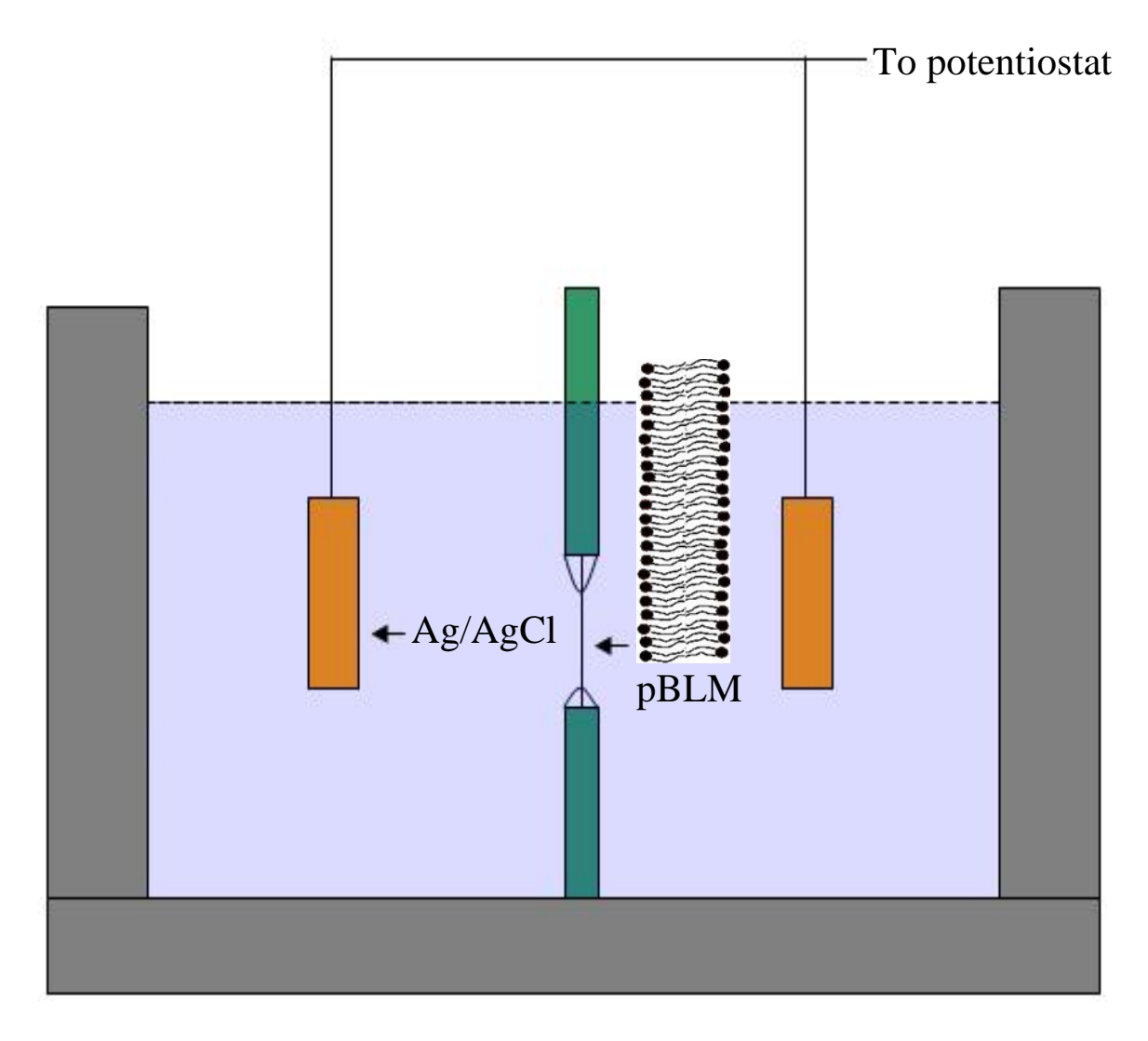


**Figure 1.1:** Schematic diagram of electrochemical cell used to characterize pBLM formed across pore separating two reservoirs containing 20 mM KCl and 20 mM HEPES buffer.

Another widely used experimental BLM for biomembranes was also developed as vesicles/liposomes which consist of spherical BLMs enclosing a volume of aqueous solution [40-42], shown in Figure 1.2. The formation of liposomes can be achieved by

either mechanical sonication or extrusion of a suspension of hydrated lipids. Electrical properties of pBLM and liposome can be readily characterized by electrophysiology technique [16] and patch clamp technique [43], respectively. These techniques measure transient ionic current across the model BLM using electronics that have a sensitivity on the order of pA [44]. These two methods offer relatively high temporal resolution and sensitivity, advancing and elucidating a variety range of molecular studies in biosensing applications [45]. For example, pBLM system has been used in characterizing channel proteins such as gramicidin [17] and porin [46], selective ionophores such as AS701 [18], and silica nanospheres induced membrane disruption [47]. Liposomes have been used as biomimetic sensors in areas of antigen-antibody reaction involved immunoassays [48], partitioning behavior of organic compounds between water and biological systems [49-51], and release rate of entrapped vesicle contents [40, 52].

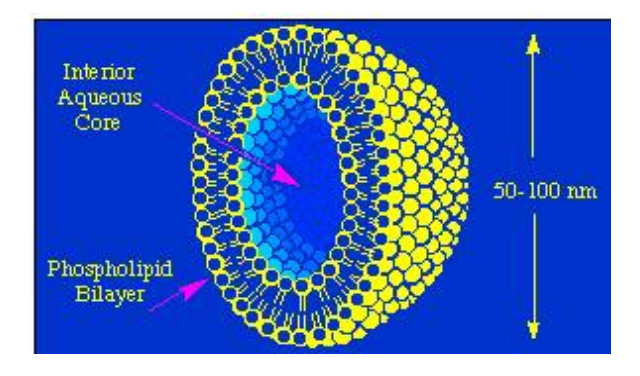


**Figure 1.2:** Schematic diagram of liposome as one type of model membranes (http://www.chem.ucla.edu/dept/Faculty/hawthorne/liposome/liposome.htm).

Although pBLM and liposome, as model membrane, coupled with sensitive characterization techniques have been employed in numerous biomedical applications, they are still fragile in terms of low mechanical stability and limited lifetime. To overcome this drawback, the concept of solid supported BLM (sBLM) that possessed

structural and thermodynamic properties of pBLM and liposomes was raised [48]. In particular, tethered BLM (tBLM) that uses self-assembly through spacer molecules such as thiol group has been recently developed based on inception of sBLM [14, 53]. The tBLM construction (Figure 1.3) has several advantages over classical model membranes [28]. For one hand, given the covalent bonding of linker (e.g. thiol lipids) to the underlying substrate surface (e.g. gold), tBLM system has an improved stability and prolonged lifetime, resulting in a more robust biomimetic platform than pBLM. On the other hand, tBLM system has solved proximity problem resulting from sBLM and provides a space layer to hold extra part of proteins or macromolecules embedded in membranes as well as an ion storage. There are two main strategies to prepare tBLM: vesicle fusion or Langmuir-Blodgett transfer on a substrate and Langmuir-Blodgett transfer or self-assembly of monolayer followed by vesicle fusion onto a substrate [14]. Furthermore, tBLM formed on a metal substrate allows for characterization of resulting tBLM not only by surface sensitive techniques but also by electrochemical methods within defined electrical field [54]. Therefore, tBLM model are extensively employed in studies of ion channels as well as their kinetics [20, 55, 56], function of membrane associated proteins [21], and electron transport of bioelectroactive molecules [57].

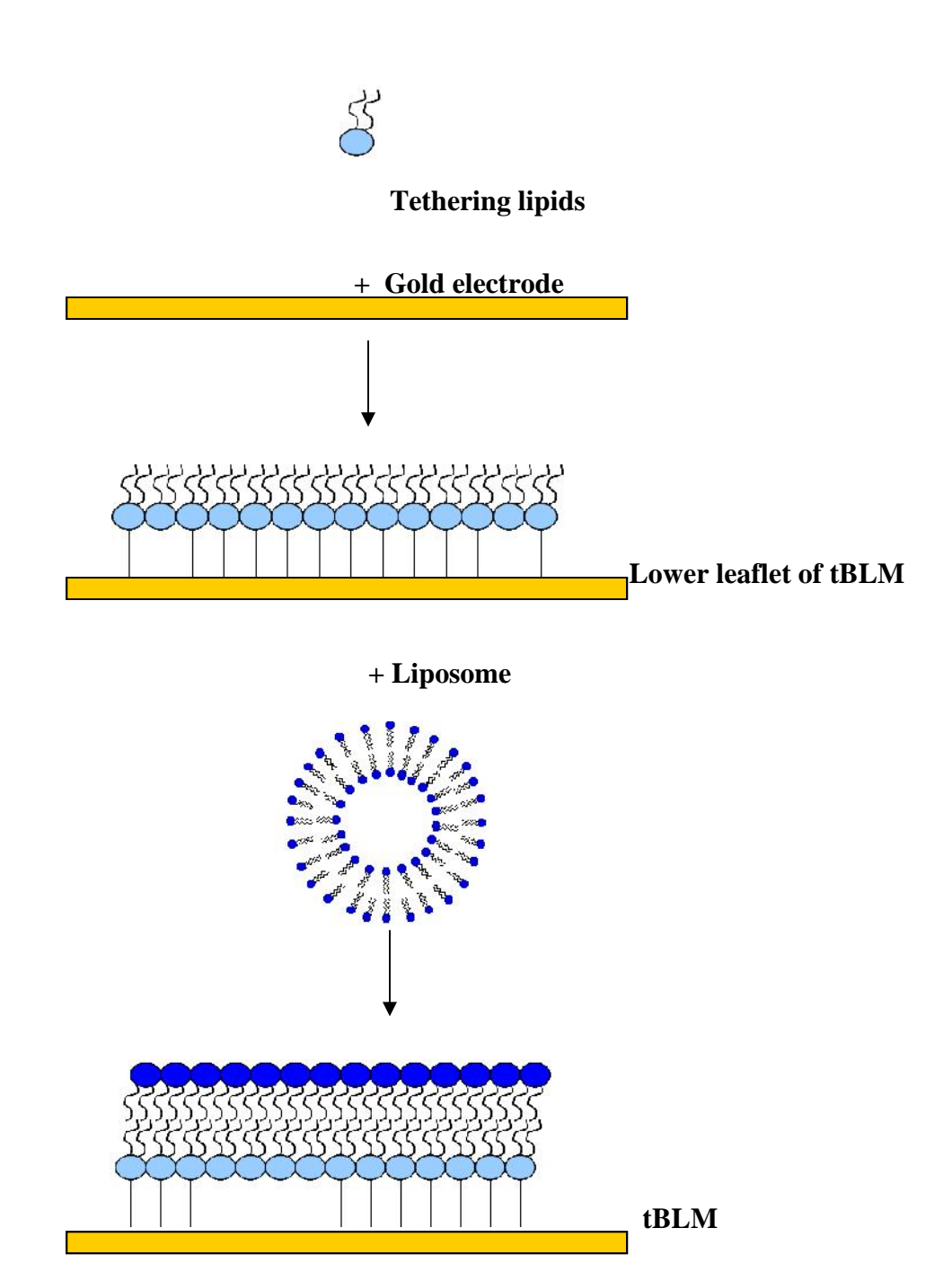


**Figure 1.3:** Schematic formation of tBLM on gold electrode via self-assembly followed by liposome rupture.

## 1.3.2. Engineered nanomaterials

Nanomaterials, which have at least one dimension smaller than 100 nm, have extremely large specific surface area and often show unique electronic, photonic and

catalytic properties [2]. There are a wide variety of types of ENM: metals, metal oxides, polymers, carbon based nanotubes, and dendrimers, etc. The dimensions of many biological macromolecules allow them to be classified as nanoparticles [10]. ENM that are designed with specific functions and properties have huge potential markets and are increasingly being used in the areas of cosmetics, sensors, drug delivery and diagnostics [2]. As a result, human are increasingly being exposed to ENM in daily life, providing an incentive to understand the mechanisms by which ENM interact with cell membranes. Interaction of different types of ENM with a cell membrane is shown schematically in Figure 1.4, leading to structural and/or functional change of a cell membrane [36]. On the other hand, the fate of ENM also depends on ENM-BLM interaction. The mode of interaction is determined, by the properties of both the membrane and the ENM, including concentration, shape, size, surface charge, chemical functionalities, heterogeneity, hydrophobicity or hydrophilicity and surface ligand arrangement of ENM as well as fluidity of biomembrane [11]. Main forces governing interfacial interactions include hydrodynamic interactions due to convection, electrodynamic interactions such as van der Waals forces, electrostatic attraction or repulsion and solvent interactions.

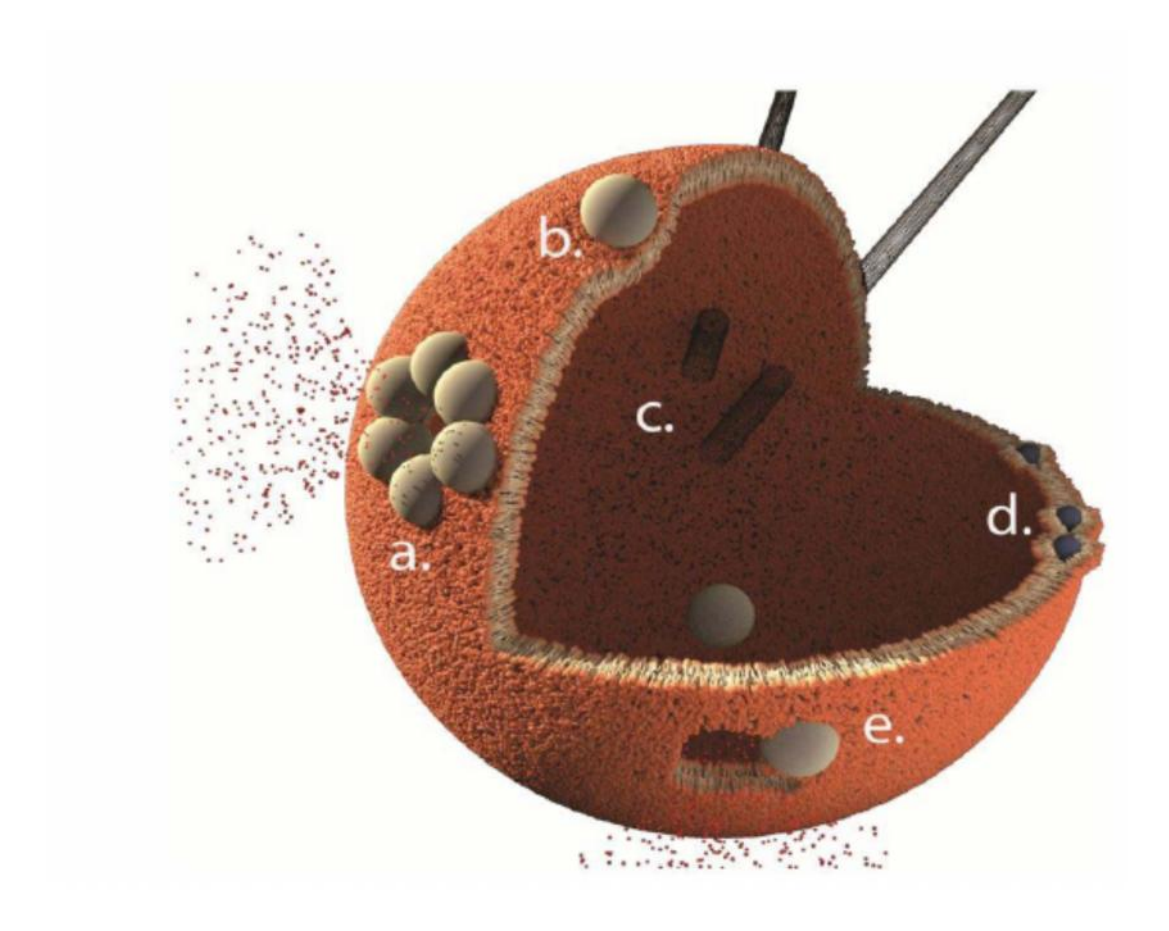


Figure 1.4: Modes for Interaction of different types of ENM with model BLM

In general, nanomaterials can be internalized and translocated into cells via endocytosis [15]. Nanomaterials might also traffic across lipid bilayer by paracellular pathways (tight junctions) or through "holes" (or defects) in the lipid bilayer. Here, it is the fluidity of the lipid bilayer interior that contributes more significantly than near the glycerol backbone in determining the permeability of nanomaterials [16]. On the other hand, the dynamic properties and fluidity of lipid bilayers are also affected by nanomaterials. Membrane fluidity was reported to increase with enhancing concentration of silver nanoparticles entrapped in dipalmitoylphosphatidylcholine (DPPC) liposomes which composed the top leaflet of the lipid bilayer [58].

Although it is still poorly understood about the mechanism of ENM transport across a cell membrane as well as ENM induced potential health risks, studies have demonstrated that ENM have the ability to penetrate cell membranes [59]. For example, Holl [60] investigated the interaction of poly (amidoamine) (PAMAM) dendrimers with supported 1,2-dimyristoyl-sn-glycero-3-phosphocholine (DMPC) lipid bilayers, showing that positively charged PAMAM dendrimers either initiated hole formation or expanded holes at existing defects of the lipid bilayer. In addition, ENM characteristics such as shape and size also influenced ENM-BLM interactions. In a study by Chithrani [61], spherical nanoparticles were absorbed 5 times more than rod-shaped nanoparticles with the same size. Also, the paper showed that the kinetics of uptake of gold nanoparticles varied with nanoparticle size and suggested that an optimal dimension may exist for efficient nanomaterial translocation across cell membranes. Therefore, ENM characteristics make active contributions to the interactions with lipid bilayer through forming electric double layer, enhancing the adsorption of ENM, initiating hole formation and reducing free surface energy via reorientation of surface structure [11].

Another challenge resulting from performing in-vitro and in-vivo assays to test ENM toxicity is that ENM are likely to aggregate in cell medium [36]. Then, physiochemical properties of ENM tend to change with a variety of shapes and sizes that need further confirmation. This is the reason why characterization of ENM only after synthesis is not adequate. Without careful characterization of ENM during ENM interaction with a cell membrane, it would result in a judicious interpretation of the outcome [62, 63]. To avoid unexpected influences due to complex cell culture medium, experiments can be conducted in a defined environment that does not promote

aggregation. So, this issue can be greatly avoided using biomimetic interface which is surrounded by only buffered electrolyte.

#### 1.3.3. Characterization of ENM-BLM interaction

Electrochemical impedance spectroscopy (EIS) and electrophysiology are two main techniques used to characterize electrical properties of model BLM in the presence/absence of ENM [16]. One run for EIS is on the order of several minutes while electrophysiology has a sampling frequency on the order of kilo Hz, both of which are label free and fast protocols compared to in-vivo and in-vitro assays. The impedance response typically reflects a distribution of reactivity that is commonly represented in equivalent electrical circuits. Two characteristic parameters, membrane resistance and capacitance are extracted after simulating EIS data using a Randles equivalent circuit [28] after modification. A good tBLM has a membrane resistance on the order of M cm<sup>2</sup> and a capacitance less than 1 μF/cm<sup>2</sup>, depending on the lipids used. A constant-phase element (CPE) replacing a double layer capacitance is employed in the equivalent circuit because it is generally not valid to assume that the electrode surface activity is homogeneous [64]. A CPE has two parameters: and Q which has units of s / cm² when 1, showing behavior that has been attributed to surface heterogeneity [65]. system has ENM-BLM interaction induced changes in resistive and/or capacitive properties of model BLM can be captured by EIS responses.

Electrophysiological method can capture transient conductance across BLM, thus enabling to characterize ENM-BLM interactions by analyzing patterns buried in the electrical signatures after ENM addition [36]. Recent studies have demonstrated its ability to characterize membrane disruption by silica nanoparticles [47].

In addition, BLM tethered on a metal substrate can allow for applying surface sensitive techniques, such as cyclic voltammetry (CV), atomic force microscope (AFM), and ellipsometry, in characterizing tBLM following ENM exposure. CV is a powerful and popular electrochemical technique for analytically studying electrochemical properties of systems [66]. For a tBLM deposited on solid substrate such as gold, the thickness of the BLM is a few nanometers, which is too far for electrons to transfer from electrode to electrochemical active redox species (e.g., ferrycyanide). When a tBLM of high quality is employed to characterize interactions between BLM and ENM or other biomolecules, CV is helpful to reveal the selectivity of the ion channel triggered by such interactions, further confirming the mechanism of the interactions. AFM is widely used to study lipid bilayer dynamics and provide information on surface topology [67]. For example, Holl [60] have investigated the interaction of poly (amidoamine) (PAMAM) dendrimers, positively charged dendrimers with supported 1,2-dimyristoyl-sn-glycero-3phosphocholine (DMPC) lipid bilayers. AFM images show that the positively charged PAMAM dendrimers either initiated hole formation or expanded holes at existing defects of the lipid bilayer. Ellipsometry is an optical technique to measure the thickness of lipid bilayers based on the change of polarization and the difference in refractive index between buffer and the adsorbed substances [14]. Jadhav et. al. [68] has reported characterizing thickness of monolayer (~2.7 nm) and bilayer (~5.7 nm) during tBLM formation using ellipsometry.

Although ENM have a specific size according to requirement for synthesis, they are likely to aggregate into especially when they are exposed to and interacting with BLM.

Therefore, characterization of ENM is performed by dynamic light scattering (DLS) and

phase analysis light scattering (PALS) prior to and after BLM exposure in order to study how ENM are influenced by BLM [69].

In addition to experimental protocols, there are also simulation methods, including molecular dynamics (MD), dissipative particle dynamics, Brownian dynamics and Monte Carlo method, to explore ENM-BLM interactions [35]. In particular, MD is the most popular approach, which applies Newton's equations of motion to derive the time dependent solution of the system. Current MD simulation studies also indicate formation of transient pores during interactions involving a cell membrane, which is consistent with the most possible mechanism for ions permeating across lipid bilayer and for lipid flip-flop. However, most of these modeling studies lacks of experimental data to support and to verify simulation results. As a result, a mechanistic model that can predict interactions between ENM and BLM based on experimental data is needed.

#### 2. tBLM INTERACTION WITH SILICA NANOPARTICLES

#### 2.1. Abstract

Engineered nanomaterials (ENM) have desirable properties that make them well suited for many commercial applications. However, a limited understanding of how ENM properties influence their molecular interactions with biomembranes hampers efforts to design ENM that are both safe and effective. This chapter describes the use of a tethered bilayer lipid membrane (tBLM) to characterize biomembrane disruption by functionalized silica-core nanoparticles and to investigate how surface functional group affect ENM-BLM interaction. Electrochemical impedance spectroscopy (EIS) was used to measure the time trajectory of tBLM resistance following nanoparticle exposure. Statistical analysis of parameters from an exponential resistance decay model was then used to quantify and analyze differences between the impedance profiles of nanoparticles that were unfunctionalized, amine functionalized, or carboxyl functionalized. All of the nanoparticles triggered a decrease in membrane resistance, indicating nanoparticleinduced disruption of the tBLM. Hierarchical clustering allowed the potency of nanoparticles for reducing tBLM resistance to be ranked in the order amine > carboxyl ~ bare silica. Dynamic light scattering analysis revealed that tBLM exposure triggered minor coalescence for bare and amine functionalized silica nanoparticles but not for carboxyl functionalized silica nanoparticles. These results indicate that the tBLM method can reproducibly characterize ENM-induced biomembrane disruption and can distinguish the BLM-disruption patterns of nanoparticles that are identical except for their surface functional groups. The method provides insight into mechanisms of molecular interaction involving biomembranes and is suitable for miniaturization and automation for highthroughput applications to help assess the health risk of nanomaterial exposure or identify ENM having a desired mode of interaction with biomembranes.

#### 2.2. Introduction

Amorphous silica nanoparticles represent an excellent model ENM for systematic studies of ENM-BLM interactions, because they are commonly found in nature, are widely used in commercial products [70], and are being developed as cargo carriers in targeted drug delivery [71-73]. Compared to crystalline silica particles, which if inhaled can cause pulmonary silicosis [74], amorphous silica nanoparticles are much less toxic to the lung. Inhalation of amorphous silica triggers minimal pulmonary inflammation in rodents [75]. The nanotoxicity properties of amorphous silica nanoparticles have been shown to vary with their size [76], structure [77] and surface properties [59, 61], which can readily be customized via chemical functionalization. Pore formation in synthetic BLM composed of L- -dimyristoyl phosphatidylcholine (DMPC) induced by silica nanoparticles less than 22 nm in size has been monitored by atomic force microscopy (AFM) [78].

Several reports have suggested that transport of nanoparticles through biomembranes strongly depended on surface charge and size of nanoparticles tested [79-82]. Negatively charged nanoparticles were more rapidly taken up by adenocarcinoma lung cells than positively charged ones [83]. On the other hand, HeLa cells more rapidly endocytosed positively charged nanoparticles than negatively charged ones [84]. A recent review of the influence of surface properties of ENM-cell interactions indicated that, in general, uncharged ENM interact less aggressively with cells, and that positively charged ENM are most efficient in crossing cell membranes [59].

The purpose of this study was to test the hypothesis that a tBLM-based method could be used to distinguish patterns of biomembrane disruption caused by nanoparticles that had identical amorphous-silica cores but different surface functional groups. EIS was used to measure time-dependent changes in the  $R_{\rm m}$  of a highly insulating tBLM following exposure to three types of silica-core nanoparticles: bare, amine functionalized, and carboxyl functionalized. The rate of decrease in  $R_{\rm m}$  was described using an exponential model, and hierarchical clustering was applied to statistically analyze whether the method could distinguish between the effects of different silica-core ENM. DLS was used to measure changes in the nanoparticles' effective diameter before and after interactions with the tBLM. The results demonstrate the suitability of the tBLM method to screen ENM for aggressiveness in biomembrane disruption.

#### 2.3. Materials and Methods

#### 2.3.1. Materials

The phospholipids 1,2-dioleoyl-sn-glycero-phosphocholine(DOPC), and 1, 2-dipalmitoyl-sn-glycero-phosphothioethanol (DPPTE) were purchased from Avanti Polar Lipids Inc. (Alabaster, AL). All other chemicals, such as sodium chloride, chloroform, decane, ethanol, potassium chloride, and, 4-(2-hydroxyethyl)-1-piperazineethanesulfonic acid (HEPES) were purchased from Sigma Aldrich (St. Louis, MO).

## 2.3.2. Fabrication and characterization of silica-core nanoparticles

The surface functional silica-core nanoparticles were fabricated via click chemistry [85, 86]. Briefly, the silica-core nanoparticles were synthesized from colloidal silica SNOWTEX XS (SNTXS, 4-6 nm, 20 wt% suspension in H<sub>2</sub>O), 40 wt% suspension in

H<sub>2</sub>O), SNOWTEX 20L (Nissan Chemical Industries, Ltd SNT20L, 40-50 nm, 20 wt% suspension in H<sub>2</sub>O), and SNOWTEX ZL (Nissan Chemical Industries, Ltd SNTZL, 71 nm, 40 wt% suspension in H<sub>2</sub>O) using a two-step process. The surfaces of silica nanoparticles were modified with alkynyl-substituted triethoxysilanes to afford the alkyne modified particles, which enable modification of particle surfaces via 'click' chemistry, the Cu-catalyzed azide-alkyne cycloaddition, catalyzed by CuSO<sub>4</sub> and sodium ascorbate in dimethylformamide (DMF) and water (3:1). Copper ions were removed using ethylenediaminetetraacetic acid (EDTA) or ion exchange resin beads (Amberlite IRC-748). Since the click reaction was the final step in the synthesis, the particles were identical except for the surface chemistry. We synthesized silica-core nanoparticles with carboxylic acids, amines, and short methoxy-terminated polyethylene chains. To avoid aggregation, the modified silica nanoparticles were purified by dialysis against DI water, using dialysis tubing with molecular weight cut off (MWCO) values appropriate for the size of the particles.

DLS was performed to identify an aqueous medium for the experiments that did not induce aggregation. In addition, particle size distributions were measured before and after ENM exposure to the tBLM [26]. Effective diameter and surface charge (zeta potential) of functionalized silica-core nanoparticles were determined using a Brookhaven 90 Plus particle analyzer (Brookhaven Instruments Inc., Holtsville, NY) at 25°C in 10 mM KCl. In control experiments to determine conditions that triggered nanoparticle aggregation, bare silica nanoparticles were incubated in 10 mM KCl in a glass cuvette, in a PDMS reservoir only, and in a PDMS reservoir on gold without tBLM, before particle-size analysis.

### 2.3.3. Preparation of liposome

Small unilamellar vesicles (SUV) of DOPC were prepared by freeze drying DOPC dissolved in chloroform in a Labconco freeze dry system (Labconco Corporation, Kansas, MO) at -47°C for 2 h followed by hydration in buffer (10 mM HEPES, 150 mM NaCl, 2 mM CaCl<sub>2</sub>, pH 7.4) to a concentration of 1 mM. DOPC liposome was ultrasonicated in an ice bath for 20 min prior to use.

#### 2.3.4. Preparation of polydimethylsiloxane (PDMS) slab

A PDMS slab with a hole in it was used as a reservoir to contain the solutions that formed the tBLM on the gold. To make the PDMS slab, 77 g of PDMS prepolymer material with the curing agent in a 10:1 weight ratio and then poured on a polished silicon wafer in a petri dish. The petri dish was stored in a vacuum desiccator for 1 h and then cured at 60°C overnight.

#### 2.3.5. Formation of tBLM biomimetic interface

Typically, one terminal group based on polyethyleneglycol coupled with functionalized disulfide moiety binds to gold surfaces through chemisorption while the other terminal group chemically binds the BLM [87]. There are two steps in tBLM forming process [68]. In general, a self-assembled monolayer is first formed followed by liposome adsorption and rupture to form upper leaflet of tBLM.

Electrodes consisting of a gold layer (100 nm thick) coated on a silicon wafer by chemical vapor deposition (Lance Goddard Associates, Santa Clara, CA) were cleaned in fresh piranha solution (51% H<sub>2</sub>SO<sub>4</sub> and 30% H<sub>2</sub>O<sub>2</sub> in a ratio of 7:3) for 30 s, washed with deionized water and then dried in nitrogen. A self-assembled monolayer (SAM) of

DPPTE was chemically adsorbed by dipping a clean gold electrode into 1 mM ethanolic DPPTE solution for 1 h, rinsing with ethanol, and drying with nitrogen.

After ultrasonication for 20 min, 300  $\mu$ L of the resulting SUV suspension was added to the PDMS slab reservoir and incubated at room temperature for 24 h. After tBLM formation, the liposome solution was replaced with fresh 10 mM KCl electrolyte (pH 6.1). Then sonicated nanoparticle solution was transferred to the PDMS reservoir and mixed by a pipette to reach a final concentration of 300  $\mu$ g/mL in 10 mM KCl. In some control experiments, the volume of DOPC and nanoparticles transferred to the PDMS reservoir was varied, but the nanoparticles were maintained at the same concentration (300  $\mu$ g/mL in 10 mM KCl) in all experiments.

## 2.3.6. Electrochemical characterization of tBLM and ENM-BLM interaction

In this study, EIS was used to measure changes in  $R_m$  during 5 h incubation with 300 µg/mL silica-core nanoparticles. A supporting electrolyte of 10 mM KCl was chosen because it provided sufficient conductance for the EIS studies while not inducing significant nanoparticle aggregation. EIS experiments were conducted using a CHI 660B electrochemical workstation (CH Instruments Inc., Austin, TX) configured in a three-electrode setup (Figure 2.1). An ac perturbation of 5 mV was superimposed on dc bias of 0 V over a frequency ( ) range between 0.01 Hz and 10,000 Hz. Experiments were conducted in triplicate for each type of nanoparticle, including the control groups. To determine  $R_m$  values, a modified Randles equivalent circuit (Figure 2.2 (A)) was fit the electrical impedance (Z) data [88, 89] using Zview software (Scribner Associates,

Southern Pines, NC). A constant-phase element (CPE) was used in this modified model to represent electrical behavior of heterogeneous submembrane space [65, 90].

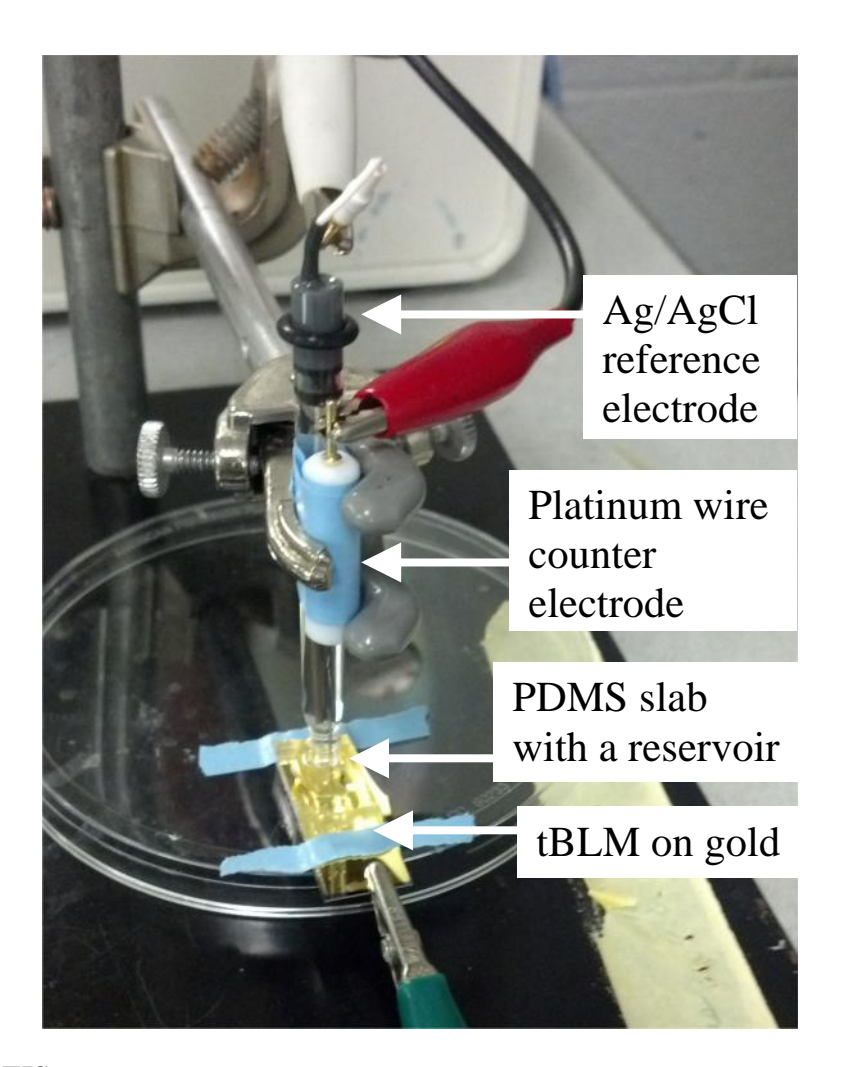
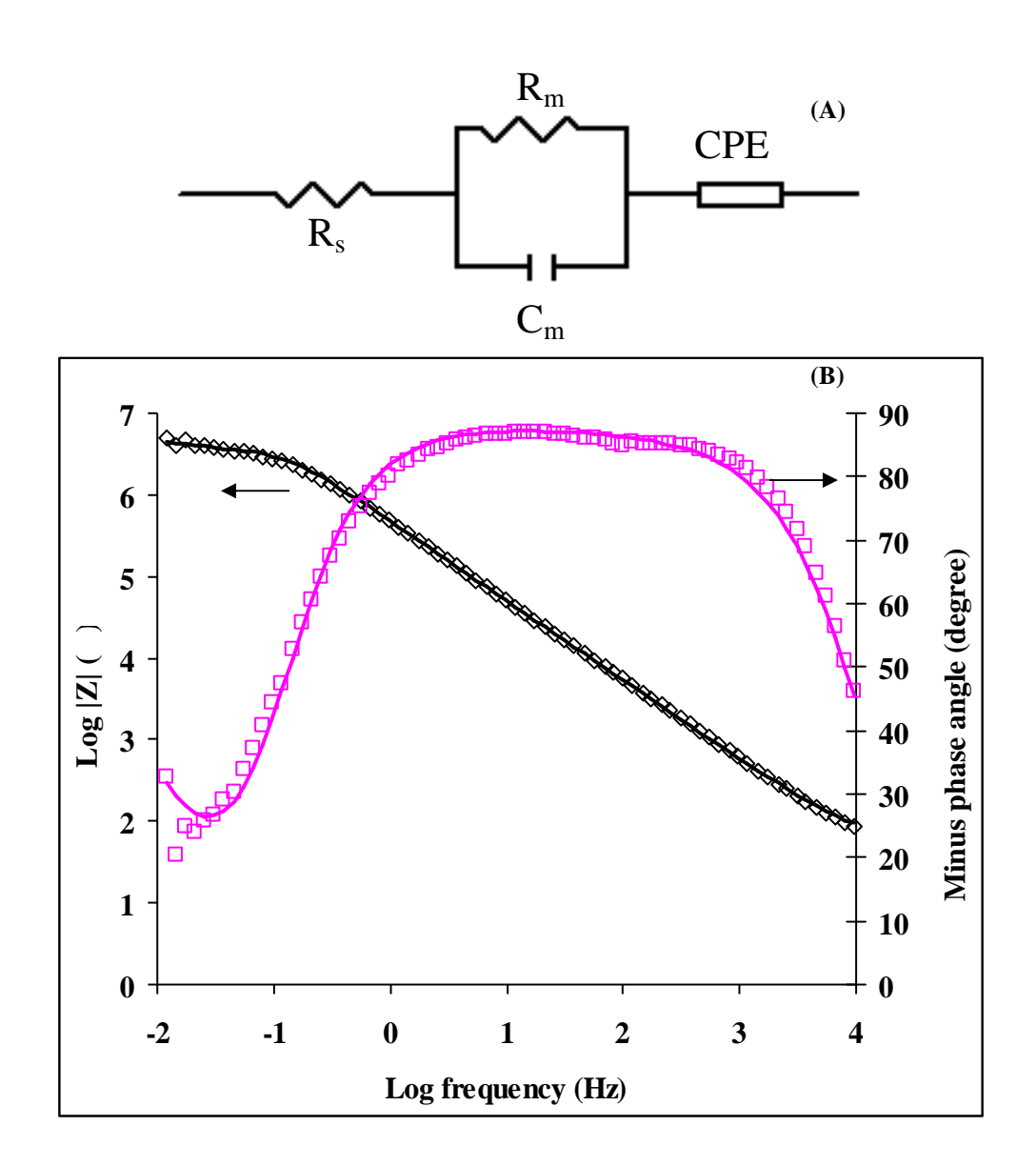


Figure 2.1: EIS measurement setup



**Figure 2.2:** (A) Modified Randles equivalent circuit that consists of an electrolyte solution resistance  $R_S$ , a membrane capacitance,  $C_m$ , a membrane resistance,  $R_m$ , and a constant-phase element, which dominates the hydrophilic spacer region. (B) Experimental and predicted EIS spectra of tBLM formed on 0.45 cm<sup>2</sup> gold. Left vertical axis: log of impedance (Z) magnitude (diamonds). Right vertical axis: minus phase angle (squares). Solid curves are impedance curves simulated from modified Randles equivalent circuit using Zview software.

## 2.3.7. Topological characterization of tBLM

A DPPTE/DOPC tBLM was formed using the procedure described above on a 1 cm×1 cm piece of freshly cleaned gold. AFM imaging experiments were performed in

tapping mode using an Asylum Research Cypher Scanning Probe Microscope (Santa Barbara, CA) equipped with a droplet cantilever holder. A drive of ~30 kHz and spring constant of 0.01 N/m for the silicon nitride cantilever were determined by thermal data. After tBLM formation, the liposome suspension was exchanged with DI water before AFM scanning.

#### 2.3.8. Statistical analysis

An exponential function (Eqn. 1) was fit to the  $R_{\rm m}$  vs time profiles measured during exposure to silica-core nanoparticles,

$$R_{m} = (R_{i} - R_{f}) \exp(kt) + R_{f}$$
 (1)

where  $R_i$  is the initial resistance,  $R_f$  is the final resistance, and k is the exponential rate constant. A relative membrane resistance change ( $R_m$ %) was also calculated using Eqn. 2:

$$R_{\rm m}\% = (R_{\rm i}-R_{\rm f})/R_{\rm i} \tag{2}$$

A pattern matrix containing a total of n=12 experiments as rows, and p=3 parameters, (R<sub>i</sub>-R<sub>f</sub>), k, and R<sub>m</sub>%, determined for each experiment as columns, was analyzed using hierarchical clustering procedures in R software (Version 2.13.2: The R Foundation for Statistical Computing), to quantify similarity between the curves. For hierarchical clustering, the distances between rows (experiments) when forming the clusters are calculated using Euclidean distance measured by summing the squared differences between rows over all columns (parameters). Since the parameters have scales in quite different orders of magnitude, the scales were standardized [91] prior to the clustering procedure to prevent a parameter with larger order of magnitude from dominating the clustering results. Also, Ward's method was used to evaluate Euclidean

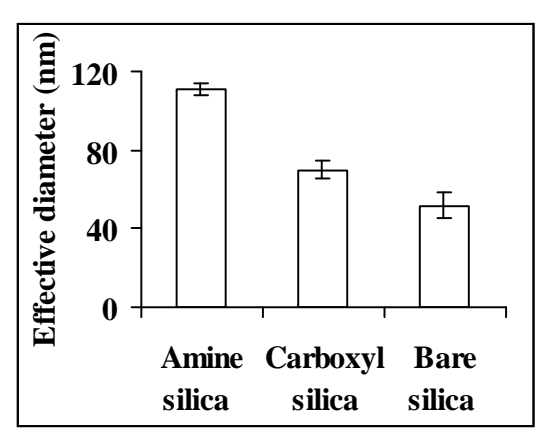
distances and to determine which clusters should be linked together at each step in the dendrogram. Since the number of sample points (experiments) to be clustered is relatively small, the uncertainty associated with the hierarchical clustering results was assessed by computing the approximately unbiased (AU) p-value via multiscale bootstrap resampling [92] with replacement at each bifurcation. AU p values provide quantitative assessment of confidence in each clustering step. AU p values close to 100% indicate relative certainty that the clustering is true. Two-sample t test assuming unequal variance and Wilcoxon rank sum test were performed to compare size and surface charge of silicacore nanoparticles before and after tBLM experiments. Differences were considered significant at p<0.05.

To identify whether measured changes in  $R_m$  following silica-core nanoparticle exposure were significant, the random fluctuation (noise) was estimated from the three control-group replicates that were not exposed to nanoparticles. The observations were assumed to be random samples from a normal distribution, and the variance was estimated using the pooled data from three control replicates (each with mean subtracted) to represent the random fluctuation. To validate the assumption, the Ljung-Box test [93] was used to test the potential serial correlation (randomness). Next, the normality condition for individual replicate of control group was tested using Shapiro-Wilk test [94]. Finally the homogeneity of variances across three replicates was assessed using Bartlett's test [95]. For all tests the p-value was greater than 0.05, indicating the corresponding assumptions hold at the 95% confidence level. After validating all assumptions, variances from three control replicates were pooled to estimate one single variance to represent the fluctuation.

## 2.4. Results and discussion

# 2.4.1. Characterization of dispersed silica-core nanoparticles prior to exposure to tBLM

Figure 2.3 shows effective diameter (Figure 2.3 (A)) and zeta potential (Figure 2.3 (B)) of bare, carboxyl functionalized, and amine functionalized silica nanoparticles before interaction with the tBLM. Bare silica had a diameter of 51.9±6.5 nm and a zeta potential of -14.8±3.0 mV. Carboxyl functionalized silica had an effective of 69.9±4.4 nm and zeta potential of -16.0±3.0 mV, respectively. Amine functionalized silica had an effective diameter 111.0±2.7 nm and a zeta potential (-29.7±1.7 mV). Two-sample t test indicated that the average size and zeta potential values of amine silica were significantly different from those of either bare silica or carboxyl silica, while carboxyl silica did not show a difference from bare silica for size or zeta potential. The unexpected larger size and negative charge of the amine functionalized nanoparticles is believed to be due to cross-linking of two or more nanoparticles via adsorption of a multivalent anion onto the aminated surface. Candidate multivalent anions include  $SO_4^{2-}$ , which was the counterion for the Cu<sup>2+</sup> click chemistry catalyst, and EDTA<sup>4-</sup>, which was added in excess to remove the Cu<sup>2+</sup> catalyst following the reaction. Stable adsorption of oppositely charged polyelectrolytes has been reported to reverse the zeta potential of charged particles and to encourage aggregation by creating ionic bridges between adjacent particles [96].



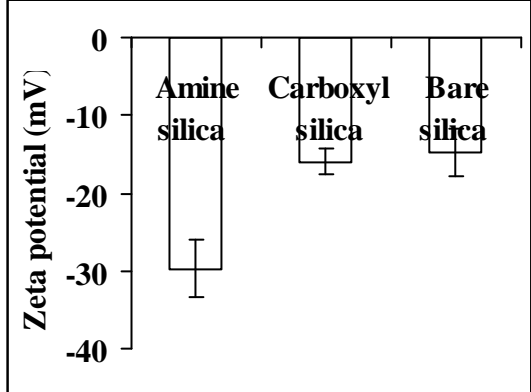


**Figure 2.3:** Size distribution (A) and zeta potential (B) of silica-core nanoparticles prior to exposure to tBLM. An asterisk indicates significant difference between effective diameter or zeta potential of carboxylic acid or bare silica and amine silica.

#### 2.4.2. Electrochemical characterization of tBLM

A BLM's lipid core blocks ion diffusion and thereby provides biomembranes with inherently high  $R_m$  values (order of M cm²). Molecules that disrupt or induce pores in BLM, such as channel proteins, ionophores, and some bacterial toxins, reduce  $R_m$  while maintaining membrane capacitance roughly constant [97-99]. Fitting the equivalent circuit model (Figure 2.3 (A)) to a typical set of tBLM impedance data gave an  $R_m$  value of 1.5 M cm² and a  $C_m$  value of 0.84  $\mu$ F/cm² (Figure 2.3 (B)). These values compare favorably with literature values in a range between 0.1 ~ 15 M cm², [21, 38, 57, 68, 97, 98], providing further evidence of a highly insulating and well formed tBLM.

## 2.4.3. AFM imaging of tBLM

A tapping-mode AFM image of a DPPTE/DOPC tBLM in DI water (Figure 2.4 (A)) follows topography of the bare gold substrate (Figure 2.4 (B)). The tBLM's surface roughness was 1.16±0.00032 nm, agreeing well with the reported roughness (0.9±0.2 nm) of a densely packed tBLM [100].

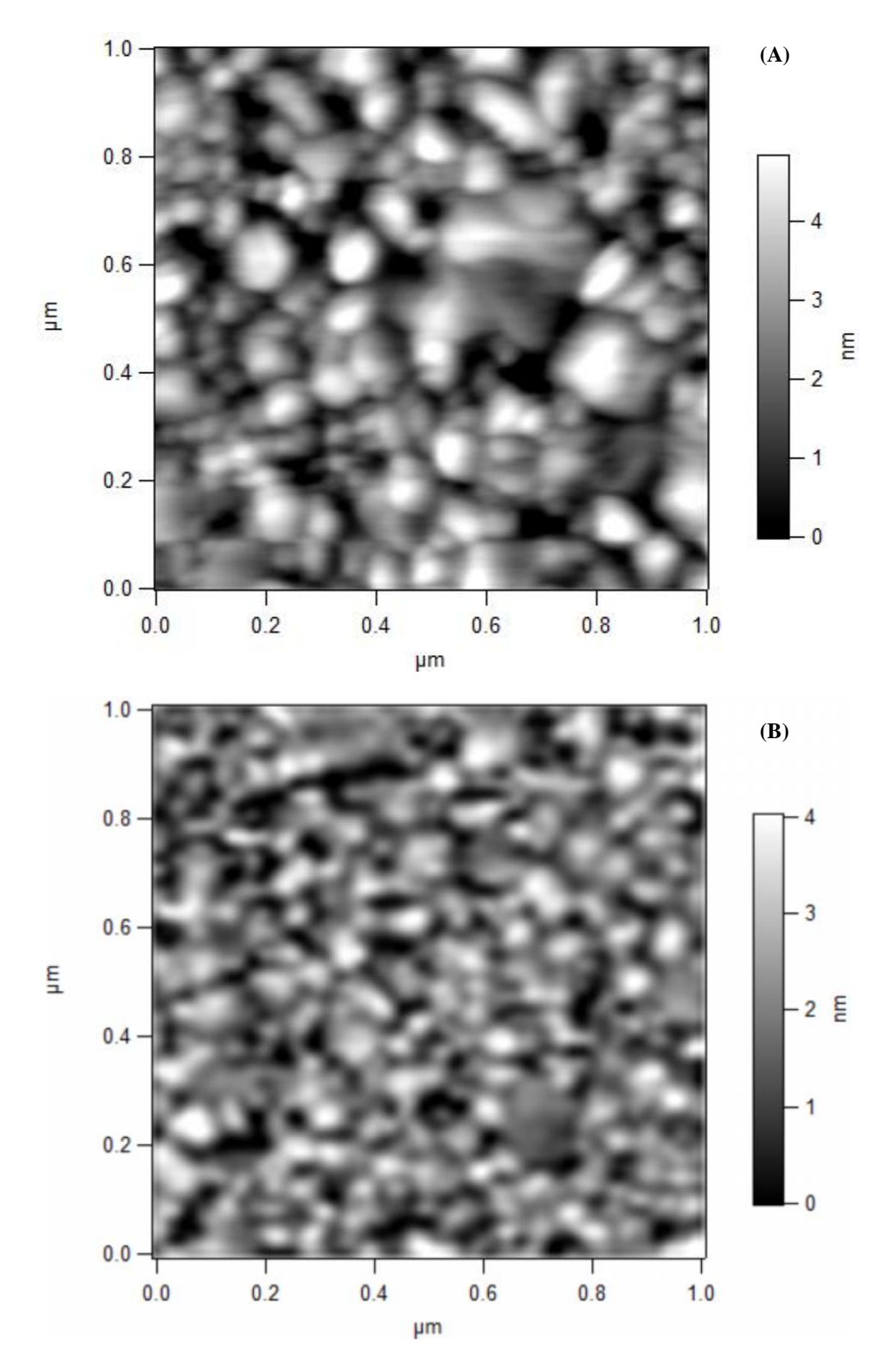
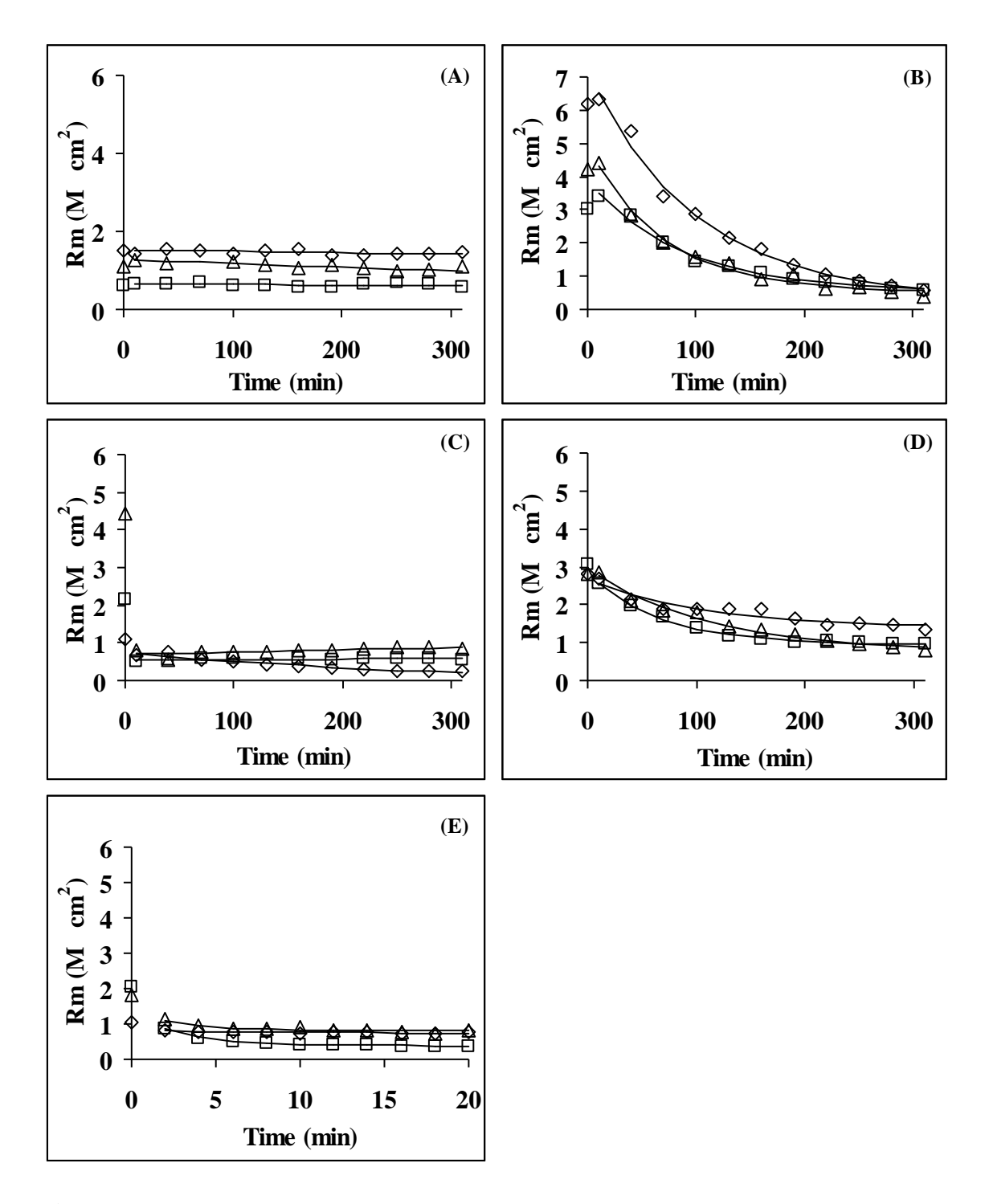


Figure 2.4: AFM images of tBLM in DI water (A) and on bare gold (B)

Since the roughness of bare gold substrate was  $1.12\pm0.0085$  nm and is not statistically different from that of the tBLM, this is consistent with a conformal BLM that is uniform and homogeneous. Moreover, resistivity of tBLM which is on the order of  $10^{12}$  cm, much higher than that of 10 mM KCl solution (~70 cm). The ratio of tBLM resistivity over KCl resistivity is a key factor in determining the minimum defect area fraction of tBLM that can dramatically reduce  $R_m$  value of tBLM. For example, the fraction as low as  $1.8\times10^{-13}$  of a total tBLM area of 0.4 cm<sup>2</sup> could result in 50% decrease in  $R_m$  value of a perfect tBLM. Therefore, it is very unlikely that the variation in height profile of tBLM due to existing holes given the high impedance shown in Figure 2 (B).

# 2.4.4. Surface functional group effects of silica-core nanoparticles on membrane resistance of tBLM

Figure 2.5 (A) shows triplicate R<sub>m</sub> vs. time curves for the control runs performed without nanoparticles, as well as the runs conducted with 300 μg/mL of silica-core nanoparticles having different functional groups. Ljung-Box test shows all p-values (Table 2.1) greater than 0.05 for control groups at lags ranging from one to five so that the serial correlation shows non-significance and randomness assumption holds well. Thus, observations can be treated as random samples for each of three replicate of control groups. Similarly, the Shapiro-Wilk test shows non-significance (p-value 0.84, 0.25 and 0.90, respectively), indicating that the normality assumption holds for all three replicates. Then, the Bartlett's test of homogeneity of variances shows non-significance (p-value 0.06), and the three replicates are roughly considered to have the same variance. Thus, the data from individual replicates were pooled to obtain the common standard deviation, which represents the fluctuation level to be 0.062 M cm² with 95% confidence interval.



**Figure 2.5:** Membrane resistance time profiles during tBLM interaction with 300  $\mu$ g/mL bare and functionalized silica-core nanoparticles in 10 mM KCl. The addition of (A) an aliquot of water (control), (B) carboxyl functionalized silica, (C) amine functionalized silica, (D) bare silica, and (E) amine functionalized silica nanoparticles was performed immediately after first  $R_m$  recorded for each replicate. Open points are experimental values, and curves are optimized exponential model fits.

**Table 2.1:** Ljung box test p values for control groups at different number of lags

	Lag = 1	Lag = 2	Lag = 3	Lag = 4	Lag = 5
Control experiment-1	0.74	0.31	0.37	0.52	0.24
Control experiment-2	0.51	0.60	0.23	0.32	0.49
Control experiment-3	0.07	0.14	0.11	0.19	0.13

Although R<sub>m</sub> values reported vary from 0.1 to 15 M cm<sup>2</sup>, R<sub>m</sub> values of tBLM formed using various lipids are, generally speaking, on the order of M cm<sup>2</sup> [32, 101]. The large variation of R<sub>m</sub> values observed from control experiments and experiments before ENM addition is believed to result from differences of roughness of gold substrate after piranha cleaning [97]. Piranha solution composed of concentrated sulfuric acid and hydrogen peroxide is a strong oxidizing agent, so cleaning the surface of gold substrate is commonly achieved by piranha treatment. Although piranha treatment can enhance the electrocatalytic activities of gold electrode, AFM and SEM studies also demonstrated piranha treatment could cause substantial increase of gold electrode roughness [102, 103].

In all runs shown in Figures 2.5 (B)-(D), the final  $R_m$  values were smaller than the initial values, indicating an enhanced ability of ions to traverse the tBLM after exposure to the silica-core nanoparticles. For the bare silica and carboxyl functionalized nanoparticles, the rates of  $R_m$  decline could be accurately traced using a 30 min interval between  $R_m$  measurements. However, for the amine functionalized nanoparticles, virtually the entire drop in  $R_m$  occurred within the first 30 min (Figure 2.5 (C)). To more accurately estimate the exponential rate constant (k in Eqn. 1) for these nanoparticles, EIS was performed over a smaller range (from 0.1 Hz to 10,000 Hz), reducing the

sampling period by a factor of 15. The use of a two minute sampling interval allowed the rate of  $R_m$  decline to be more clearly resolved for the amine silica (Figure 2.5 (E)).

Clustering analysis was then used to test the hypothesis that the tBLM method could distinguish patterns of biomembrane disruption caused by nanoparticles that had identical amorphous-silica cores but different surface functional groups. Eqns. 1 and 2 were fit to  $R_m$  vs. time profiles (Figure 2.5). Then, the clustering analysis was applied to the resulting three values of  $(R_i\text{-}R_f)$ , k, and  $R_m\%$ . The dendrogram generated from hierarchical clustering using a parameter matrix containing best-fit  $(R_i\text{-}R_f)$ , k, and  $R_m\%$  values (Figure 2.6) visually displays the degree of similarity between experiments. Numbers below the line indicate the sequence in which two objects are linked together, while numbers above the line are AU p values at every clustering step.

Although bare silica, carboxyl silica, and amine silica particles all caused a decrease in  $R_m$  that was well represented by an exponential curve, other trends in nanoparticle-induced  $R_m$  dynamics have also been observed. For example, when the same silica-core nanoparticles were functionalized with short polyethylene glycol (PEG) functional groups, the resulting PEG functionalized silica nanoparticles triggered a minor increase in the tBLM resistance (data not shown). Because these  $R_m$  trajectories were poorly described by the exponential decay model (Eqn. 1) and were easily distinguishable from the trajectories of the other three silica-core nanoparticles, the PEG functionalized nanoparticle data were not included in the clustering analysis.

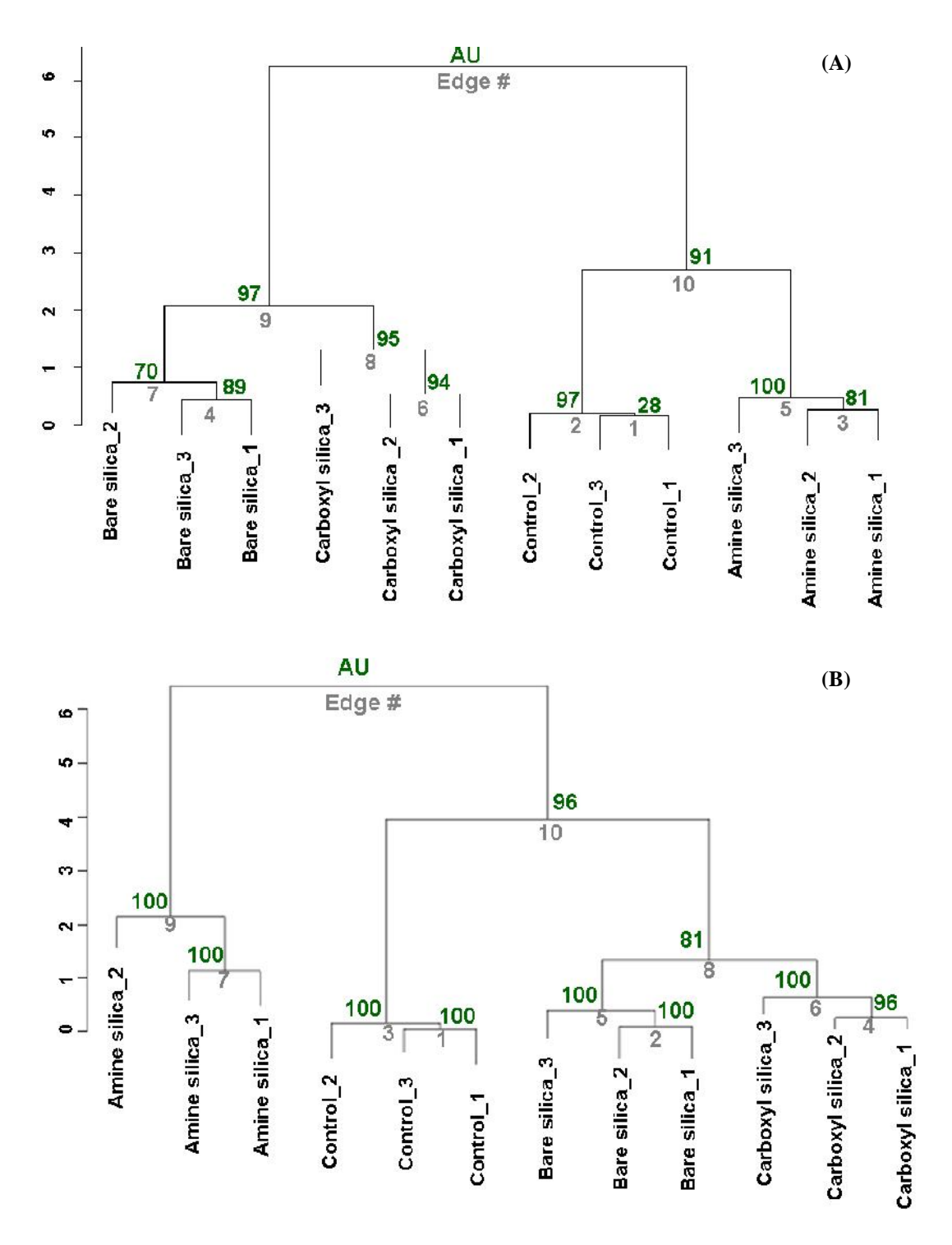


**Figure 2.6:** Hierarchical clustering dendrogram resulting from Ward's method analysis of Figure 5 data. Parameters for dendrogram in were analyzed (A) from data in Figures 2.5 (A)-(D), and (B) from data in Figures 2.5 (A), (B), (D), and (E). The sequence of clustering steps is shown below the line, and the AU p-value for each clustering step is shown above the line. The vertical axis is a measure of the distance between the members of each clustered set.

The dendrogram indicates that each type of nanoparticle clusters as a unique group, consistent with the hypothesis. When only  $R_m$  data acquired at 30-minute intervals (Figures 2.5 (A)-(D)) were used to calculate ( $R_i$ - $R_f$ ), k, and  $k_m$ % values, the amine silica nanoparticles clustered most closely with the control group (Figure 2.6 (A)), because 30-min sampling interval did not capture the rapid exponential decline in  $k_m$  that is apparent in Figure 2.5 (E). However, when the two-min sampling interval  $k_m$  profiles for amine silica nanoparticles (Figure 2.5 (E)) were used, the resulting dendrogram (Figure 2.6 (B)) showed little similarity between the amine silica nanoparticles and the other three cases. Also, Figure 2.6 (B) shows higher AU p values than those in Figure 2.6 (A), indicating a greater degree of certainty that the clusters are distinct.

The simple exponential model (Eqn. 1) did a reasonable job of describing the  $R_m$  trajectories for the bare, carboxyl functionalized, and amine functionalized nanoparticles, and the regression constants are physically meaningful. Specifically, k, ( $R_i$ - $R_f$ ), and  $R_m$ %, represent the rate of change, total  $R_m$  change, and the fractional change in  $R_m$  as a function of time. This physical interpretation provides a framework by which nanoparticles may be ranked in order of potency for biomembrane disruption. The parameters regression constants for amine, carboxyl, and bare silica, combined with the observation that PEG functionalized silica-core nanoparticles did not reduce  $R_m$ , yield the following potency rank for functionalized amorphous silica EMN: amine > carboxyl ~ bare silica > PEG. The hierarchical clustering method presented here could be extended to models other than Eqn. 1, such as one capable of describing an initial increase in  $R_m$  followed by a decrease. In addition to different models, different combinations of variables could be analyzed in the clustering analysis. We found that including all three

variables: k,  $(R_i-R_f)$  and  $R_m\%$  allowed effects of different nanoparticles to be better distinguished than when only two (k and either  $(R_i-R_f)$  or  $R_m\%$ ) were used.

The dendrogram's ability to cluster silica-core nanoparticles according to their surface functional groups confirms the study's central hypothesis. Thus, this study demonstrates for the first time that a tBLM method can measure time-dependent changes in tBLM  $R_{\rm m}$  values with sufficient sensitivity to discern differences in potency of BLM disruption by ENM that are identical except for their surface functional groups.

Mechanistic insight into ENM-BLM interactions can be difficult to discern when using intact cell membranes, because the nanoparticles may interact with intact cell membranes through a variety of mechanisms [59], some of which involve protein-mediated events. For example, in receptor-mediated endocytosis, highly selective membrane receptor proteins may bind a target macromolecule and trigger endocytosis [104]. Results of this study showed not only that silica-core nanoparticles can disrupt biomembranes through direct action on the lipid bilayer, as evidenced by a significant reduction in the tBLM's  $R_{\rm m}$  value, but that the potency of disruption can be significantly affected by the surface chemistry of the otherwise identical nanoparticles. This finding suggests it may be possible to achieve highly selective macromolecule-biomembrane interactions without the need for protein-mediated processes.

# 2.4.5. Effects of tBLM exposure on aggregation of silica-core nanoparticles

Figure 2.7 (A) shows effective diameter of bare, amine functionalized, and carboxyl functionalized nanoparticles measured before and after interaction with tBLM. Both two-sample t test and Wilcoxon rank sum tests indicated a significant difference between the

size of bare and amine functionalized silica before and after exposure to the tBLM. However, the size of carboxyl functionalized silica did not change significantly during tBLM exposure.

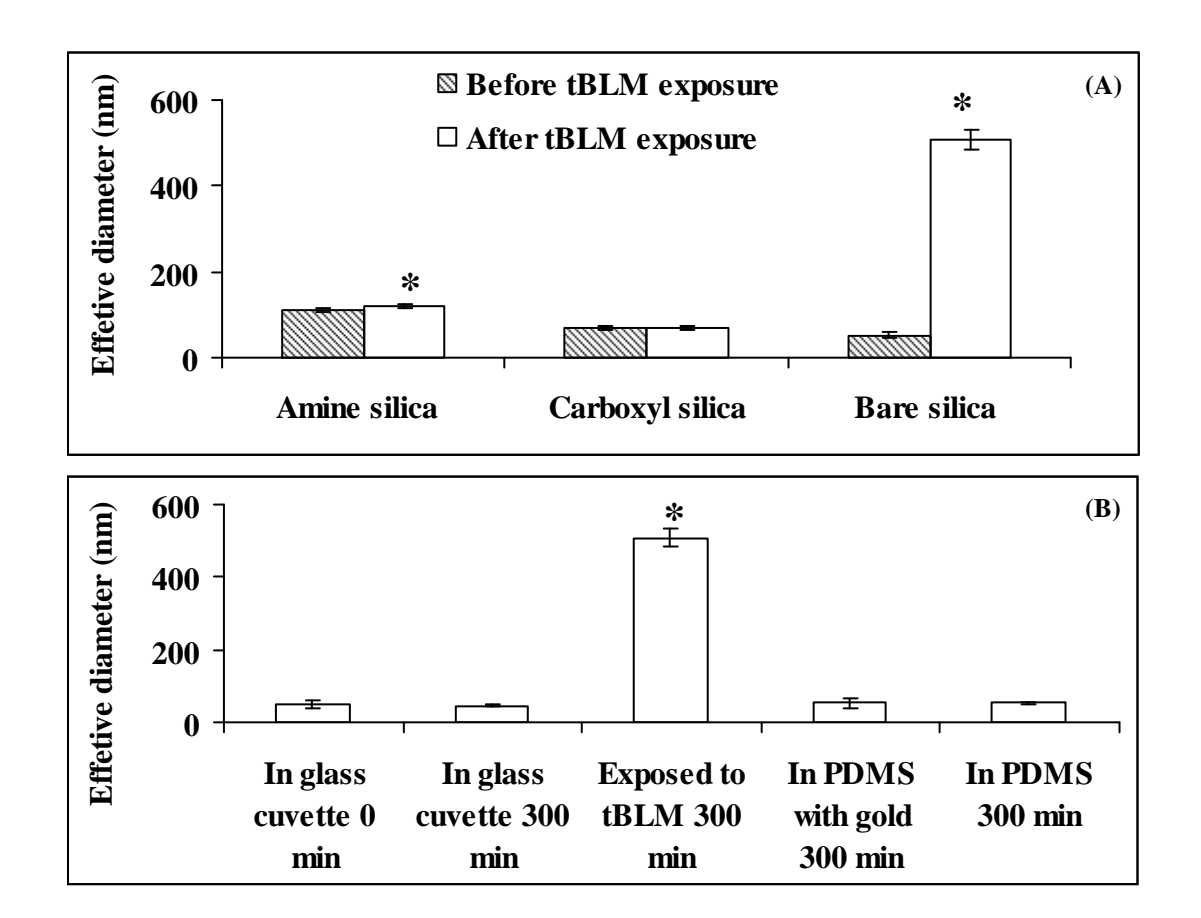


**Figure 2.7:** (A) Effective diameter of silica-core nanoparticles prior to and after 5 h interaction with tBLM, measured by DLS. An asterisk indicates significant difference of effective diameter of silica nanoparticles between before tBLM exposure and after. (B) Effective diameter of bare silica nanoparticles under various conditions by DLS. The asterisk indicates the size of bare silica measured in the presence of tBLM is significantly higher than that measured in all other conditions.

Control experiments were conducted to identify whether the apparent aggregation of bare silica nanoparticles may have been due to factors other than the tBLM exposure. Final particle sizes following 300 min contact of the bare silica nanoparticles with the glass cuvettes in which particle size was measured, the PDMS well, the PDMS well with

a gold electrode, and the PDMS well with a gold electrode covered with a tBLM are shown in Figure 2.7 (B). Statistical analysis indicated no significant difference before and after exposure of the bare silica nanoparticles to all components tested, except the tBLM.

At this time, molecular interaction mechanisms between the ENM and tBLM are insufficiently understood to unambiguously map the R<sub>m</sub> trajectories into detailed knowledge of ENM-biomembrane interactions. Additional research is needed to calibrate the tBLM in terms of underlying mechanisms. Nevertheless, trends in the experimental results presented here provide reproducible measures of molecular-scale molecular interactions. One hypothesis to explain the decline in R<sub>m</sub> is that nanoparticles adsorb to the tBLM and then remove lipids, thereby generating or enlarging defects in the tBLM through which ions could traverse the tBLM. This hypothesis is consistent with the observed increase in effective diameter of bare and amine functionalized silica following exposure to the tBLM. Lipid transferred from the tBLM to the nanoparticles could trigger nanoparticle cross-linking and aggregation. The hypothesis is also consistent with reports that PAMAM dendrimers removed lipid from an sBLM on a carbon electrode, thereby reducing R<sub>m</sub> measured by EIS and increasing Faradaic current measured by cyclic voltammetry [105]. Additional evidence for BLM lipid removal has been provided by AFM images showing holes in sBLM on mica induced by dendrimers [60, 106, 107], as well as by visible microscopy images showing disruption of a sBLM by semihydrophobic nanoparticles.

### 2.5. Conclusions

The novel method presented here integrates EIS to monitor the  $R_{\rm m}$  of a tBLM during nanoparticle exposure, an exponential-decay model to describe  $R_{\rm m}$  vs time

trajectories, and statistical hierarchical clustering to generate a dendrogram that graphically depicts similarities of time trajectories due to different nanoparticles. The R<sub>m</sub> profiles obtained while challenging a tBLM composed of DPPTE/DOPC with three types of amorphous-silica-core nanoparticles (bare, amine functionalized, and carboxyl functionalized) could be reasonably described with a decaying exponential model. The resulting dendrogram successfully clustered each set of replicates, confirmed the study's central hypothesis that a tBLM-based method could be used to distinguish patterns of biomembrane disruption caused by nanoparticles that had identical amorphous-silica cores but different surface functional groups. The results also allowed the tBLMdisrupting potency of the surface functionalized silica nanoparticles to be ranked in the decreasing order amine > carboxyl ~ bare silica, with PEG functionalized nanoparticles not reducing the R<sub>m</sub>. These findings indicate that nanoparticle surface chemistry (e.g., click chemistry) can be used to modify the nanoparticles' surface functional group and thereby modulate nanoparticle-biomembrane interactions. Changes in the surface functional group also influenced the tendency of silica nanoparticles to aggregate following exposure to a tBLM; bare silica nanoparticles aggregated significantly, while carboxyl functionalized nanoparticles showed no change in diameter. The methods presented here are generic and could be applied to a wide range of nanoparticles and tBLM compositions to test other hypotheses about nanomaterial interactions with biomembranes.

## 3. tBLM INTERTACTION WITH PNP

## 3.1. Abstract

Molecular interactions between engineered nanomaterials (ENM) biomembranes are not well understood. This study investigated the effects of particle size and surface functional group on polystyrene nanoparticles (PNP) potency for biomembrane disruption. Electrochemical impedance spectroscopy (EIS) was used to measure changes in the R<sub>m</sub> of a tethered bilayer lipid membrane (tBLM) composed of 1,2-dioleoyl-sn-glycero-3-phosphocholine (DOPC) following PNP exposure. All PNP tested triggered a decline in the R<sub>m</sub> that could be described using an exponential-decay model. Statistical hierarchical clustering analysis of two model parameters (exponential rate constant and fractional loss of R<sub>m</sub>) could distinguish between the PNP based on both size and surface functional group. For carboxylate (COOH) modified nanoparticles, 20 nm PNP were more potent in reducing R<sub>m</sub> than 100 nm PNP. However, for amidine modified nanoparticles, 120 nm PNP were more potent in reducing R<sub>m</sub> than 23 nm PNP. The COOH modified PNP were more potent in reducing R<sub>m</sub> than amidine modified PNP, which tended to aggregate following exposure to a tBLM. Ultra performance liquid chromatography-mass spectroscopy analysis suggested that the aggregation may have been triggered by DOPC that was removed from the tBLM by the amidine PNP.

## 3.2. Introduction

The expectation of elucidating and better apprehending the mechanisms of ENM effects on biomembranes has driven numerous studies and efforts. The inherent challenge lies in how ENM cross biomembranes [16]. The fluidity of the lipid bilayer interior

contributes more significantly than near the glycerol backbone in determining the permeability of ENM. On the other hand, the dynamic properties of lipid bilayers are also affected in the presence of ENM.

DOPC is a major constituent of many biomembranes that readily forms liquidphase BLM at room temperature, and is well suited to form biomimetic interfaces that mimic biomembranes [108]. PNP are well suited as model ENM to elucidate ENMbiomembrane interactions. Key properties of PNP, such as size and surface functionality, can readily be customized. PNP have been investigated for a wide range of commercial applications including drug delivery, food additives and other pharmaceutical implementations [109-111]. PNP have been shown to activate ion channels (K+ and Cl-) when interacting with human airway epithelial cells, thereby interfering with signaltransduction pathways [112]. PNP having different size and surface functionalization have been shown to exhibit cytotoxicity by causing G1 phase delay and disrupting membrane integrity [113]. Cationic PNP were shown to induce mitochondrial damage and ATP depletion [114]. Transcellular trafficking of positively charged, amidinemodified PNP (amidine PNP) across primary rat alveolar epithelial cell monolayers was shown to occur 20-40 times faster than for negatively charged, COOH-modified PNP (COOH PNP) [80, 115]. The primary mechanism of this PNP translocation was thought to be PNP diffusion through the BLM of the cell plasma membranes. Moreover, both COOH PNP and amidine PNP have been shown to induce ion-selective pores in planar BLM [116]. However, interactions of PNP with tBLM systems have not yet been reported. In addition the ability of the tBLM method to distinguish between polymeric

ENM (e.g., PNP) based on their size and surface functionality has not yet been established.

This chapter focuses on characterization of interactions between DOPC tBLM and PNP for two functional groups (COOH and amidine) in two sizes (20 and 100 nm). EIS was used to monitor changes in the tBLM's R<sub>m</sub> following exposure to the various PNP. Ultraperformance liquid chromatography-mass spectroscopy (UPLC-MS) analysis was used to explore the role of DOPC in differential aggregation of COOH PNP and amidine PNP observed after exposure to the tBLM. The methods's ability to distinguish between two different particle sizes and surface groups was assessed hierarchical clustering analysis.

## 3.3. Materials and Methods

#### 3.3.1. Characterization of functionalized PNP

Fluorescent amidine PNP (23 nm and 120 nm in diameter) and fluorescent COOH nanoparticles (20 nm and 100 nm in diameter) were purchased from Invitrogen (Eugene, Oregon). Effective diameter of COOH and amidine PNP prior to and after interaction with tBLM were measured by 90 Plus nanoparticle size analyzer (Brookhaven Instruments Inc., Holtsville, NY), respectively. Zeta potential of tested PNP was determined by Zeta potential analyzer (Brookhaven Instruments Inc., Holtsville, NY). Dynamic and phase analysis light scattering measurements were performed at 25°C in 10 mM and 1 mM KCl, respectively. COOH and amidine PNP were ultrasonicated for 10 min. Then they were transferred to PDMS reservoir and exposed to tBLM in 10 mM KCl to give a final concentration of 100 µg/mL.

#### 3.3.2. Fabrication of tBLM

A tBLM was deposited on freshly cleaned gold coated on silicon wafer in two-step process, as described in Chapter 2. Briefly, gold electrodes were cleaned in fresh piranha solution (51%  $H_2SO_4$ : 30%  $H_2O_2 = 7:3$ ) for 30 s, washed with deionized water and then dried in nitrogen. A SAM of DPPTE chemically adsorbed on gold electrode to form lower leaflet of tBLM by dipping the gold substrate into 1 mM ethanolic DPPTE solution for 1 h. Then gold electrode was washed by ethanol and dried in nitrogen. SAM coated gold electrode was incubated in DOPC liposome solution in a PDMS slab. The area of tBLM was  $0.48 \text{ cm}^2$ .

#### 3.3.3. EIS characterization of tBLM

EIS was performed in a frequency interval ranging from 0.01 Hz to 10,000 Hz at 0 V bias potential relative to an Ag/AgCl reference electrode with ac perturbation amplitude of 5 mV using CHI660B electrochemical workstation (CH Instruments Inc., Austin, TX). The same equivalent circuit in Figure 2.2 (A) was employed to fit the impedance spectra. Electrical resistances of the tBLM were measured by EIS for 5 h in triplicate prior to, and after exposure to 100 μg/mL PNP.

### 3.3.4. DOPC analysis by UPLC-MS

Analysis of DOPC was conducted on a Xevo G2-S UPLC-Time of Flight MS (Waters, Milford, MA) in a positive electrospray ionization mode, coupled with Acquity UPLC consisting of binary pumps. An Ascentis Express Carbon reversed phase column (100×2.1 mm, 2.7 μm, Sigma-Aldrich) was used to separate the DOPC lipid extract. The column temperature was kept at 30 °C while the capillary energy was 2.14 kV. A 10-μL solution was injected through an autosampler and eluted at a flow rate of 0.4 mL/min

using mobile phase system consisting of solvent A (10 mM NH<sub>4</sub>CH<sub>3</sub>COO) and B (50% CH<sub>3</sub>OH and 50% CH<sub>3</sub>CN) in a linear gradient, shown in Table 3.1.

**Table 3.1:** Mobile phase flow gradient for UPLC-MS analysis: solvent A (10 mM NH<sub>4</sub>CH<sub>3</sub>COO) and B (50% CH<sub>3</sub>OH and 50% CH<sub>3</sub>CN). The percentage represents the volumetric ratio of solvent A over solvent B.

Time (min)	Flow (mL/min)	% A	%B
0	0.4	30	70
20	0.4	0	100
25	0.4	0	100
25.01	0.4	30	70
28	0.4	30	70

### 3.3.5. Statistical analysis

All  $R_m$  of tBLM versus time profile after addition of COOH or amidine PNP was fitted using an exponential function, as described previously [22]. A pattern matrix containing a total of n=12 experiments as rows, and p=2 features, b and  $R_m$ % for each experiment as columns, was analyzed using hierarchical clustering procedures in R software (Version 2.13.2: The R Foundation for Statistical Computing), to evaluate the similarity between experiments. Also, Ward's method was used to determine which clusters should be linked together at each step.

A difference was considered insignificant at p<0.05 by applying two-sample t test assuming unequal variance when comparing size and surface charge of COOH and amidine PNP.

#### 3.4. Results

#### 3.4.1. Characterization of COOH and amidine PNP

Effective diameters of COOH PNP and amidine PNP were measured by DLS in 10 mM KCl (Table 3.2). Effective diameters of COOH PNP were  $102.3 \pm 1.0$  nm and  $20.4 \pm 0.6$  nm. Diameters for these PNP given by the manufacturer (determined by transmission electron microscopy) were 100 nm and 20 nm, respectively. For amidine PNP, the effective diameters were  $93.2 \pm 1.3$  nm and  $20.6 \pm 1.5$  nm, and the manufacturer-provided diameters were 120 nm and 23 nm, respectively. Based on the DLS values, a two-sample t test indicated that the size was significantly different between 20 and 100 nm COOH PNP, as well as between 23 and 120 nm amidine PNP. Also, the size of COOH PNP labeled 100 nm was significantly different from that of amidine PNP labeled as 120 nm. However, there was no significant size difference between the 20 nm COOH PNP the 23 nm amidine PNP.

**Table 3.2:** Effective diameter of COOH and amidine PNP in 10 mM KCl measured by dynamic light scattering at 25 °C.

PNP	Effective Diameter (nm)
100 nm COOH PNP	$102.3 \pm 1.0$
20 nm COOH PNP	$20.4 \pm 0.6$
23 nm Amidine PNP	$20.6 \pm 1.5$
120 nm Amidine PNP	$93.2 \pm 1.3$

Zeta potentials of functionalized PNP (Table 3.3) were  $-32.2 \pm 3.3$  mV for 100 nm COOH PNP,  $-29.8 \pm 2.1$  mV for 20 nm COOH PNP,  $38.3 \pm 6.2$  mV for 120 nm amidine PNP and  $26.6 \pm 3.8$  mV for 23 nm amidine PNP. Based on these values, there was a significant difference in zeta potential between the two sizes of amidine PNP, but not between the two sizes of COOH PNP.

**Table 3.3:** Zeta potential of COOH and amidine PNP in 10 mM KCl measured by Phase analysis light scattering at 25 °C.

PNP	Zeta Potential (mV)	
100 nm COOH PNP	$-32.2 \pm 3.3$	
20 nm COOH PNP	$-26.8 \pm 4.8$	
23 nm Amidine PNP	$26.6 \pm 3.8$	
120 nm Amidine PNP	$38.2 \pm 6.2$	

#### 3.4.2. EIS characterization of tBLM

The EIS spectrum of a typical tBLM used in this study is shown as a Bode plot (logarithm phase diagram versus logarithm frequency) in Figure 3.1. This figure has regimes dominated by different electrical characteristics:  $R_m$ -dominated in the low frequency range (< 1 Hz) and capacitance-dominated in mid to high frequency range (1 Hz ~ 1000 Hz) [117]. The equivalent circuit model fit to the impedance data had an  $R_m$  value of 2.1 M cm<sup>2</sup> and a membrane capacitance ( $C_m$ ) value 1.1  $\mu$ F/cm<sup>2</sup>. Both values are in the range reported for a highly insulating tBLM formed on a gold substrate[101, 118].

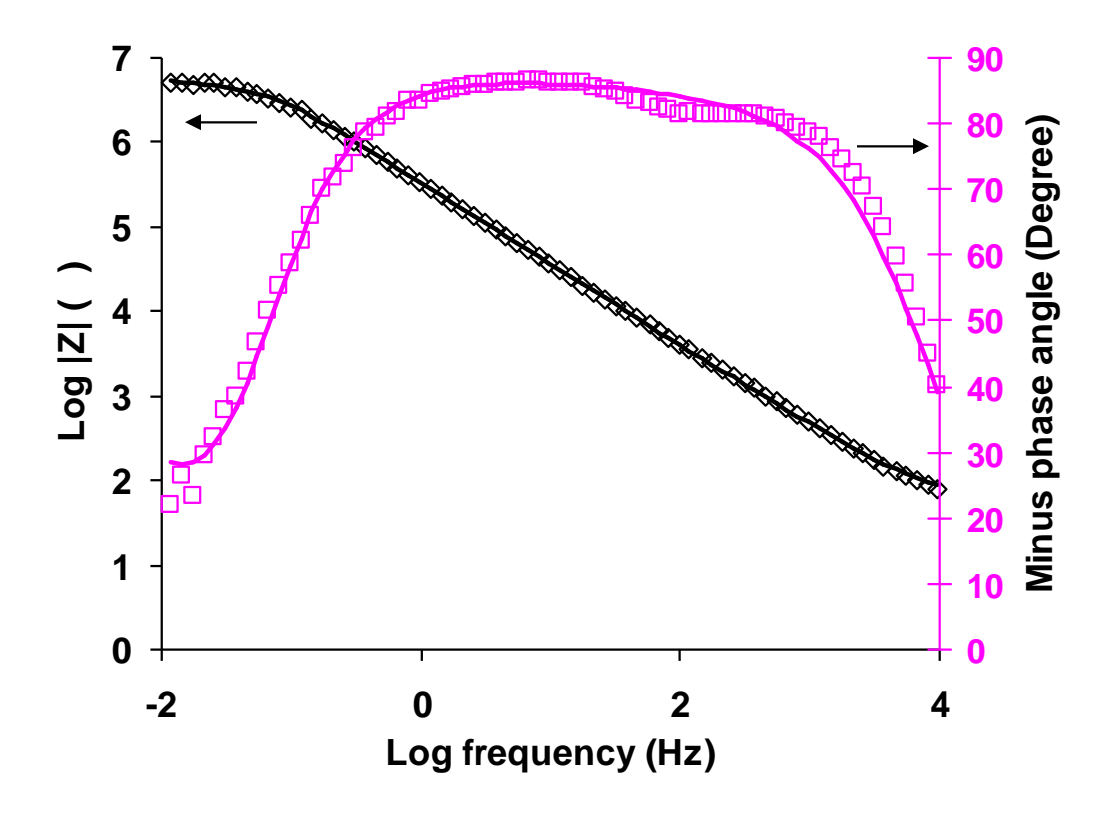


**Figure 3.1:** Experimental and equivalent circuit-predicted EIS spectra of the tBLM formed on 0.48 cm<sup>2</sup> gold. Left vertical axis: log of impedance magnitude (diamonds). Right vertical axis: minus phase angle (squares). Solid curves are impedance curves simulated by the equivalent circuit using Zview software.

#### 3.4.3. Interaction of COOH and amidine PNP with tBLM

Triplicate  $R_m$  profiles extracted from EIS data over 310 min were obtained for 100 nm COOH (Figure 3.2 (A)), 20 nm COOH PNP (Figure 3.2 (B)), 23 nm amidine PNP (Figure 3.2 (C)), and 120 nm amidine PNP (Figure 3.2 (D)). In these experiments, the PNP were added immediately after the first data point was recorded. Solid lines in Figure 3.2 show the best-fit exponential decay curves [22]. All PNP tested triggered a decline in the  $R_m$  that could be described using an exponential-decay model. Based on the regression values for the b and  $R_m$ % constants (Figure 3.3), the 20 nm COOH PNP reduced  $R_m$  more rapidly than did the 100 nm COOH PNP, as evidenced by a more negative b value. The smaller COOH PNP particles gave a greater  $R_m$ % value. Amidine

PNP in both sizes reduced  $R_m$  to a plateau value, but the 120 nm amidine PNP caused a more rapid  $R_m$  decay than the 23 nm amidine PNP.

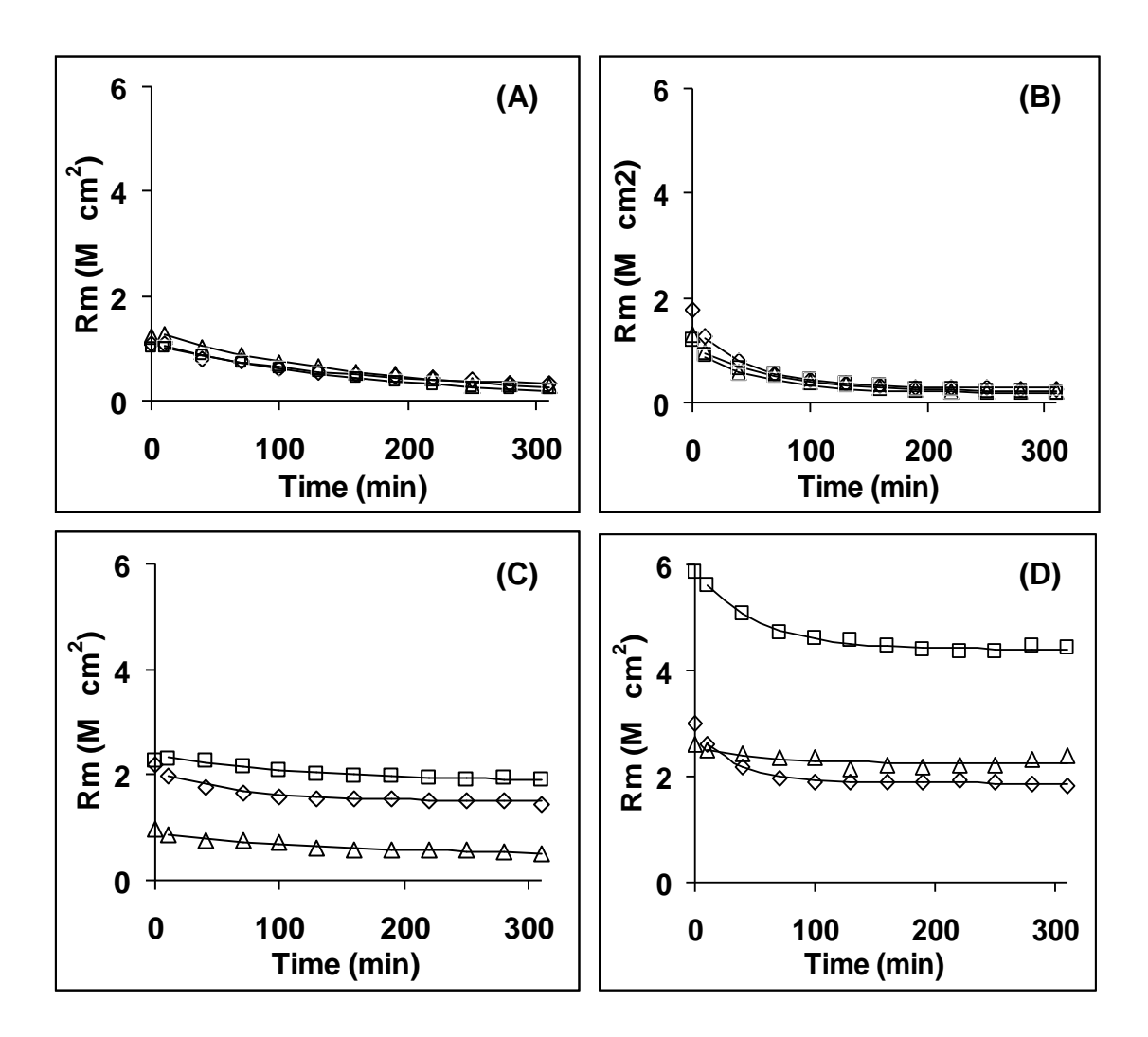


**Figure 3.2:**  $R_m$  profiles over time during tBLM interaction with 100 µg/mL PNP in 10 mM KCl. (A): 100 nm COOH PNP, (B): 20 nm COOH PNP, (C): 23 nm Amidine PNP and (D): 120 nm Amidine PNP.  $R_m$  was extracted from EIS data fitted by equivalent circuit model. Three replicates were done, labeled as open diamonds, squares and triangles. All solid curves were fitted  $R_m$  by a time dependent exponential model as  $R_m$ =a\*exp(b\*t)+c where a, b and c represent initial  $R_m$ , rate constant and final  $R_m$  after addition of PNP.

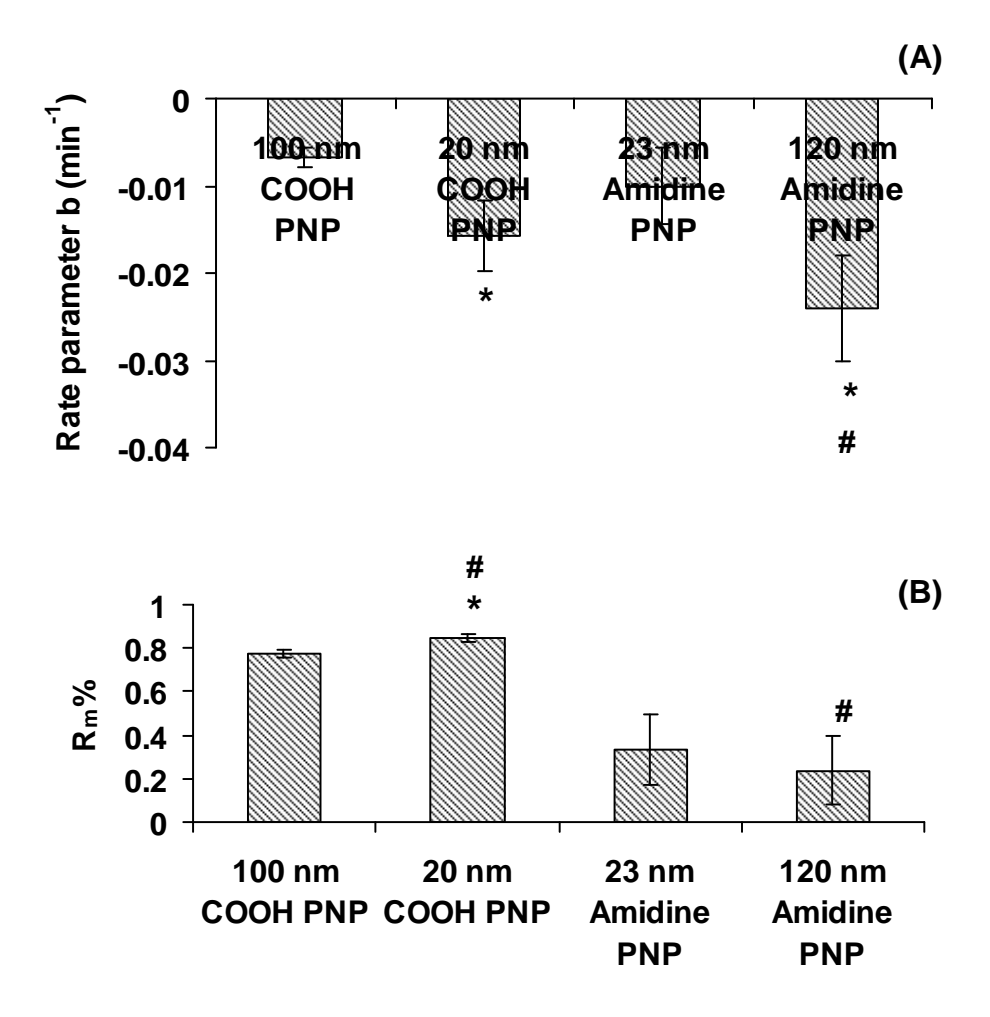


**Figure 3.3:** Rate parameter (A) and  $R_m\%$  (B) extracted using an exponential decay model and calculated from  $R_m$  profiles of COOH or amidine PNP interaction with tBLM in 10 mM KCl, respectively. The asterisk indicates statistical difference in rate parameter b or  $R_m\%$  when comparing two different sizes of PNP functionalized with either COOH or amidine. The pound sign indicates statistical difference in rate parameter b or  $R_m\%$  when comparing 20 nm COOH PNP and 23 nm amidine PNP or comparing 100 nm COOH PNP and 120 nm amidine PNP.

## 3.4.4. Hierarchical clustering analysis

The hierarchical clustering dendrogram (Figure 3.4) for the best-fit b and  $R_m\%$  constants displays the Euclidean distance between clustered objects as a measure of dissimilarity between samples and clusters. Samples that cluster at a smaller height are more similar (separated by less Euclidean distance) than samples that cluster at a greater

height. Each set of PNP triplicates having the same size and functional surface group clustered first. Next, PNP having the same functional group but different sizes clustered. Finally, PNP having different functional groups clustered. These results demonstrate that the tBLM method, with hierarchical clustering analysis based on two experimental parameters (b and  $R_m\%$ ), can distinguish patterns of PNP-BLM interaction according to both functional groups and size.

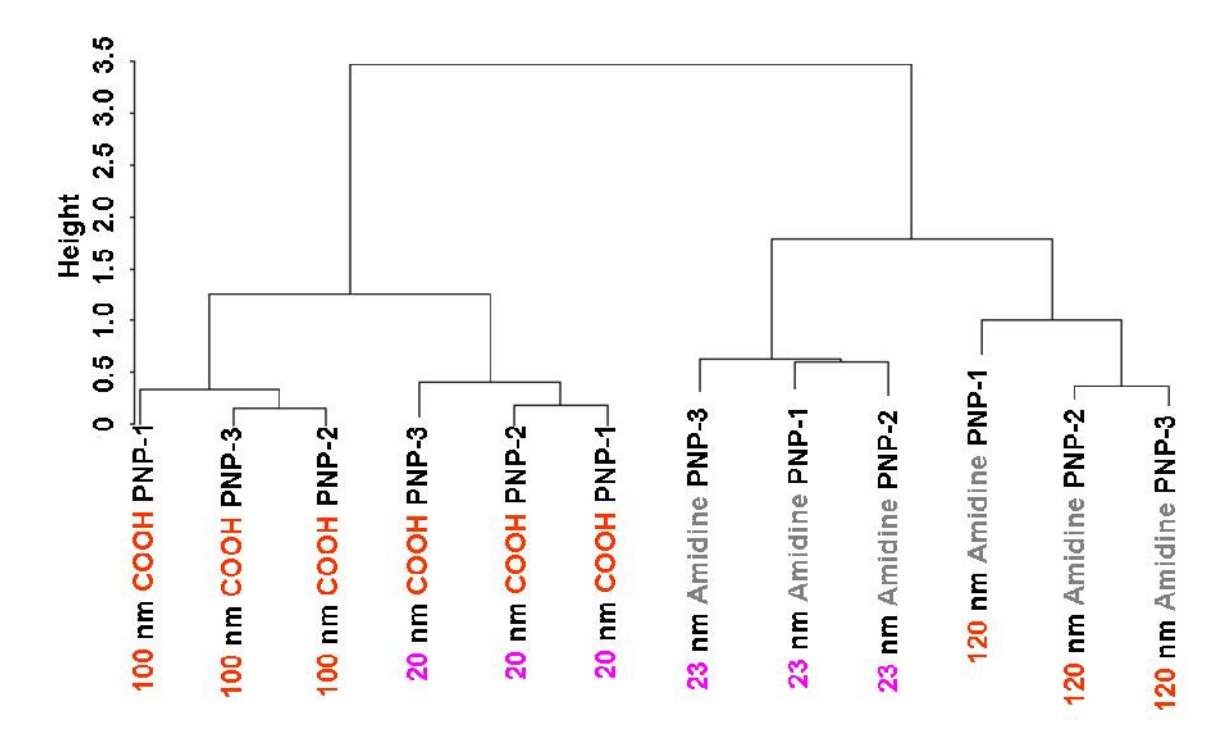


**Figure 3.4:** Hierarchical clustering dendrogram of 20 and 100 COOH, as well as 23 nm and 120 nm amidine PNP interaction with tBLM. Distances between objects when forming the clusters were calculated by Euclidean distance. Ward's method was used to evaluate distances between clusters and to determine which clusters should be linked together at each step.

## 3.4.5. Aggregation of amidine PNP

Particle size analyses (Figure 3.5) showed significant increases in effective diameter during the experiments for the amidine PNP but not the COOH PNP.

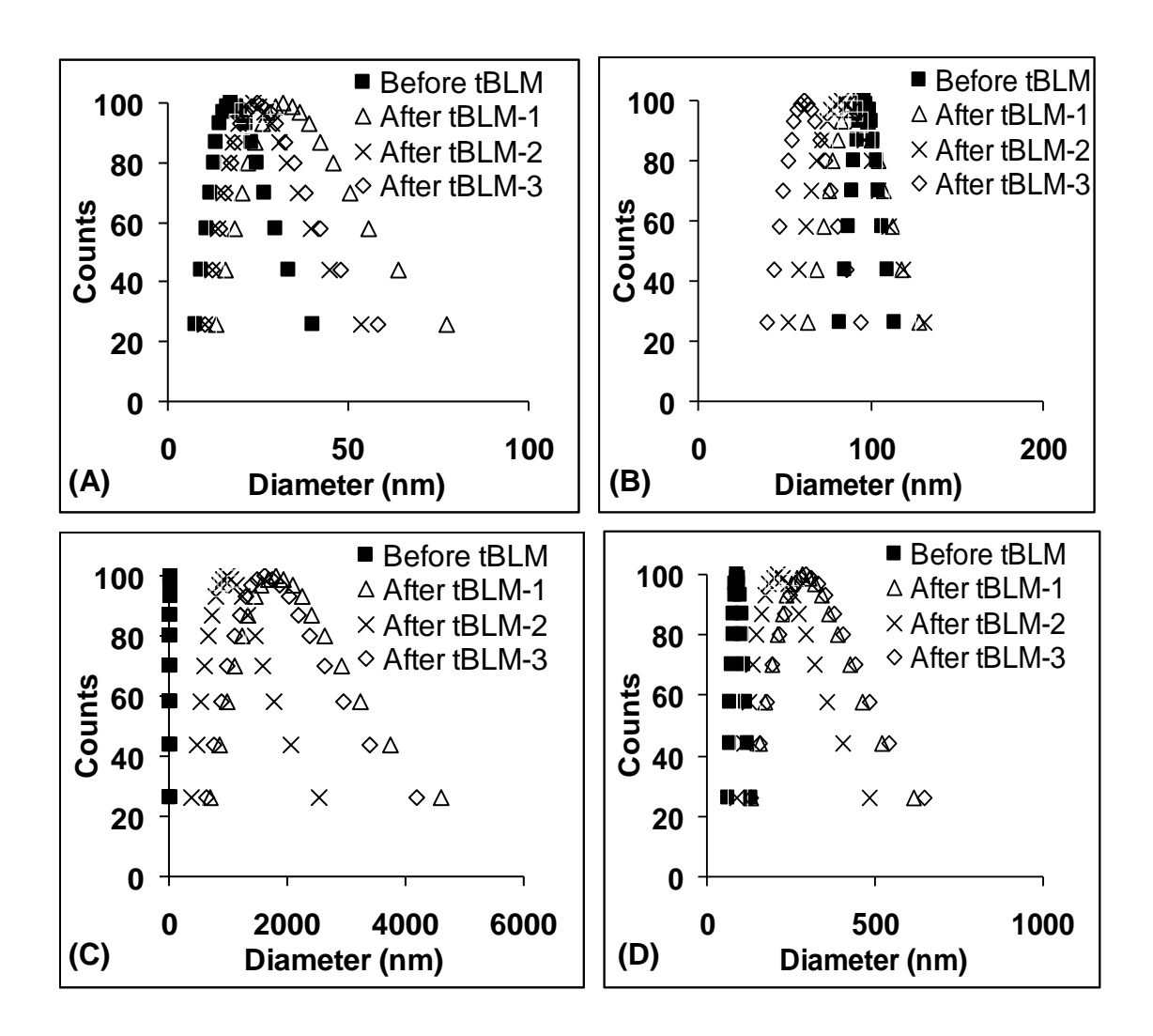


**Figure 3.5:** Size distribution of COOH and amidine PNP in 10 mM KCl prior to and after tBLM exposure for 5 hrs, measured by DLS at 25 °C. (A): 20 nm COOH PNP; (B) 100 nm COOH PNP; (C): 23 nm Amidine PNP and (D): 120 nm Amidine PNP.

The increases in effective diameter for amidine PNP following tBLM exposure were accompanied by visibly apparent aggregation, as evidenced by cloudy solutions (Figure 3.6 (A) and (B)), while solutions containing COOH PNP remained clear (Figure 3.6 (C) and (D)). The effective diameter increased about 50-fold for the 23 nm amidine PNP (Figure 3.5 (C)), but only about 3-fold for the 120 nm amidine PNP (Figure 3.5 (D)). Electrolyte and buffer concentrations are known to affect the rate and extent of

nanoparticle aggregation [26]. However, no aggregation was observed when the amidine PNP were incubated in the electrolyte solution (10 mM KCl) used for the EIS experiments, indicating that electrolyte concentration was not the sole factor triggering the aggregation.

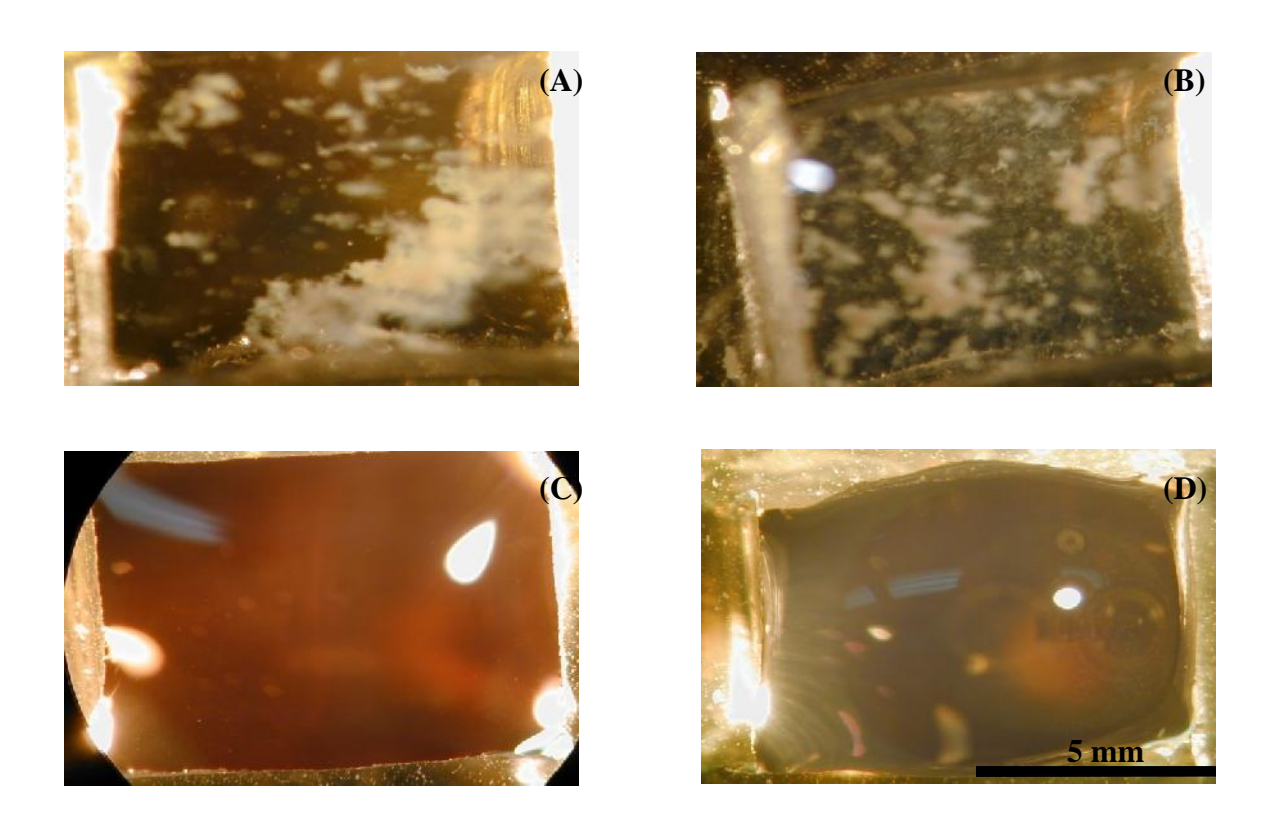


**Figure 3.6:** Images of PDMS reservoir containing functionalized PNP after exposure to tBLM for 5 h: (A) 23 nm Amidine PNP; (B) 120 nm Amidine PNP; (C) 20 nm COOH PNP; (D) 120 nm COOH PNP.

Additional experiments were conducted to explore the involvement of PNP-BLM interactions in amidine PNP aggregation. One hypothesis was that DOPC liposomes remaining in solution after forming the upper tBLM leaflet (concentration estimated to be  $<1.3~\mu\text{M}$ ) may have interacted with the amidine PNP, triggering aggregation. To test this hypothesis, amidine PNP were incubated with a wide range of DOPC liposome concentrations (10, 1, 0.1, 0.01, 0.001  $\mu\text{M}$ ), and the size distribution profiles were

measured over a 300 min period (Figure 3.7). Figure 3.7 (A and B) show that the 23 nm amidine PNP aggregated to a lesser degree when exposed to the DOPC liposomes than when exposed to a tBLM (Figure 3.5 (C)). In addition, there was no significant aggregation of 120 nm amidine PNP exposed to DOPC liposome (Figures 3.7 (C) and (D)).

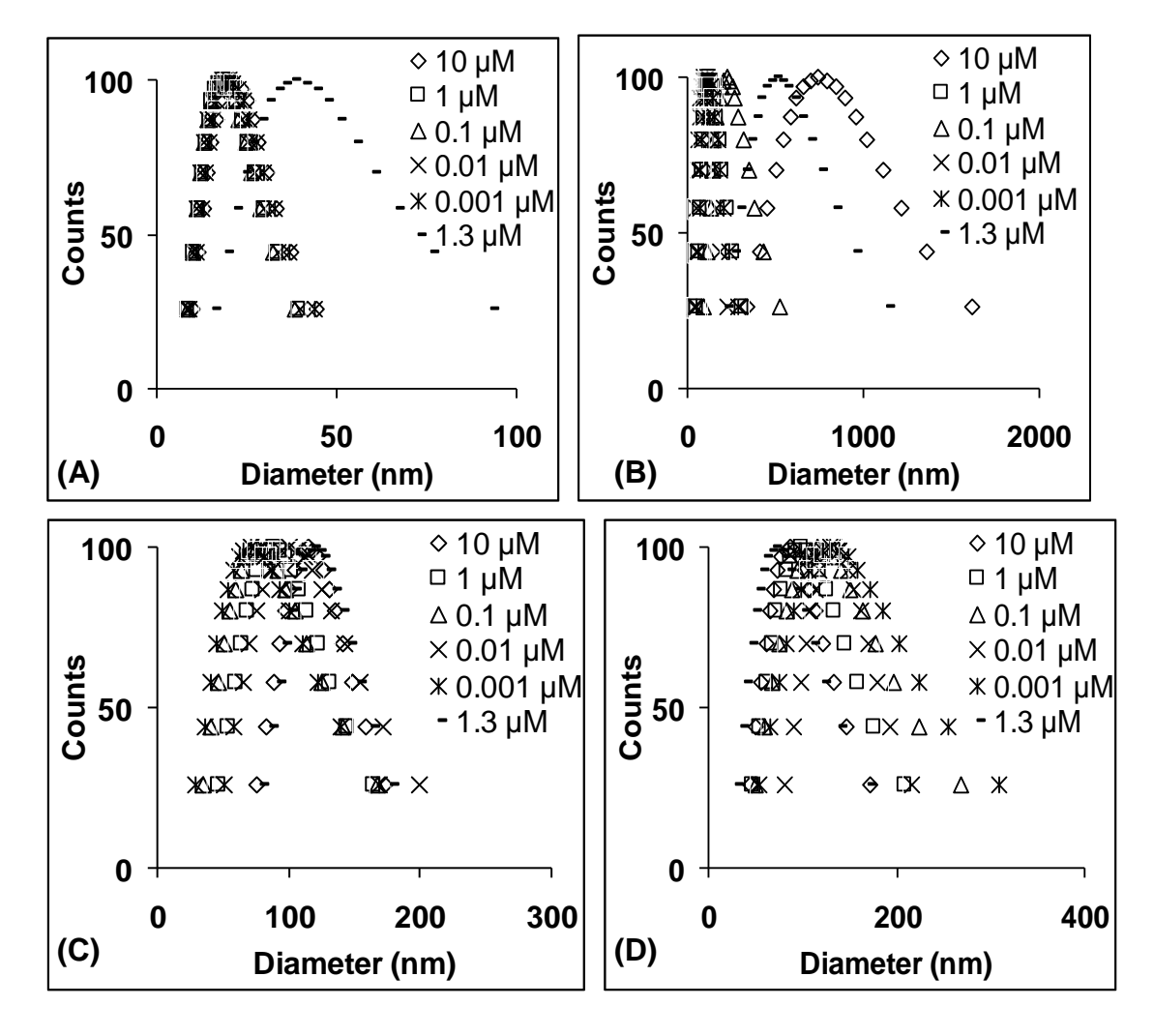


**Figure 3.7:** Size distribution of amidine PNP at different concentrations of DOPC liposome in 10 mM KCl, measured by DLS at 25 °C. (A): 23 nm Amidine PNP at 0 min; (B) 23 nm Amidine PNP at 300 min; (C): 120 nm Amidine PNP at 0 min and (D): 120 nm Amidine PNP at 300 min. Residue concentration of DOPC liposome was <1.3  $\mu$ M when tBLM was interacting with functionalized PNP while at all other concentrations of DOPC liposome, amidine PNP did not contact a tBLM.

### 3.4.6. DOPC analysis by LC/ESI/MS

A second hypothesis to explain amidine PNP aggregation following tBLM exposure was is that the PNP remove DOPC from the tBLM, and the adsorbed DOPC triggers PNP aggregation. To test this hypothesis, after the amidine PNP were exposed to the tBLM for 5 h, the PNP were recovered and extracted with isopropanol. The extract was then assayed for DOPC using UPLC/ESI/MS. As controls, similar extractions and assays were performed on (1) PNP-free solutions that had been contacted with a tBLM, (2) solutions containing 100 μg/mL COOH PNP that have been exposed to a DOPC tBLM, and (3) solutions containing an equivalent concentration of amidine PNP that had not been exposed to a tBLM. Figure 3.8 shows peak area of DOPC at m/z=786.6 for the different samples, including a DOPC standard dissolved in isopropanol. The DOPC peak had a retention time of 23.08±0.10 min. DOPC extracted from 120 nm and 23 nm amidine PNP after exposure to a tBLM were at least 10 and 50 times higher, respectively, than that the highest content of DOPC detected among the controls, confirming that the amidine PNP DOPC lipids did contain DOPC following 5 h exposure to the tBLM.

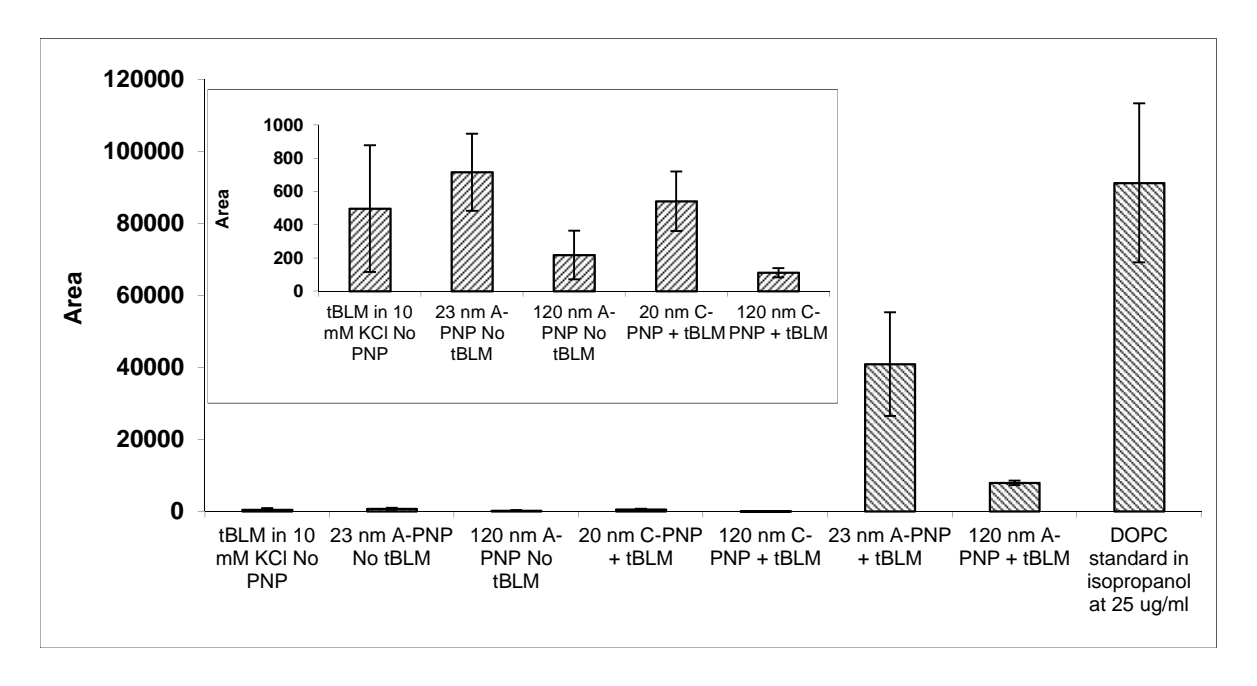


**Figure 3.8:** Peak area of DOPC at m/z=786.6 analyzed by UPLC-MS. DOPC lipids were extracted from functionalized PNP after exposure to tBLM and bare gold for 5 h as well as from the solution where PNP was not added in the presence of tBLM. A and C in the x axis labeled stand for amidine and COOH, respectively.

#### 3.5. Discussion

The goal of this study was to use EIS to characterize interactions between a DOPC tBLM and PNP having different sizes (ca. 20 and 100 nm) and functional groups (COOH and amidine). The hydrophobic core of an intact BLM is an excellent barrier to ion flow, resulting in high initial  $R_m$  values (on the order of 1 M cm2). The reduction in  $R_m$  following PNP exposure is likely due to PNP-induced defect (hole) formation and/or expansion. Formation and/or expansion of defects in supported BLM by dendrimers has been documented using atomic force microscopy [60, 107]. Increased ion transport through these defects would be manifested as a reduction in  $R_m$  values following PNP addition, while Cm remains roughly constant [36]. Similar trends are commonly observed

following incorporation of channel proteins [97] or electroactive molecules into a tBLM [57].

Figures 3.3 showed that the best-fit b values were significantly different between the two sizes of COOH PNP and also between the two sizes of amidine PNP. Moreover, the  $R_m$ % values were significantly different between the two sizes of COOH PNP. However, there was no significant difference in zeta potential between the two sizes of COOH PNP, and only a minor difference between the two sizes of amidine PNP. In addition, the PNP mass concentration was identical for all experiments (100  $\mu$ g/mL). These results indicate that the tBLM method can distinguish between PNP based on their size. The apparent size effect may be manifested indirectly, via the influence of PNP diameter on PNP surface area, PNP diffusion rate, and/or some other size-dependent influence. The importance of ENM size on biomembrane interactions has been reported previously for other types of ENM, including dendrimers [119]. The 20 nm COOH PNP triggered a more rapid decline in  $R_m$  than the 100 nm COOH PNP, consistent with other studies that reported higher trafficking or uptake rates of smaller PNP into biomembranes [80, 120].

Figures 3.3 also showed that the best-fit  $R_m$ % parameters were significantly different between the two functional groups for both the larger (ca. 100 nm) and smaller (ca. 20 nm) sizes. Moreover, the b values were significantly different between the functional groups for the larger PNP. The DLS-measured diameters of the 20 and 23 nm PNP were statistically identical, and those of the 100 and 120 nm PNP were only slightly different. These results indicate that the tBLM method can distinguish between PNP based on their functional group. For the functional groups studied, the effect of functional

group is likely manifested via surface charge. The zeta potentials differed dramatically between similarly sized COOH and amidine PNP (Table 3.3).

Clustering analysis applied to the best-fit b and  $R_m$ % values also demonstrated the tBLM method's ability to distinguish between PNP based on both size and functional group. The dendrogram (Figure 3.4) indicated that the results clustered first by size and then by functional group, suggesting that functional group was the more potent variable in influencing PNP-induced tBLM disruption.

All  $R_m$  vs. time profiles were reasonably described using the exponential decay model. Although this model uses three parameters, (b,  $R_i$ , and  $R_f$ ), combining  $R_i$  and  $R_f$  into a single parameter ( $R_m$ %) allowed the results to be satisfactorily clustered with only two parameter.

There was statistical difference of DOPC content associated with aggregated amidine PNP in both sizes (Figure 3.8), with the smaller amidine PNP absorbing more DOPC. This finding is consistent with aggregation for the 23 nm amidine PNP being much greater than for the 120 nm amidine PNP. While both liposomes and tBLM were able to trigger some degree of amidine ENM aggregation, tBLM exposure was far more potent in triggering coalescence than liposomes. This result may reflect differences in the fluidity, geometry or lower-leaflet composition of the unsupported BLM in the liposomes compared to the tethered BLM.

Nanoparticles can interact with BLM through a variety of mechanisms, some of which can result in nanoparticle-induced lipid removal from the BLM [36]. Because DOPC is nearly ubiquitous, and the detection limit of the LC/MS system is extremely low (around 10<sup>-16</sup> mol), harsh and complex cleaning procedures would have been

required to completely remove all DOPC from the glass tubes used to extract the DOPC from PNP samples [121]. As a result, even controls to which DOPC was not added showed traces of DOPC (Figure 3.8). However, the much larger amounts of DOPC found in amidine PNP samples that were exposed to the tBLM are consistent with our hypothesis that amidine PNP extract DOPC from the tBLM. Nanoparticle-induced extraction of phospholipids from lipid bilayers has been reported by others. Tu et al. presented both experimental and theoretical evidence that graphene nanosheets can extract phospholipid from lipid bilayers and become coated by the extracted phospholipid [122]. The lipid extraction was attributed to strong dispersion interactions between the graphene and lipids. Solvent-mediated forces that can dominate nanoparticle-BLM interactions at small distances, especially for biological colloidal systems [123], may also play a role.

Theoretical models have predicted that nanoparticles can entirely cross a BLM and/or become wrapped in BLM [124], depending on the balance of contact-adhesion energy and curvature energies [125-127]. Simulations have estimated the minimum nanoparticle size for such wrapping to be around 30 nm, which represents the transition state between partially lipid coated nanoparticles and free nanoparticles [78]. Thus, nanoparticle size would be expected to influence the reduction of R<sub>m</sub> following PNP exposure as was observed in Figures 3.3.

Even small amounts of PNP-induced phospholipid removal from the tBLM can explain the  $R_m$  reduction shown in Figure 3.2. The electrical resistivity of a BLM (about 1012 cm) is about ten orders of magnitude higher than that of the 10 mM KCl electrolyte solution (about 70 cm) [128]. As a result, the overall  $R_m$  of a high-

impedance tBLM can be exquisitely sensitive to small ENM-induced defects. Assuming a PNP-induced defect went through both the upper and lower leaflets, a defect area fraction of only  $1.8\times10^{-13}$  would cause a 50% decrease in the  $R_m$  value [22]. The amount of lipid that would need to be removed from the tBLMs used in this study to achieve this defect area fraction is less than the amount needed to fully coat a single 20 nm nanoparticle. Assuming the PNP removed lipid only from the upper leaflet, the entire upper leaflet would need to be removed to cause a 50% reduction in  $R_m$ . The fact that  $R_m$  reductions up to about 80% of the initial value were observed in this study suggests that lipid was removed from both the top and bottom leaflets.

A second mechanism by which nanoparticles may influence  $R_m$  values is by changing the local BLM packing density. Functionalized 20 nm PNP were shown to cause surface reconstruction of various phosphocholine BLMs in giant unilamellar vesicles [129]. Negatively charged COOH PNP induced local gelation in a DOPC BLM above the phase-transition temperature, and positively charged amidine PNP induced local fluidization in a 1,2-dipalmitoyl-sn-glycero-phosphocholine BLM below the phase-transition temperature [129]. In the present study, COOH PNP may have caused local DOPC gelation, but the effect of this surface reconstruction on  $R_m$  is unclear. Local PNP-induced compaction could increase the local  $R_m$ . However, unlike the giant unilamellar vesicles, which can shrink if gelation occurs [129], the tBLM has a fixed total surface area and inventory of lipids. Thus, BLM compaction in one location would cause BLM stretching in other areas, potentially creating or expanding defects, which could reduce  $R_m$ .

The finding that amidine PNP gave a smaller R<sub>m</sub>% than the similarly sized COOH PNP (Figure 3.3) was surprising, given the previous observations that (1) amidine PNP passed through primary rat alveolar epithelial cell monolayers 20-40 times faster than COOH PNP [80, 115], (2) negatively charged cell membranes adsorbed cationic nanoparticles more extensively than anionic ones [59], and (3) amidine PNP more aggressively induced pores in DOPC planar BLM than COOH PNP [116]. This result is attributed to the aggregation of amidine PNP into large flocs (Figures 3.6 (A) and (B)), which significantly depleted the effective PNP concentration in the solution.

The PNP's surface functional group was found to strongly influence the aggregation rate during tBLM exposure. This finding is consistent with our previous observation that bare silica nanoparticles exposed to a DOPC tBLM aggregated significantly (10-fold increase in effective diameter), while COOH-functionalized silica nanoparticles having a similar zeta potential did not [22]. In that study, control experiments provided strong evidence that the factor triggering aggregation of the bare silica nanoparticles was exposure to the tBLM. The different aggregation properties of the amidine and COOH PNP may be interpreted in terms of long-range charge interactions. The PNP's surface charge generates an electrostatic repulsive force that provides an energy barrier to PNP collision and aggregation. Electrolytes that shield the charge or compounds that adsorb onto the PNP's surface can reduce the repulsive force, thereby accelerating aggregation [130, 131]. Previous studies to characterize PNP aggregation under reaction-limited [132] and diffusion-limited [133] conditions showed that even trace quantities of surface-active impurities can significantly increase PNP aggregation rates. For example, low concentrations of hydrophobically modified ethyl(hydroxyethyl)cellulose polymer and sodium dodecyl sulfate triggered rapid aggregation of cationic PNP into macroscopic flocs similar to those shown in Figure 3.6 [134]. The authors proposed that the amphiphilic polymer adsorbed onto the PNP, creating high-energy hydrophobic patches on the PNP surface. Spontaneous bridging between such hydrophobic patches on adjacent PNP would be entropically driven. Highly ordered water clathrates form adjacent to hydrophobic patches in aqueous solution. Bridging of two hydrophobic patches would eliminate the clathrates, thereby increasing the system's entropy [135]. A similar mechanism is likely to occur in the PNP-tBLM system. Extraction of small quantities of DOPC from the tBLM would create hydrophobic monolayer patches on the PNPs' surfaces. Bridging of patches between adjacent nanoparticles would form PNP clusters, and then bridging between clusters would form the flocs seen in Figure 3.6.

The type of BLM system used (tBLM vs planar BLM) also affected the aggregation rate of amidine PNP during exposure to a DOPC BLM. The heavy aggregation observed for amidine PNP (Figure 3.6) was not observed when the same amidine PNPs were exposed to a DOPC planar BLM [116]. We attribute this difference to physical constraints the gold electrode places on PNP penetration into the tBLM. Amidine and COOH PNP have been shown to pass through cell membranes, reportedly by diffusion through the plasma membrane [80, 115]. In the process, the PNP are likely to become coated with a BLM, as has been described for other types of nanoparticles, including dendrimers [136]. BLM-coated PNP would be expected to be relatively stable against aggregation, as are BLM-coated silica nanoparticles (e.g., TRANSIL®) [137].

This conceptual model of how PNP interact differently with a tBLM than with a planar BLM is also consistent with trends in the electrochemical results. For the planar BLM, DOPC molecules removed by the PNP would be replaced from the Plateau-Gibbs border. The observed of transient current spikes separating extended periods of low background current [116] could result from a pore formed as a PNP penetrates into the planar BLM, followed by flow of lipids from the Plateau-Gibbs border to seal the pore and terminate the current spike. In contrast to the planar BLM, the tBLM's underlying gold electrode limits the PNP's penetration depth into the tBLM. Also, tethering of some lipids to the gold electrode limits the amount of lipid that can be extracted from lower leaflet and consequently the degree of R<sub>m</sub> reduction observed following PNP exposure. Consequently, amidine PNP would likely only become partially coated with phospholipid after contacting the tBLM. Monolayer lipid patches would be hydrophobic and facilitate the observed interparticle bridging and aggregation. In support of this model, significant lipid removal from supported BLM by cationic nanoparticles including dendrimers, poly-L-lysine, polyethylenimine, and diethylaminoethyl-dextran, has been reported [60, 106, 138]. Such lipid removal would generate patches of bare electrode or lipid monolayer whose impedance would be lower than the bilayer, resulting in the reductions in R<sub>m</sub> seen in Figure 3.2.

Based on this conceptual model, the amount of lipid removed from the tBLM, and hence the observed degree of reduction of R<sub>m</sub>, would be expected to depend on the nanoparticle's size. The maximum depth to which the PNP could penetrate into the tBLM is equal to the tBLM's depth (about 5 nm). However, the total surface area of the PNP's spherical cap in contact with the tBLM at maximum penetration depth, as well as the

fraction of the nanoparticle's surface area in contact with the tBLM, would vary with the nanoparticle's size, consistent with the tBLM method's observed ability to discern differences in PNP particle size.

Comparison of results from the tBLM and pBLM systems provides insight into the relative advantages, disadvantages, and areas of complementarity of the two methods. Both methods are based on a BLM having an area-normalized resistance on the order of 1 cm2. Because the planar BLM is unsupported, it is fragile and prone to rupture during several-hour experiments, whereas tBLM's tethered lower leaflet makes it more physically robust. Microscopic roughness of the gold electrode's surface causes slight defects in the tBLM, resulting in initial area-normalized R<sub>m</sub> values that are slightly less than those for planar BLM and prone to minor variations between replicates. In control experiments conducted without nanoparticle addition, the tBLM's R<sub>m</sub> was constant over a several-hour period with a random fluctuation level of 0.062 M cm2 at the 95% confidence interval [22]. The noise level of the planar BLM is about 1 pA. PNP interactions with a planar BLM induced pores, as evidenced by sudden increases in current that were at times one or more orders of magnitude greater than the background signal [116]. In contrast, PNP interactions with the tBLM reduced R<sub>m</sub> over a smaller range (about 80% of the initial value). The lower sensitivity for the tBLM method is due in part to differences in the measurement methods. The planar BLM method uses chronoamperometry, which measures increases in current against an initially low value, whereas the tBLM method uses EIS, which measures decreases in tBLM resistance against an initially large value. In addition, chemical tethering of the lower tBLM leaflet makes it difficult to form a sizable pore through both leaflets. Because of these inherent differences, direct quantitative comparison of results from the tBLM and the planar BLM methods is difficult.

However, application of both the tBLM and planar BLM methods to the same ENM (e.g., COOH and amidine PNP) and phospholipid (e.g., DOPC) provides complementary information that can help elucidate interaction mechanisms. The planar BLM provides sensitive, time-resolved information about single-pore events with a time constant on the milliseconds. For example, penetration of a nanoparticle through the planar BLM, followed by rapid resealing of the BLM is consistent with the frequently observed current spikes [116]. However, nanoparticle-induced lipid removal is difficult to discern with the planar BLM method, because the Gibbs-Plateau border quickly replaces the removed lipids, allowing the pore to close. In contrast, the fixed area and lipid inventory of the tBLM method does not allow lipid replacement, so ENM-induced extraction of lipids from the tBLM would permanently reduce R<sub>m</sub>. Thus, the tBLM system provides a global measure of the ENM's influence on the tBLM's R<sub>m</sub> that is integrated over time and area and has a time constant ranging from seconds to hours. The tBLM method is more robust than the planar BLM method. Some nanoparticles are particularly aggressive toward planar BLM, causing rapid rupture and then preventing the BLM from being reestablished. In addition, the equipment cost and technical difficulty of tBLM experiments is less for the tBLM system than for planar bilayer system. However, further experimental and modeling research is needed to map time-dependent changes in R<sub>m</sub> obtained using the tBLM method into a mechanistic understanding of ENMbiomembrane molecular interactions.

#### 3.6. Conclusions

This work demonstrates for the first time that the tBLM method can measure biomembrane disruption by PNP with sensitivity that can discriminate between PNP having the same functional groups but different size, and between PNP having the same size but different functional groups. Both PNP sizes tested (ca. 20 and 100 nm) and both functional groups (amidine and COOH) resulted in reductions in R<sub>m</sub> that could be described by a simple exponential model. Statistical analysis of two regression parameters from the exponential model (b and R<sub>m</sub>%) yielded a dendrogram that first clustered the triplicates for all test cases, then clustered PNP having the same but different sizes, and finally clustered the PNP having different functional groups. These results further establish the tBLM method as a sensitive and versatile tool to characterize ENM-biomembrane interactions. The simple and well-characterized tBLM interface can be easily customized by changing the lipid composition, adding additional biomolecules, etc., to test a broad range of hypothesis. The information-rich  $R_{\text{m}}$  vs. time profiles are likely to contain additional insight into fundamental mechanisms by which ENM interact with biomembranes that could be discerned through further studies and integration of mathematical models. The finding that amidine PNP aggregate in the presence of tBLM but not planar BLM or intact cell membranes suggests that the tBLM method provides complementary information to the other experimental platforms. The presence of DOPC lipids associated with amidine PNP aggregates after exposure to the tBLM is consistent with the hypothesis that amidine PNP capture lipids from the tBLM, and that the captured lipids trigger aggregation. The utility of the tBLM method to characterize ENMbiomembrane interactions, combined with its ability to be miniaturized and adapted with

MEMS systems, may lead to automated, high-throughput screening systems to identify ENM that are both safe and effective for desired applications.

### 4. INTEGRATION OF MINIATURIZED BIOSENSOR ARRAY WITH A MULTI-CHANNEL IMPEDANCE EXTRACTION CIRCUIT

#### 4.1. Abstract

Tethered bilayer lipid membrane (tBLM) methods are well suited for studying interactions between biomembranes and functional molecules including engineered nanomaterials (ENM), ion channel proteins, and ionophores (e.g., gramicidin). In this chapter, research was conducted to adapt tBLM methods to high-throughput and automatic operation mode. Miniaturized electrode arrays were used for fabricating nanostructured biosensors and for demonstrating the ability of multi-channel impedance extraction and digitization for measuring electrochemical impedance spectroscopy. The tBLM biointerface formed on miniaturized electrode arrays exhibited giga ohm electrical resistance and therefore high insulating property, as well as ion channel incorporation activity. The exposure of tBLM to carboxylate (COOH) functionalized multiwall carbon nanotubes decreased impedance of the tBLM.

#### 4.2. Introduction

Miniaturized, electrical biosensors hold great promise for minimizing size, cost, and power in vital applications such as point-of-care diagnostics, bio-toxin detection and bioprocess monitoring [139]. Electrode array based biosensors can be integrated onto CMOS chip circuitry integrated with a microfluidic assembly to automate fluid delivery, as shown schematically in Figure 4.1. Biosensors today often incorporate affinity-based interfaces such as nucleic acids, antibodies and antigens, and optical techniques are commonly employed to measure binding of fluorescent tags. Alternatively, sensors

utilizing electrochemical techniques have the advantages of direct transduction to electrical signals and reduced interference noise. Furthermore, because electrochemical instrumentation can readily be implemented within CMOS chips, electrochemical biosensors offer an ideal basis for miniaturization into a microsystem array platform [140].

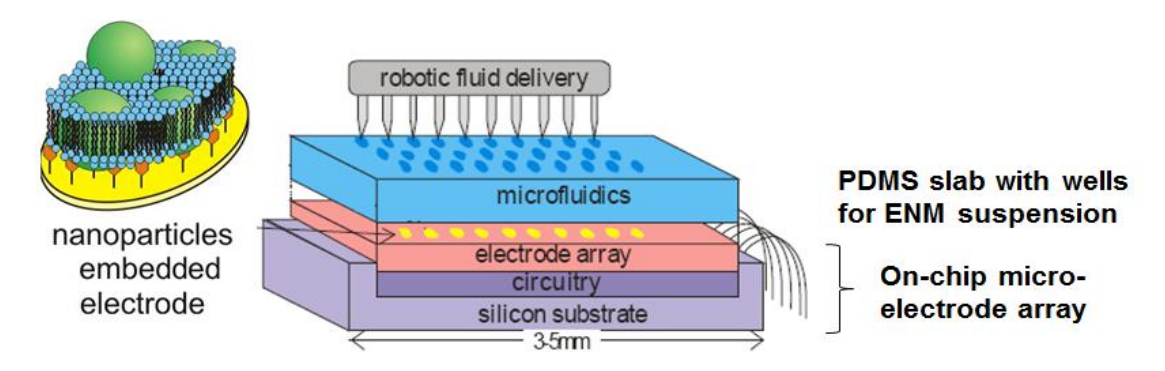


**Figure 4.1:** Electrochemical biosensor array microsystem concept with fluid delivery to an electrode array on the top of a silicon integrated circuit.

Electrochemical microsystems have been formed by immobilizing affinity-based bio-recognition interfaces onto CMOS electrodes [141]. However, affinity-based interfaces do not permit continuous operation because the analytes do not disassociate easily from the probe. Alternatively, enzyme and membrane protein interfaces are capable of continuous use and provide label-free monitoring with electrochemical techniques. Enzyme interfaces maintain continuous catalytic activity for amperometric monitoring when immobilized on an electrode by physical trapping or covalent binding [142]. Many membrane proteins can be continuously monitored using a variety of electrochemical techniques and can be immobilized on electrodes using synthetic BLM serving as biomimetic interfaces to circumvent denaturing [143]. The development of a

CMOS-based electrochemical microsystem platform that combines membrane-protein biointerfaces would enable a new breed of biosensor arrays that are valuable for biological research and medical applications. Furthermore, such a platform would open new pathways for biology-to-silicon communication with vast opportunities for future applications [144, 145].

Tethered BLM interfaces can be characterized by EIS using a commercial potentiostat. Impedance spectra can be recorded by sweeping the frequency of a small sinusoidal voltage stimulus and measuring the resulting current. The stimulus frequencies vary depending on the interface measured, but are generally in mHz to kHz range for many thin-film biomaterials.

The objective of this work was to demonstrate the ability to build tBLM interfaces on miniaturized electrode array and to test functionality of a fully integrated multichannel impedance extraction circuit (MIED) that could both generate ac stimulus signals over a broad frequency range and also measure and digitize the real and imaginary components of the impedance response of tBLM interaction with nanoparticles. The tBLM method was also adapted to gramicidin ion channel characterization using an electrode array based biosensor. A model electrochemical sensor array platform was implemented by incorporating gramicidin ion channel-based alkali sensor. Because alkali ions, including sodium and potassium, are reported to have an effect on blood pressure [146, 147], this model sensor array could aid in the study and treatment of cardiovascular disorders, diabetes and related complications. The miniaturized electrode and MIED were fabricated in collaboration with the laboratory of Dr. Andrew Mason from the MSU Department of Electrical and Computing Engineering.

This research on microsystem integration fills the gap between heterogeneous protein-based biosensors and CMOS electrochemical instrumentation circuitry by identifying suitable processes for post-CMOS electrode fabrication, bio-interface formation and sensor interrogation. By replacing the protein bio-recognition elements, this model platform can be expanded to tackle a wide range of detection challenges in fundamental biomedical research, medical diagnostics and drug discovery.

#### 4.3. Materials and Methods

#### 4.3.1. Fabrication of miniaturized electrode

The electrode was fabricated on the silicon substrate with thermal oxides using lift-off process. Before fabrication, a photomask was designed for 1 mm diameter electrode. Negative AZ5214 photoresist was spin coated on the cleaned substrate. After 1 minute soft bake at 95°C on hotplate and 0.7s UV exposure with the photomask, the substrate was then baked for 30 s at 110°C. Metal layers (5 nm titanium and 100 nm gold) were then deposited on the substrate using physical vapor deposition. Then the substrate was immersed in acetone overnight to lift-off the undesired titanium and gold areas. The 1 mm diameter gold electrode was then finally made after rinsing the substrate with acetone, isopropanol and DI water.

# 4.3.2. Design of fully integrated muti-channel impedance extraction circuit chip

A fully integrated MIED chip including a digitally programmable signal generator (SG) and multiple channels of a compact, high-sensitivity impedance-to-digital converter (IDC) [148] was fabricated in 0.5 µm complementary metal-oxide-semiconductor

(CMOS) and consumed 355  $\mu$ W at 3.3 V. Tailored for BLM characterization, the signal generator produced sinusoidal waves from 1 Hz to 10 kHz. To suit a variety of applications, the impedance extraction circuit provided a programmable current measurement range from 100 pA to 100 nA with a measured resolution of ~100 fA. The circuit occupied only 0.045 mm² per measurement channel and was compact enough to include nearly 100 channels and the signal generator on 3 × 3mm die.

## 4.3.3. Incorporation of gramicidin protein into tBLM biosensor array platform

An alkali sensor can be formed by embedding gramicidin, a dimeric membrane protein that selectively transports alkali metal ions, into the tBLM. The resulting interface will ensure that only alkali ions such as sodium and potassium pass through the BLM. The concentration of alkali analyte in the test solution will reflect proportionally in the membrane electrical parameter. The tBLM formation on gold electrode array followed the same protocol described in Section 2.3.5. Gramicidin insertion into the tBLM was accomplished by adding its ethanolic stock solution to give desired gramicidin concentration of 1  $\mu$ M in the KCl electrolyte solution. The concentration of KCl electrolyte ranged from 2 mM to 150 mM.

### 4.3.4. COOH MWNT interaction with tBLM biosensor array platform

The DPPTE/DOPC tBLM biosensor was exposed to 200 µg/mL COOH MWNT by adding COOH MWNT to the electrolyte solution to achieve the above concentration. Then, EIS was performed over the frequency range from 0.01 Hz to 100 Hz in a two-electrode setup with 0 V DC and 5 mV AC as the perturbation, relative to Ag/AgCl

reference electrode. The MIED chip automatically recorded impedance data and converted binary output into real and imaginary parts of the impedance.

#### 4.4. Results and Discussion

### 4.4.1. Electrochemical characterization of gramicidin ion channel incorporated biosensor performance

After tBLM formation, gramicidin ion channels were incorporated in the tBLM by maintaining protein in the electrolyte solution. The incorporation continued for one hour before testing. Since gramicidin can transport both potassium and sodium ions almost equally, potassium was chosen to characterize this alkali sensor. The impedance spectrum shown in Figure 4.2 was measured in the presence of KCl up to 150 mM, which covers the typical potassium concentration in blood (3.5 mM to 5.2 mM), urine (25 mM to 125 mM) and the typical blood sodium concentration (136 mM to 145 mM). In the  $R_{\rm m}$ dominated frequency range shown in the Figure 4.2 inset, the magnitude of impedance decreased as KCl concentration increased. One step further, the R<sub>m</sub> was extracted from Figure 4.2 impedance data using Z-View and plotted versus KCl concentration, shown in Figure 4.3. The inset plot of Figure 4.3 indicates the high linearity of R<sub>m</sub> in the blood potassium concentration range, where a K<sup>+</sup> sensitivity of -69.36 k /mM was obtained. To determine the limit of detection (LOD), multiple control measurements were performed in a buffer solution without any ions. The standard deviation of R<sub>m</sub> was calculated to be 48.41 k (n=3), and the LOD was calculated as three times the standard deviation. Using the absolute value of sensitivity, LOD in the range of 2.0 mM to 5.5 mM is 2.12 mM.

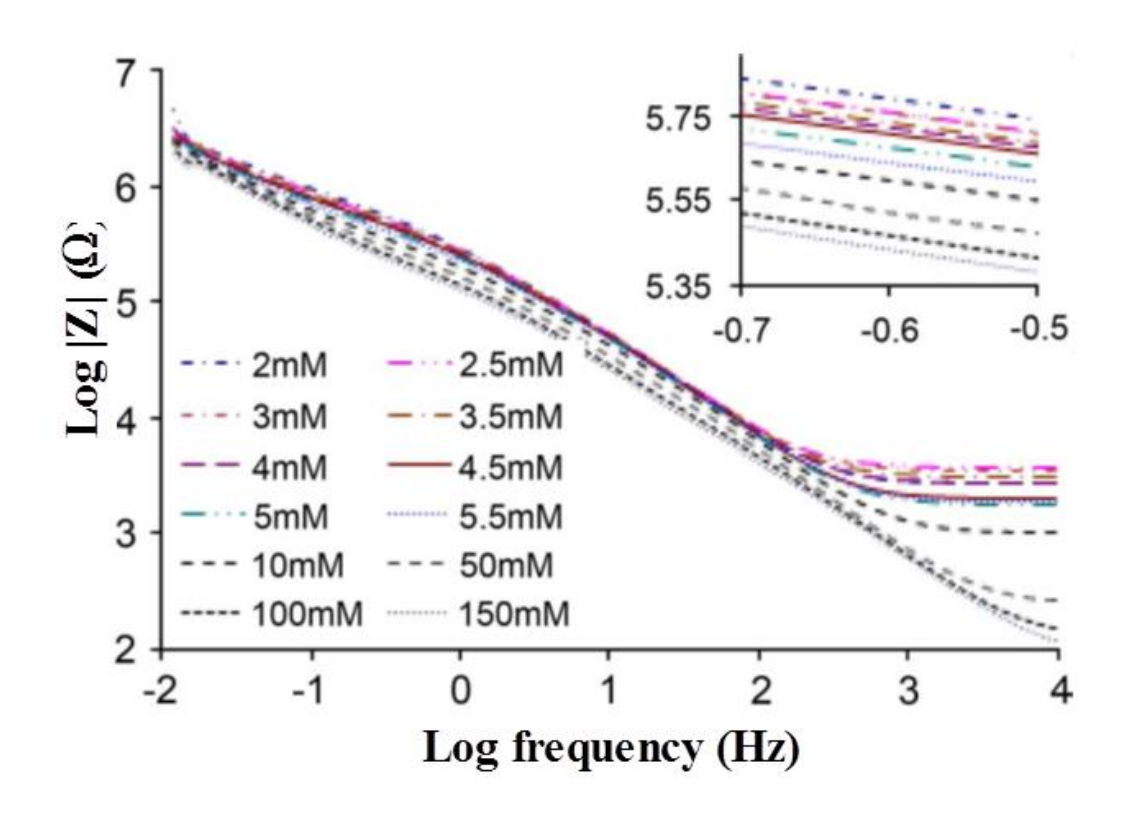


**Figure 4.2:** Impedance spectrum of gramicidin embedded tBLM in presence of KCl. Inset is a magnified plot of the  $R_m$ -dominate frequency range.

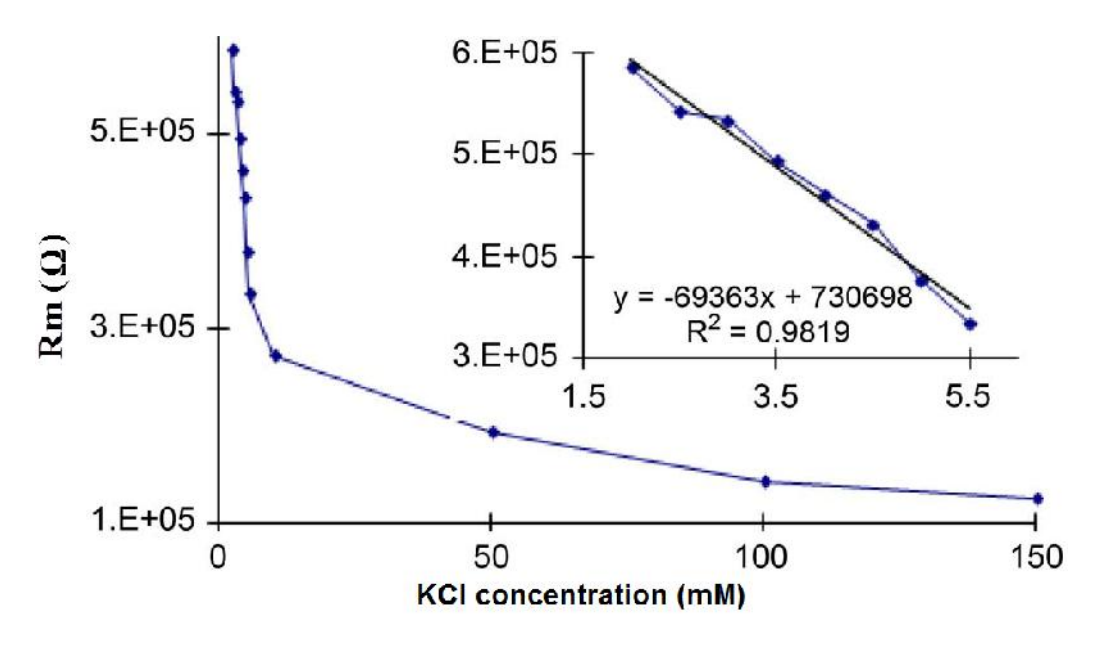


**Figure 4.3:** Membrane resistance  $R_m$  versus KCl concentration. Inset is magnified plot in concentration range of blood potassium.

The performance of the tBLM alkali sensor in measuring potassium ion concentration was summarized in Table 4.1 and compared with a reported potassium sensor [149, 150]. This model membrane protein interface demonstrates the potential of the protein-based electrochemical biosensor array platform introduced in this work. The tBLM sensor can be easily adapted to measure the activity of several other membrane transport proteins, ionophores and nanomaterials by embedding different ion channel and pore-forming proteins into the tBLM interface using similar protocols.

**Table 4.1:** Comparison of BLM potassium sensors

	BLM-	K <sup>+</sup> Range (mM)	Sensitivity	LOD (mM)
	ion channel			
This work	tBLM-Gramicidin	2 to 150	-69.36 k /mM	2.12
[150]	sBLM-Valinomycin	2.5 to 130	N/A	N/A

# 4.4.2. Electrochemical characterization of tBLM-nanoparticle interaction by commercial potentiostat and MIED

EIS was used to characterize the interaction between DPPTE/DOPC tBLM formed on miniaturized electrode and 200 μg/mL COOH functionalized multiwall carbon nanotubes (MWNT) over the frequency range from 0.01 Hz to 100 Hz in a two-electrode setup. Figure 4.4 shows that Bode plots of impedance spectra measured by potentiostat fit well with those measured by MIED chip. Each data point taken by MIED chip was averaged by repeating measurement five times at frequencies below 1 Hz while ten times at frequencies above 1 Hz, in order to reduce measurement error. The impedance magnitude of the tBLM reached up to 10 M , suggesting a highly insulating tBLM formed on 1 mm gold electrode. To investigate the interaction of tBLM with carboxylate

group modified MWNT, impedance was recorded immediately after addition of 200 µg/mL MWNT. The impedance spectrum measured in the presence of COOH MWNT using MIED chip well matches that measured using commercial potentiostat, indicating that MIED chip is able to tailor electrochemical impedance characterization to tBLM biosensor array. This is consistent with the theoretical mathematical design of the impedance readout chip [151] and the previous work relating micro-fabrication integrated biomimetic interface development [148].

- tBLM impedance magnitude measured by MIED chip
- -tBLM impedance magnitude measured by commercial potentiostat
- \* impedance magnitude of tBLM interaction with FMWNT measured by MIED chip
- —impedance phase of tBLM interaction with FMWNT measured by commercial potentiostat
- tBLM impedance phase measured by MIED chip
- ---tBLM impedance phase measured by commercial potentiostat
- impedance magnitude of tBLM interaction with FMWNT measured by MIED chip
- —impedance phase of tBLM interaction with FMWNT measured by commercial potentiostat

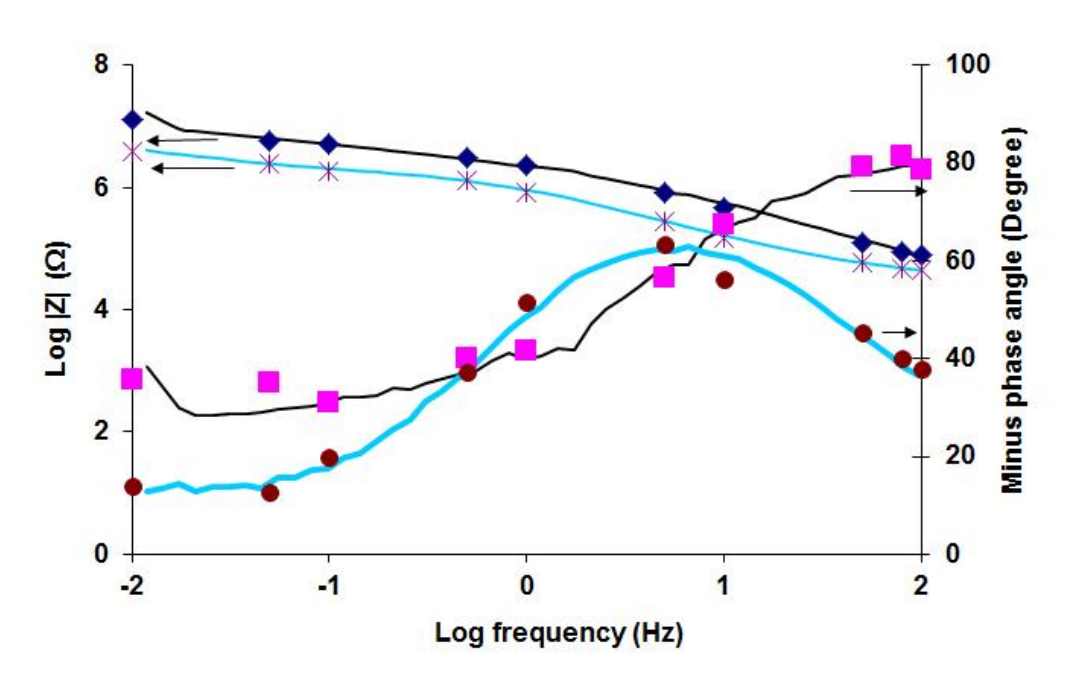


**Figure 4.4:** EIS spectra taken prior to and after addition of 200 μg/mL MWNT to tBLM formed on micro-electrode.

When tBLM interacted with MWNT, the instant impedance drop and phase angle peak at approximate 10 Hz instead of phase dip over the frequency range indicated the insulating barrier of tBLM becoming more capacitive and less resistive when exposed to MWNT, allowing enhanced ions transport across tBLM. Also, in our study of MWNT interaction with DOPC pBLM, MWNT was found to induce high level conductance which lasted up to tens of seconds, implying transient pores enabling ions to pass through lipid bilayers. Thus, the impedance decrease after addition of MWNT confirmed that MWNT could enhance ion transport across a lipid bilayer. This finding is consistent with molecular dynamics simulation showing that insertion of carbon nanotubes enhanced diffusion coefficient of ion transport across the dimyristoylphosphatidylcholine lipid bilayer by 35% [152]. Other toxicological effects induced by carbon nanotubes include membrane structure reorientation, alteration of lipid molecule packing, and/or loss of membrane fluidity [152]. Our results confirm that nanoparticle exposure to biomembranes can modify membrane properties.

#### 4.5. Conclusions

This work introduced a set of technologies for assembly of heterogeneous protein biosensors within a microsystem platform. A scalable, CMOS chip compatible electrode array was microfabricated to demonstrate its capability to accommodate membrane protein biosensor interfaces. A self-assembled biomimetic membrane was formed on the electrode array, followed by insertion of gramicidin, an ion channel protein, and impedance spectroscopy verified the detection sensitivity of potassium ions. The MIED instrumentation system on chip is tailored to BLM-based biointerfaces but provides the sensitivity and programmability to serve a range of impedance measurement applications.

Here, we demonstrated the use of the MIED chip for electrochemical impedance measurement of tBLM interaction with nanoparticles. So MIED chip is suitable for EIS measurements of biointerfaces as well as its functionality on a miniaturized electrode. Moreover, the electrode array platform is a milestone toward integrating protein-based electrochemical biosensor arrays and microelectronic instrumentation into highly functional microsystems.

### 5. DEVELOPMENT OF NANOPORE pBLM ON SILICON NITRIDE FOR INVESTIGATING ENM-BLM INTERACTIONS

#### 5.1. Abstract

Electrophysiological signatures of a bilayer lipid membrane (BLM) are influenced by both the BLM's lipid composition and the engineered nanomaterials (ENM) properties. Electrophysiological methods are well suited for studying single channel activity induced by ENM for they have temporal kHz resolution. This chapter reported a highly insulating biomimetic interface of planar BLM (pBLM) with giga ohm resistance on nanopore drilled through silicon nitride window grid by focused ion beam. Electrochemical impedance spectroscopy and electrophysiological techniques were used to characterize the functionality of nanopore pBLM. The pore-forming peptide gramicidin was used to validate the system's ability to measure pore formation in pBLM. ENM such as polyethylene glycol (PEG) functionalized silica core nanoparticles and carboxylate (COOH) functionalized multi-wall carbon nanotubes (MWNT) induced current spikes or extended integral conductance when interacting with nanopore pBLM, indicating transient hole formation on nanopore pBLM. Electrophysiological methods are capable of measuring ENM tendency to create pores in pBLM. Characteristic conductance induced by charged carbon nanotubes was 20 times higher than that triggered by PEG silica. The results predicted that charged carbon nanotubes were more aggressive in pore forming activity against nanopore pBLM, compared to silica nanoparticles.

#### 5.2. Introduction

Model BLM have previously been shown to exhibit mechanical and electrical properties similar to those of cell membranes [37] and thus offer outstanding potential for systematically probing the role of specific membrane properties (lipid composition, charge, fluidity, etc.) on cell membrane interactions with ENM.

Planar BLM represents the first generation of biomimetic model of a biomembrane. A pBLM that mimic biomemembranes are extensively used to study molecular phenomena involving cell membranes. The aperture diameter for pBLM formation typically varies from 100 nm to hundreds of micrometers, and the materials of test compartment are usually dielectrics such as glass, Teflon and silicon nitride [36]. Usually, a pBLM is formed by painting or brushing a solution containing phospholipids across an aperture separating two aqueous solutions [153]. Properties of pBLM or pBLM modified by different types of proteins can be readily characterized electrically. The chronoamperometric traces monitored by electrophysiological technique show detailed electrochemical signatures [46], which provide fundamental insight into molecule-biomembrane interactions, allowing pBLM associated with electrophysiology methods to be used to test ENM toxicity.

The high temporal resolution, on the order of milliseconds, and sensitivity offered by the pBLM method enable to characterize ENM-BLM interactions by analyzing current vs. time patterns in the electrical signatures following ENM exposure. One important hypothesis of this work is that ENM properties influence its interactions with pBLM. Especially, when the size of a pBLM falls in the nanometer range, only a few nanoparticles are allowed to access to the lipid bilayer interface. Therefore, the objective of the work was to fabricate a nanopore aperture across silicon nitride substrate via

focused ion beam lithography, to use electrophysiological methods to measure ENM (PEG terminated silica nanoparticles and COOH functionalized MWNT) tendency to create pores in nanopore pBLM.

#### 5.3. Materials and Method

#### 5.3.1. Materials

The phospholipids 1, 2-diphytanoyl-sn-glycero-3-phosphocholine (DPhPC), DOPC, 1-palmitoyl-2-oleoyl-sn-glycero-3-phosphocholine (POPC) and 1-palmitoyl-2-oleoyl-sn-glycero-3-phosphoethanolamine (POPE) were purchased from Avanti Polar Lipids Inc. (Alabaster, AL). All other chemicals, such as gramicidin D, chloroform, decane, ethanol, potassium chloride, and, 4-(2-hydroxyethyl)-1-piperazineethanesulfonic acid (HEPES) were purchased from Sigma Aldrich (St. Louis, MO).

# 5.3.2. Fabrication of nanopore on silicon nitride membrane window grids by focused ion beam (FIB)

Silicon nitride ( $Si_3N_4$ ) substrates (200 µm thick frame, 100 nm thick window, 1 mm  $\times$  1 mm window size) were purchased from SPI Supplies / Structure Probe, Inc. (West Chester, PA). A 1 nm thick layer of gold was sputter coated on the front side of the silicon nitride membrane window to avoid charge accumulation [154] during ion beam lithography using a Carl Zeiss Auriga Cross Beam FIB-SEM (Carl Zeiss NTS, LLC., Peabody, MA) with FIB probe at 30 kV and 50 pA. A nanopore having an average diameter of 760 nm on silicon nitride window (Figure 5.1), was imaged by scanning electron microscope (SEM).

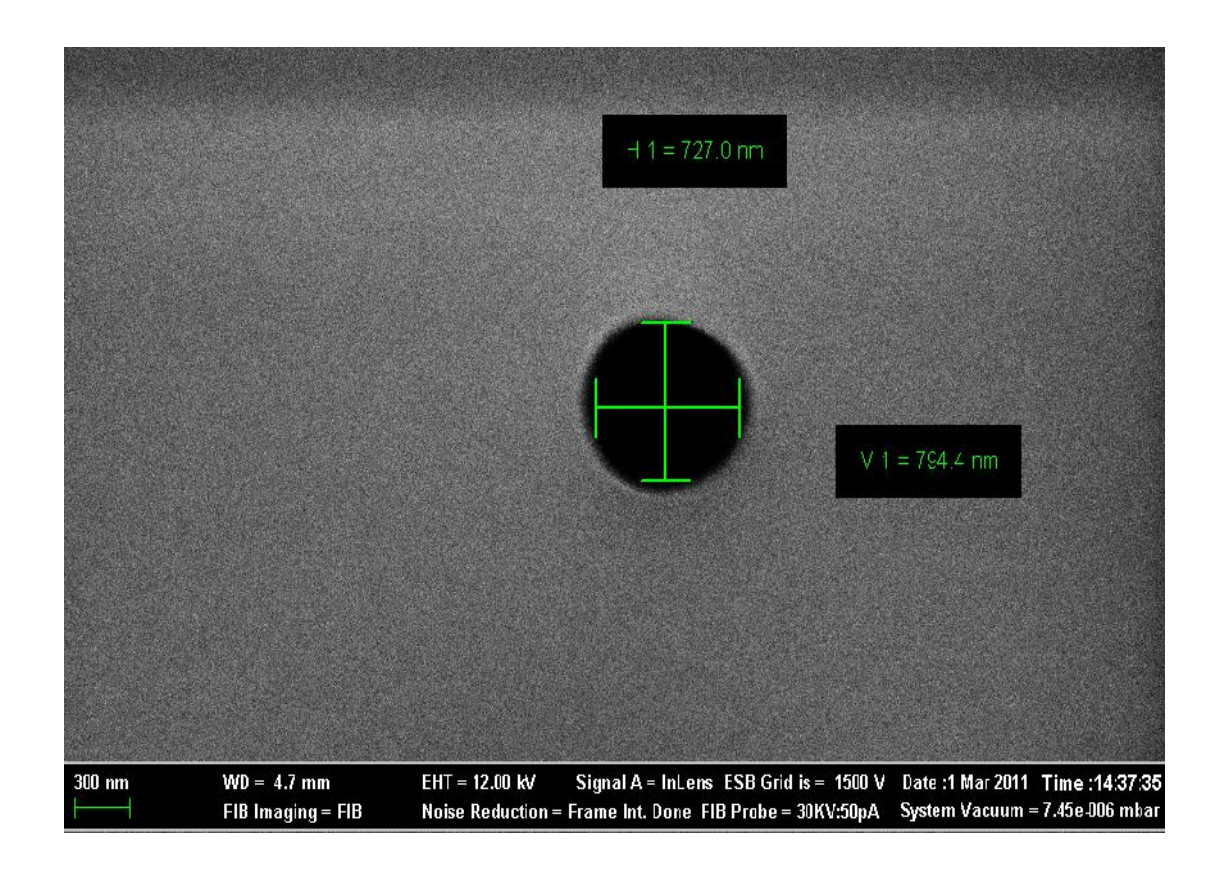


**Figure 5.1:** SEM image of nanopore on  $Si_3N_4$  window. The horizontal (H1) and vertical (V1) diameters are 727.0 nm and 794.4 nm, respectively.

#### 5.3.3. Formation of pBLM across nanopore on silicon nitride

The front side of the Si<sub>3</sub>N<sub>4</sub> window was pretreated with 10 mg/mL 1, 2-diphytanoyl-sn-glycero-3-phosphocholine (DPhPC) in decane and then dried. It is the net attractive interaction between phospholipids and underlying gold substrate that leads to the adhesion of phospholipids to the hydrophobic interface. These interactions consisting van der Waals forces, electrostatic interactions, entropic repulsion and hydration repulsion are in competition. The ultimate interaction mode is dependent on the dominant interaction force [155]. A DPhPC pBLM was then formed across nanopore in 20 mM KCl and 20 mM HEPES buffer by the Muller – Montal (M-M) method [38]. Briefly, buffer solution was slowly injected into the two compartments until the aqueous solution

level was close to the position of nanopore. Then, 10 µL of DPhPC was added to the two compartments followed by raising the buffer level via adding buffer solution to the aqueous solution phase gradually and slowly. A schematic diagram of the experimental setup for electrophysiological measurement of transient current across the nanopore pBLM is shown in Figure 1.1. Each Ag/AgCl reference electrode was immersed in buffer solution in a compartment separated by nanopore pBLM.

#### **5.3.4. Instrumentation**

EIS was performed over in a frequency range between 0.01 Hz and 10,000 Hz at 0 dc bias and an ac perturbation amplitude of 5 mV using a CHI660B electrochemical workstation (CH Instruments Inc., Austin, TX). An equivalent circuit [25] was employed to fit the impedance spectra and to simulate membrane resistance by Zview software (Scribner Associates, Southern Pines, NC). Reference and counter electrodes were Ag/AgCl electrode and platinum wire, respectively.

Current traces were recorded by bilayer workstation equipped with a bilayer clamp amplifier (Warner Instruments LLC., Hamden, CT). DC potential was applied to the *cis* compartment while the *trans* compartment was held at virtual ground. Currents were filtered at 10 kHz by a low pass 8-pole Bessel filter and data was digitized at 1 kHz using pClamp10 software (Molecular Devices Corporation, Sunnyvale, CA). Gramicidin was added to buffer solution to reach a concentration of 20 nM and then DC current was recorded at +100 mV. Similarly, PEG functionalized silica core nanoparticles (300 µg/mL) and COOH functionalized MWNT (300 µg/mL) were tested with nanopore pBLM composed of a mixture POPC and POPE, and DOPC, respectively. The current

across nanopore pBLM in presence of silica core nanoparticles and COOH functionalized MWNT was recorded at applied DC potential of -80 mV and +50 mV, respectively.

#### 5.4. Results and Discussion

#### 5.4.1. EIS and electrophysiological characterization of nanopore pBLM

Figure 5.2 shows Bode plots prior to and after pBLM deposition on silicon nitride nanopore. A dramatic increase of impedance magnitude at low frequencies and a plateau region of the phase angle from 1 Hz to 10,000 Hz are consistent with pBLM formation spanning nanoscale apertures [25, 156]. Pore resistance values extracted were 4.2 G and 0.2 M for nanopore pBLM and nanopore only, respectively. Giga ohm resistance for the nanopore pBLM is consistent with a highly insulating pBLM across the 760 nm aperture.

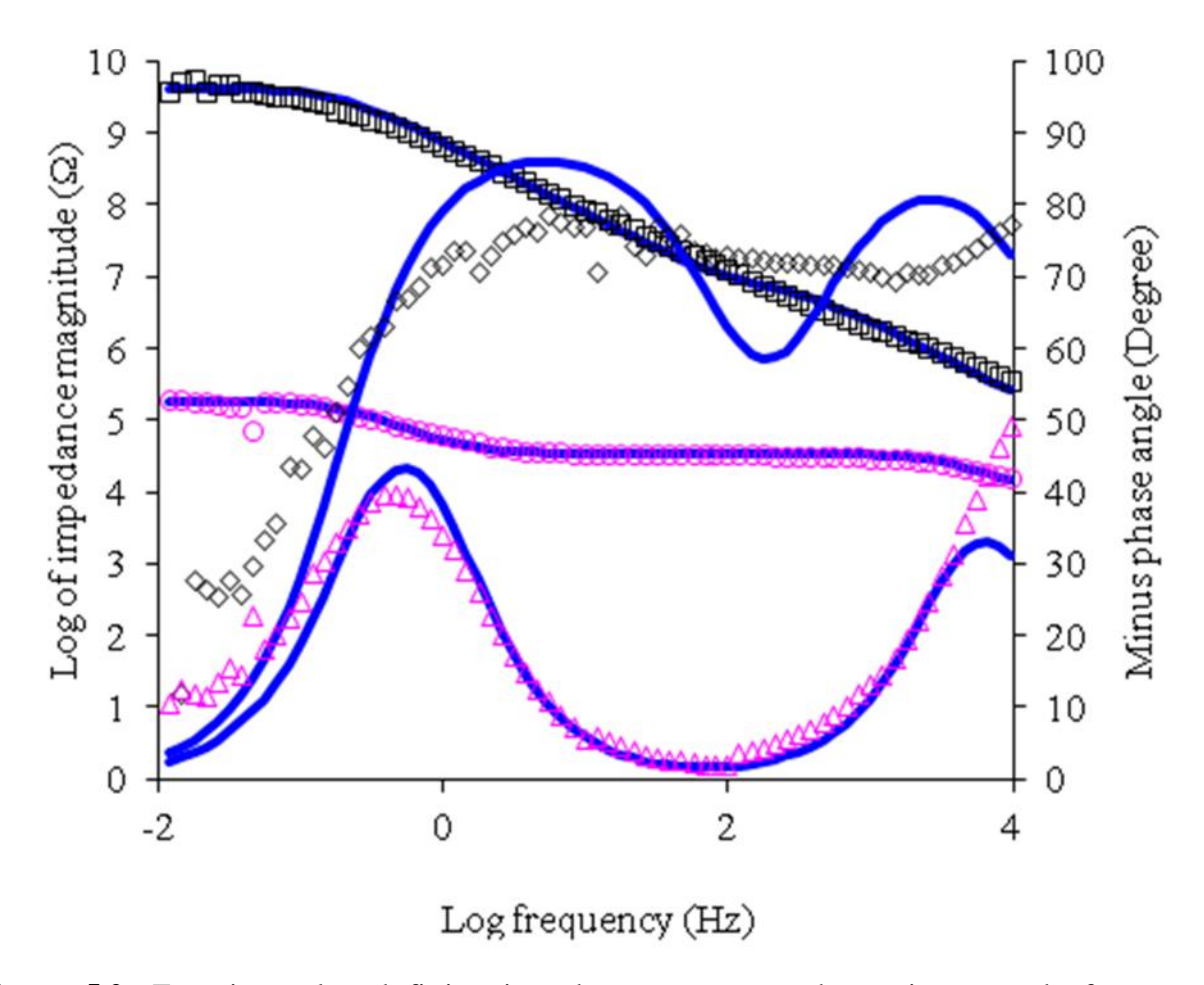


**Figure 5.2:** Experimental and fitting impedance spectrum taken prior to and after nanopore pBLM formation on silicon nitride window. Log of impedance magnitude: squares and circles for nanopore pBLM and nanopore, respectively; Minus phase angle: diamonds and triangles for nanopore pBLM and nanopore, respectively. All blue curves are impedance data fitted by Zview.

The channel-forming peptide gramicidin was used to further investigate the functionality of nanopore pBLM. Gramicidin peptides partition into both leaflets of the BLM. Alignment of peptides in the upper and lower leaflet creates an ion channel through the BLM that is selective for monovalent cations. Single-channel conductance following addition of 20 nM gramicidin was recorded at +100 mV. Single current spikes about 2.5 pA above baseline that lasted up to several seconds were shown in Figure 5.3. The well-defined feature of single channel current was observed and the average

conductance level was calculated to be 20 pS, both of which are in agreement with the single channel conductance of gramicidin reported using pBLM model [17, 157]. Formation of single gramicidin ion channels having the expected properties, coupled with the EIS results, suggest that the Si<sub>3</sub>N<sub>4</sub> nanopore pBLM platform is suitable for BLM-molecule interaction studies.

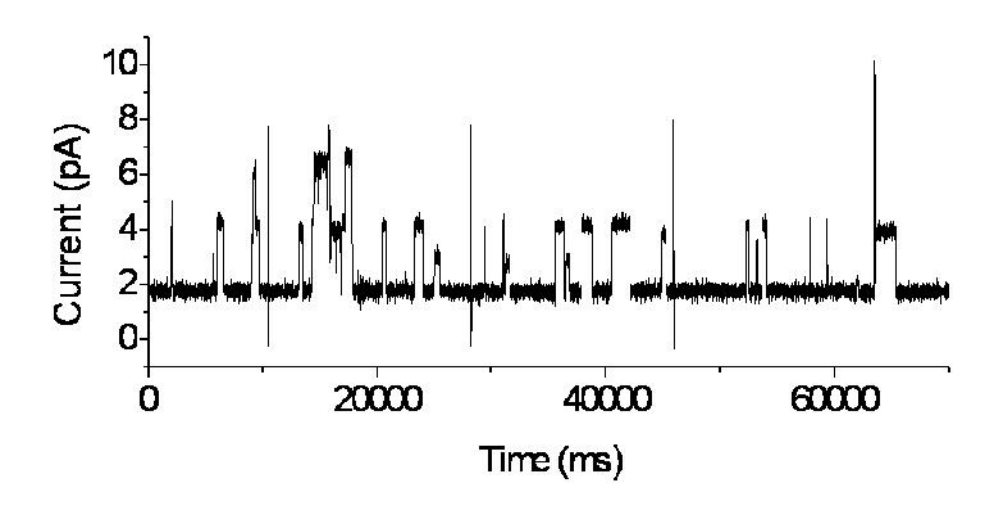
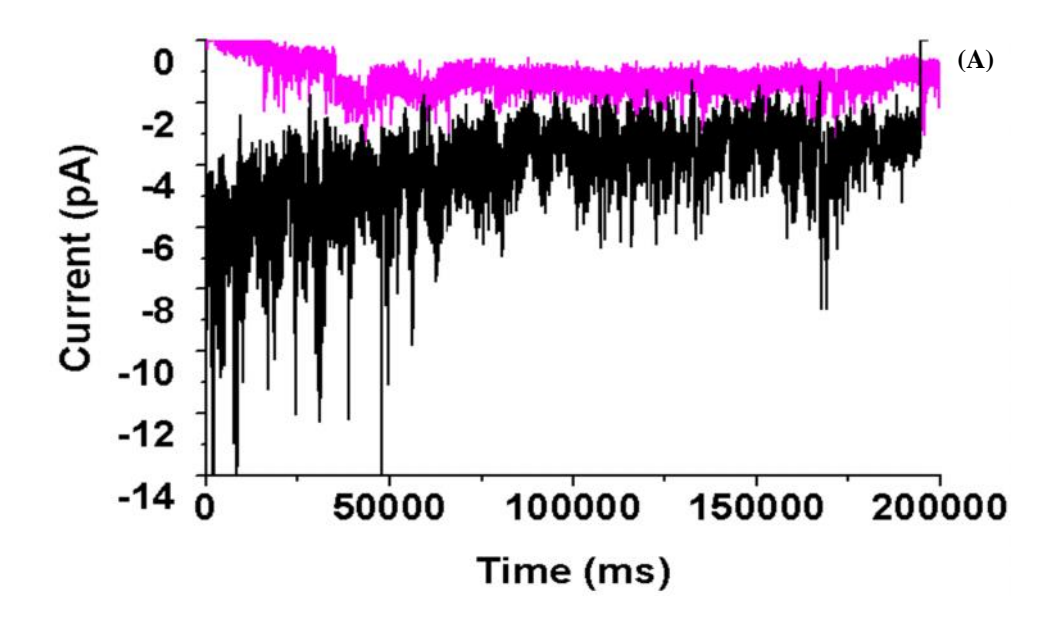


**Figure 5.3:** Trace of gramicidin (20 nM in ethanol) channel incorporated in nanopore pBLM in 20 mM KCl and 20 mM HEPES.

#### 5.4.2. Nanopore pBLM interaction with nanoparticles

The activity of PEG functionalized silica core nanoparticles (37 nm in diameter) and COOH functionalized MWNT (91 nm in diameter) were tested with nanopore pBLM in 20 mM KCl and 20 mM HEPES buffer. The current-time profile shown in Figure 5.4 (A) indicates that PEG functionalized silica tended to induce current spikes at -80 mV when interacting with pBLM composed of POPC and POPE, compared to control current profile. However, MWCT tended to cause much higher conductance in DOPC pBLM in Figure 5.5 (A). Current traces were recorded at +50 mV and -80 mV voltages applied to

nanopore pBLM and then the most abundant conductance was averaged from three independent experiments.



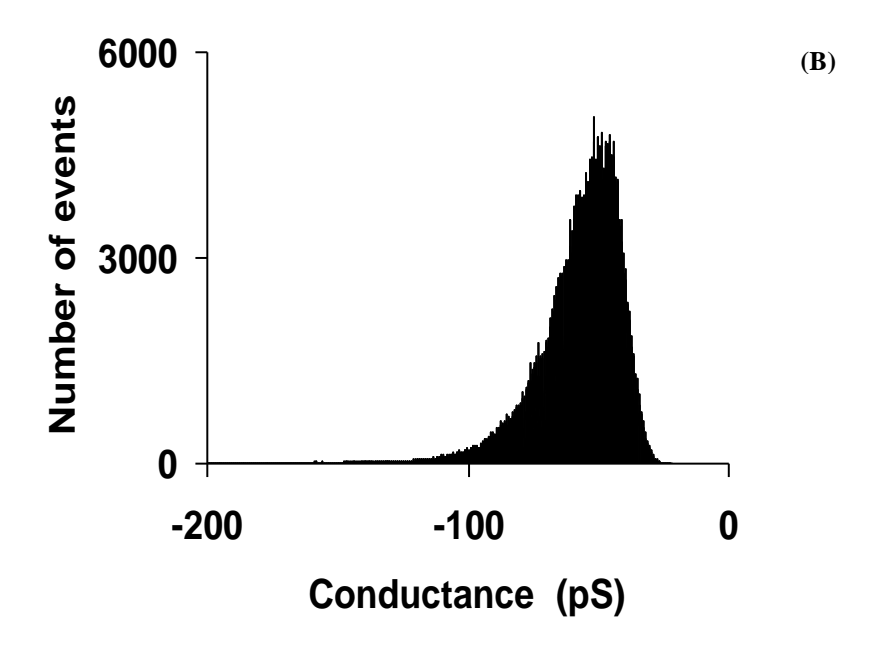


**Figure 5.4:** (A) Current vs time profile of pBLM composed of lipid mixture (POPC:POPE=3:1) without (in pink) and with (in black) 300  $\mu$ g/mL PEG terminated silica NPs in 20 mM KCl and 20 mM HEPES at -80 mV, respectively. (B) Corresponding histogram for (A).

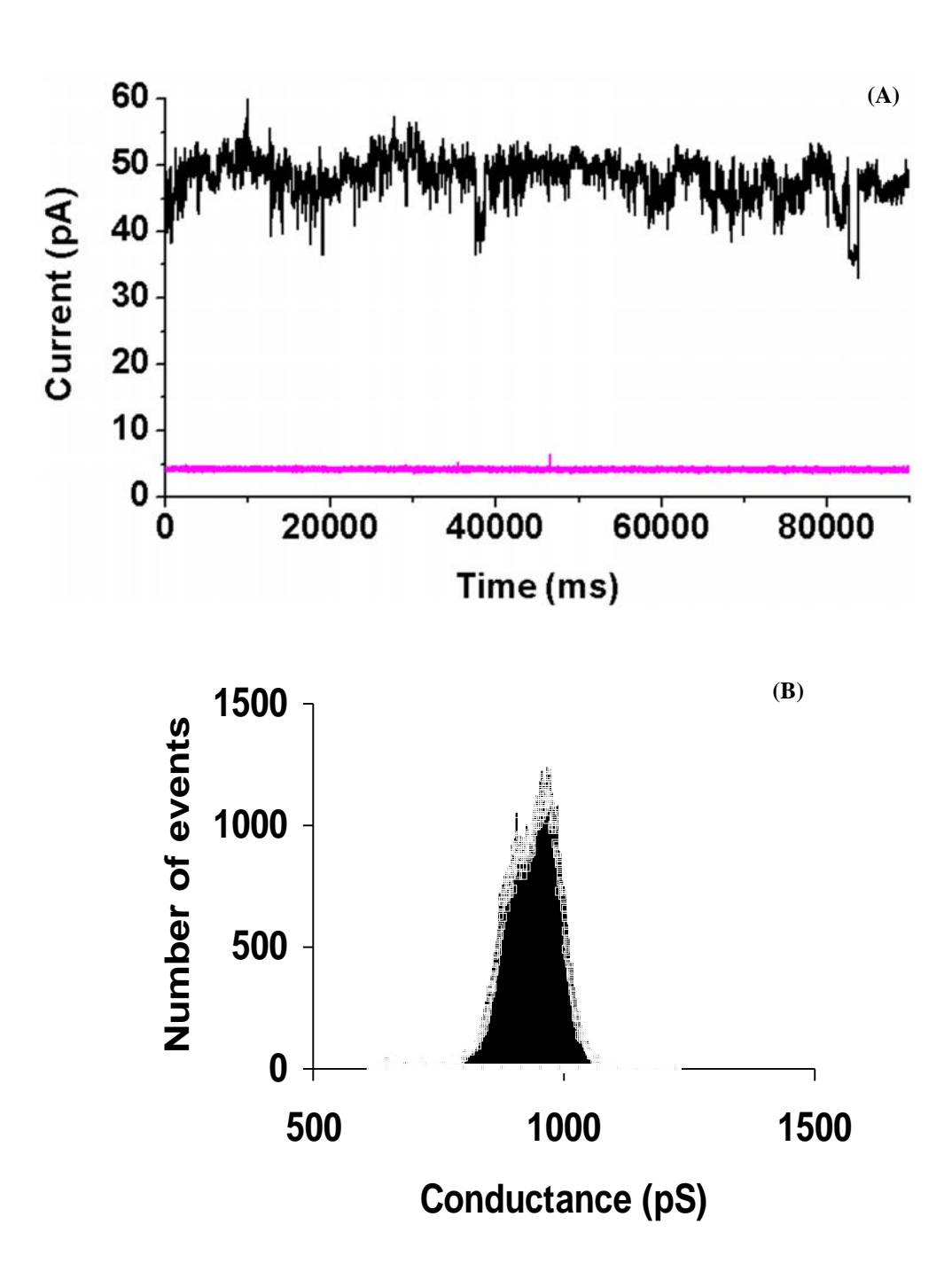


**Figure 5.5:** (A) Current vs time profile of DOPC pBLM without (in pink) and with (in black) 20  $\mu$ g/mL F-MWNT in 20 mM KCl and 20 mM HEPES at +50 mV. (B) Corresponding histogram for (A).

The electrical conductance caused by the nanoparticles suggests that transient holes formed in nanopore pBLM at applied voltage, triggering transient ion flow that was

measured as current spikes. Histograms of conductance distribution fitted by normal distribution yield average conductance amplitude of  $46.3 \pm 2.1$  pS for PEG terminated silica NPs and  $798.3 \pm 97.0$  pS for MWNT, shown in Figure 5.4 (B) and Figure 5.5 (B), respectively. Both PEG modified silica nanoparticles and MWNT were considered aggressive in term of the ability of inducing transient holes and allowing current to pass through lipid bilayer.

Planar BLM formed on standard electrophysiology cuvettes having an aperture about 500 µm in diameter exhibit low mechanical stability, exhibiting lifetimes on the order of an hour and rapidly breaking transmembrane potentials of 150 to 200 mV. However, pBLM formed on smaller orifices exhibit significantly higher stability [23]. Sub-micron aperture sizes gave pBLM an order of magnitude longer lifetime and tolerated several times higher transmembrane potentials [156]. For example, a pBLM formed on a 100 nm nanopore had a minimum breakdown voltage of 250 mV [25]. Moreover, these nano-sized pBLM exhibited properties typical of conventional pBLM, as evidenced by patterns of pore formation by ion channel proteins and ionophores [158]. Here, we have demonstrated that nanopore pBLM can be used to measure ENM-membrane interactions. Current traces following ENM addition showed the expected trends, including rapidly resealing current spikes and integral conductance similar to those observed in pBLM formed using conventional electrophysiology cuvettes.

The electrophysiological methods measure transmembrane ion flux, which is important for cell viability, material transport and intercellular signaling. The pBLM method leverages well established electrophysiology tools to characterize ENM induced membrane perturbations with single pore sensitivity, whereas the tBLM method is more

robust and uses less expensive equipment. High-throughput can be achieved for both electrochemical/electrophysiological methods via integration of customizable CMOS-based microfluidics and microsystem array architectures.

#### **5.5.** Conclusions

A pBLM was fabricated on nanopores drilled through silicon nitride windows using FIB. EIS characterization and the pore-forming peptide gramicidin have validated the system's ability to measure pore formation in pBLM. The effects of two types of ENM on the pBLM were investigated: (1) PEG functionalized silica-core nanoparticles and (2) COOH functionalized MWNT. Two phospholipid compositions were used to produce the pBLM: pure DOPC and a 3:1 mixture of POPC and POPE. Current traces following ENM addition showed a variety of trends, including rapidly resealing current spikes and extended conductance with longer duration. Electrochemical signatures were influenced by both the BLM's lipid composition and the ENM properties. Average pore conductance arising from MWNT interactions with pBLM formed from DOPC was about an order of magnitude larger than that arising from interaction of PEG-functionalized, silica-core ENM with pBLM formed from a POPC-POPE mixture.

### 6. DEVELOPMENT OF A MATHEMATICAL MODEL DECRIBING KINETICS OF ENM-BLM INTERACTION

#### 6.1. Abstract

The experimental studies showed that different nanoparticles generated different trends in the resistance of tethered bilayer lipid membrane (tBLM) vs. time profiles. A mathematical model was needed to help elucidate molecular processes responsible for time-dependent changes in tBLM resistance (R<sub>m</sub>) following ENM exposure and gain physical insight into the underlying nanoparticle-biomembrane interactions. In this chapter, we present a simple mechanistic kinetic model to describe interactions between engineered nanomaterials (ENM) and a tBLM. The mathematical model developed uses two kinetic constants to describe the rates of ENM binding to, and lipid removal from, the tBLM. The model was fit to R<sub>m</sub> vs. time data for interaction of a tBLM formed using DOPC with two types of ENM: functionalized polypropargyl glycolide nanoparticles (PGL) and polystyrene nanoparticles (PNP). The model was able to reproduce diverse trends in the R<sub>m</sub> vs. time data, including a continuous decrease in R<sub>m</sub> as well as an initial increase in R<sub>m</sub> followed by a decrease. The model also predicted that interactions of only a few nanoparticles with the tBLM were required measurable changes in the tBLM's R<sub>m</sub>. Hierarchical clustering was applied to pairs of optimized kinetic constants for various ENM. The resulting dendrograms indicated that ENM having different properties (composition, size, surface charge) could be statistically distinguished based on their influence on tBLM's R<sub>m</sub> using this approach. Results of this study provide insight into fundamental mechanisms by which ENM interact with biomembranes and may lead to

improved methods to rapidly screen ENM libraries for desired functional and biosafety profiles.

## 6.2. Introduction

The increasing use of ENM raises concerns about potential toxicity and health risks. Nanoparticles have been shown to penetrate cell membranes, but the internalization pathways by which ENM interact with biomembranes is still poorly understood [59]. Recent computer based modeling and simulations have been successfully used in studying lipid-lipid, lipid-protein interactions and lipid-nanoparticle interactions [35, 159]. For example, potassium ion transport across biomembranes incorporating valinomycin ionophore has been determined via passive permeation [32, 97]. Molecular dynamics usually yields time evolved force by numerically integrating Newton's equations of motion for a group of interacting particles. On the contrary, dissipative particle dynamics, dominated by friction and random forces in addition of Newton's law, are becoming more powerful in elucidating diverse mechanisms of ENM interaction with a cell membrane, ENM fate upon interaction with a cell membrane, and correlation of interaction patterns to physicochemical properties of ENM [35, 59, 61, 160]. Modeling using molecular dynamics shows that modes of nanoparticle interaction with biomembranes strongly depend on charge, size as well as surface functionalization of nanoparticles, and that the translocation rate of nanoparticles ranges from microsecond to second [160]. For example, modified and optimized atomistic models that enable simulations performed on the smallest scale under classical mechanics were used to simulate phospholipid bilayers [161, 162]. The simulated lipid bilayer composed of dipalmitoylphosphatidylcholine had similar lipid area and volume densities, in

accordance with those values measured in the experiments [163]. Pore forming and resealing behaviors across lipid bilayers were simulated using an atomistic model where electroporation occurred and lasted on the order of nanoseconds in lipid bilayers under a 0.5 V/nm electrical field [164, 165].

However, these computational studies are complicated, simulation time is limited and experimental data to support simulation results is lacking. Accordingly, systematic experimental methods and simple models are needed to help elucidate molecular interactions between ENM and cell membranes, to study ENM toxicity and to develop ENM-based biomedical technologies [13]. Furthermore, Ginzburg et al. reported application of a mesoscale thermodynamic model to predict membrane morphology changes upon exposure to various types of nanoparticles and the simulation results indicated formation of nanosized holes on lipid bilayers [166]. Unfortunately, this thermodynamic model is not able to provide kinetic mechanisms of nanoparticle interaction with biomembranes, e.g., characteristic time constant for nanoparticle adsorption into biomembranes or for other interaction modes. In addition, no direct experimental evidence was available to support or supplement the simulation results.

As a result, the purpose of this project was to develop a simple mechanistic mathematical model to describe kinetics/dynamics of ENM interactions with a tBLM and to predict diverse trends of ENM molecular interaction with a tBLM. The model was developed to help elucidate molecular processes responsible for time-dependent changes in  $R_{\rm m}$  following ENM exposure.

## **6.3.** Materials and Methods

Functionalized (-NH<sub>2</sub>, -COOH, -OH) PGL nanoparticles were synthesized in the laboratory of Dr Gregory L. Baker in the Chemistry Department at Michigan State University. Briefly, propargyl glycolide was first polymerized and then surface functionalized with -NH<sub>2</sub>, -COOH, -OH group via click chemistry [167]. An aliquot of PGL nanoparticle solution was added to a DPPTE/DOPC tBLM to reach a final concentration of 100  $\mu$ g/mL. The tBLM was formed using the protocol, as described in Section 2.3.5.

EIS was used to measure  $R_m$  trajectories in 5 h period following ENM exposure. The instrumentation setup for EIS characterization was the same as described in Section 2.3.6 except that the PGL in a concentration of 100  $\mu$ g/mL was studied rather than silica nanoparticles in a concentration of 300  $\mu$ g/mL.

# 6.4. Mathematical Model Development

Coarse-grained molecular dynamics models have been used to simulate interactions between nanoparticles and lipid bilayers [35, 160, 168]. These models are either on the basis of pair potentials with broad minima or MARTINI force field theory. However, these models are too expensive to adapt to fully atomistic simulations, limited by simulation time and dimensions. Moreover, it is almost unlikely to validate these models without any experimental data as support.

A goal of this study was to develop a simple kinetic model that could be validated based on our experimental measurements of ENM-BLM interactions. The ENM is assumed to first adsorb onto a tBLM into which it may partially insert itself, displacing lipids. Because the lipid bilayer is incompressible, the displaced lipids would flow into defects, thereby shrinking the pre-existing defects. At the same time, the adsorbed

nanoparticles can remove and capture lipids from tBLM in the vicinity of the adsorbed nanoparticles, enlarging defects in the tBLM. A defect area balance was applied to account for changes in tBLM defect area. The resulting equation would take into account the relative rates of (1) reductions in defect area as nanoparticles push into the tBLM, forcing lipid into defects, displacing lipids, and (2) increases in defect area as lipids are removed from the bilayer by the nanoparticles. The model would also include an equation that would calculate the changes in  $R_m$  (both positive and negative) in terms of the changes in defect area. The model should be as simple as possible while still capturing the elementary kinetic steps above to minimize the number of adjustable constants and allow optimal values of the constants to be determined and used to characterize differences in ENM' effects as a function of the ENM' and bilayer's properties.

In the conceptual model, the tBLM is considered as a pair of parallel plates, each of which offers resistance to ion flow across the tBLM. Because electrochemical resistances in series are additive, the overall  $R_m$  of the tBLM is sum of upper  $(R_u)$  and lower leaflet resistance  $(R_l)$  [16, 169], as shown in Equation (1). Electrical resistance is calculated as the product of resistivity ( ) and the thickness of the leaflet (l) divided by the cross-sectional area (A) [128, 170], shown in Equation (2).

$$R_m = R_u + R_l \tag{1}$$

$$R = \frac{...l}{A} \tag{2}$$

Each leaflet is assumed to include regions of continuous bilayer in parallel with defect regions that are filled with electrolyte. Thus, each leaflet's resistance can be calculated from the resistance of intact lipid aggregate within the leaflet  $(R_{bu}, R_{bl})$  in parallel with that leaflet's defect resistance  $(R_{du}, R_{dl})$ , shown in Equation (3) – (6).

Because continuous bilayer resistivity ( $_b$ ) is on the order of  $10^{12}$  cm, 10 orders of magnitude higher than defect resistivity ( $_d$ ), the key component dominating the overall tBLM resistance is the ratio of defect area ( $A_d$ ) to the continuous bilayer area ( $A_b$ ). For each leaflet, the total area, which is the sum of the defect area and continuous bilayer area, is fixed. Thus, changes in each leaflet's continuous bilayer area equal in magnitude to defect area but opposite in sign.

$$\frac{1}{R_u} = \frac{1}{R_{bu}} + \frac{1}{R_{du}} \tag{3}$$

$$\frac{1}{R_l} = \frac{1}{R_{bl}} + \frac{1}{R_{dl}} \tag{4}$$

$$R_{u} = \frac{\cdots_{b} \cdots_{d} l}{\cdots_{b} A_{du} + \cdots_{d} A_{bu}}$$
 (5)

$$R_{l} = \frac{\cdots_{b} \cdots_{d} l}{\cdots_{b} A_{dl} + \cdots_{d} A_{bl}}$$
 (6)

When a free ENM in the bulk liquid approaches a tBLM interface, the nanoparticle first adsorbs onto either continuous bilayer area or defect area to form complex. The number of complexes is  $n_3$  while the number of defects is  $n_2$ . ENM adsorption rate is proportional to number of free ENM  $(n_1)$  in the bulk solution only when the adsorption occurs within continuous bilayer area, shown in Equation (7). The rate of ENM adsorption onto defect area, the adsorption rate depends on not only ENM concentration but also defect area.

$$\frac{dn_3}{dt} = k_1 n_1 A_{du} + k_2 n_1 + k_4 n_1 A_{dl} \tag{7}$$

where  $k_1$ ,  $k_2$  and  $k_4$  are corresponding rate constants. For a highly insulating tBLM, defect area fraction is so low, less than  $10^{-10}$ , that corresponding complex formation rate with defects is assumed to be negligible and Equation (7) can be simplified as Equation (8) as following:

$$\frac{dn_3}{dt} = k_2 n_1 \tag{8}$$

When ENM interact with continuous bilayer region, they may become partially embedded in the bilayer and displace free (non-tethering) lipid molecules that would migrate into open defect regions, thereby shrinking the defects. Alternatively, defect region can be directly filled by ENM absorption within the same region. Both processes would reduce the defect area and thus increase  $R_m$  of a tBLM. Tethering lipids that constitute the lower leaflet presumably cannot be displaced due to their strong chemical affinity to the underlying gold substrate. Therefore, the non-tethering lipid fraction ( ) determines maximum volume of free lipids that can be displaced by ENM in lower leaflet. Limited to the thickness of a tBLM, maximum nanoparticle penetration depth was estimated using Equation (9). Given the available free lipids in the tBLM and available sites on the surface of a spherical nanoparticle having a radius  $r_n$  and the formula for a spherical cap, Equation (10) – (12) were developed to account for the volume of free lipids displaced by a single ENM.

$$\Phi = 1.5(r_n + \alpha l) - 0.5\sqrt{9(r_n + \alpha l)^2 - 24\alpha l r_n}$$
(9)

$$V_n = \frac{f}{3} (\Phi + l)^2 (3r_n - l - \Phi)$$
(10)

$$V_{nl} = \frac{f}{3} \, \Phi^2 (3r_n - \Phi) \tag{11}$$

$$V_{nu} = V_n - V_{nl} \tag{12}$$

where ( < 5 nm) is the penetration depth of ENM through the tBLM. The terms  $V_n$ ,  $V_{nl}$ , and  $V_{nu}$  are the volume of total free lipids, free lipids from lower leaflet, and free lipids from upper leaflet, displaced by ENM, respectively. After ENM adsorption, free lipids are assumed to be captured from the tBLME and deposited onto the ENM as a supported bilayer. The lipid capture rates from the upper and lower leaflets are described in Equations (13) and (14), respectively. Lipid capture and removal is predicted to cease once the ENM surface is completely coated by a bilayer of free lipids, thus limiting the amount of lipid that can be captured from the tBLM.

$$\frac{dV_{cu}}{dt} = k_3 n_3 \left[1 - \frac{V_{cu} + V_{cl}}{(4f \, r_n^2) 2l n_3}\right] \tag{13}$$

$$\frac{dV_{cl}}{dt} = k_5 n_3 \left[1 - \frac{V_{cl} + V_{cu}}{(4f \, r_n^2) 2l n_3}\right] \left(1 - \frac{V_{cl}}{\mathbf{Q}(A_{dl} + A_{bl})}\right) \tag{14}$$

In Equations (13) and (14),  $V_{cu}$  and  $V_{cl}$  are free lipid volume captured by ENM from the upper and lower leaflet with corresponding rate constants  $k_3$  and  $k_5$ , respectively. In order to simplify the model,  $k_3$  and  $k_5$  are set to be equal. Then, Equation 14 can be written as follow:

$$\frac{dV_{cl}}{dt} = k_3 n_3 \left[1 - \frac{V_{cl} + V_{cu}}{(4f \, r_n^2) 2l n_3}\right] \left(1 - \frac{V_{cl}}{\mathsf{Ql}(A_{dl} + A_{bl})}\right) \tag{15}$$

A Balance on defect areas in each leaflet, which strongly influence the tBLM resistance, can written based on initial defect area ( $A_{du0}$  and  $A_{dl0}$ ), defect shrinkage by nanoparticle displacement of lipids ( $V_{nl}$  and  $V_{nu}$ ) and defect enlargement by free lipid capture by nanoparticles ( $V_{cu}$  and  $V_{cl}$ ), are shown in Equations (16) and (17)

$$A_{du} = A_{du0} - \frac{V_{nu}n_3}{l} + \frac{V_{cu}}{l} \tag{16}$$

$$A_{dl} = A_{dl0} - \frac{V_{nl}n_3}{l} + \frac{V_{cl}}{l} \tag{17}$$

## 6.5. Results and Discussion

#### 6.5.1. Model validation

The mechanistic model was first validated by simulating the continuous  $R_m$  decay curvess that were observed when PNP interacted with tBLM. Each type of PNP interaction with tBLM was performed in triplicates. The mathematical model was fit to the experimental  $R_m$  profiles. Optimal values of the rate constants are shown in Table 6.1:  $k_2$  for adsorption and  $k_3$  for lipid removal. Student t test shows that there is significant difference in magnitude of  $k_2$ , which varied from  $10^{-15}$  to  $10^{-12}$  min<sup>-1</sup> between PNP in different size and surface functionality. For both COOH PNP and amidine PNP, smaller PNP exhibited larger  $k_2$  values and thereby a more rapid formation rate of ENM complexes. This trend suggests that smaller ENM with larger specific surface areas adsorb more quickly to tBLM. On the other hand, negatively charged COOH PNP adsorbed to tBLM much faster than positively charged, indicating negatively charged ENM are more active and potent in terms of binding to tBLM surface. This trend is mainly due to the aggregation of positively charged nanoparticles via negatively charged lipid mediated crosslink [171].

The goodness of fit of the mechanistic model was compared with the previously developed exponential decay model. Figure 6.1 shows experimental  $R_{\rm m}$  profiles extracted from EIS data (open symbols), empirical exponential model predicted  $R_{\rm m}$  profiles

(dashed lines), and mechanistic model predicted  $R_m$  profiles (solid lines) over 310 min when COOH (20 nm, Figure 6.1 (A)), COOH PNP (100 nm, Figure 6.1 (B)), amidine PNP (23 nm, Figure 6.1 (C)), or amidine PNP (120 nm, Figure 6.1 (D)), were exposed to tBLM after the first data point was recorded. The  $R_m$  trajectories predicted by the mechanistic model agree well with the experimental data. The observed variation in the initial  $R_m$  values is due to the extremely high sensitivity of  $R_m$  to defect area. For example, the change of tBLM area fraction from 100% to 99.999999999998% is predicted to cause a 50% decrease in the  $R_m$  value.

**Table 6.1:** Kinetic constants of functionalized PNP. The number after PNP stands for size of PNP while the last number shows the replication.

ENM	k <sub>2</sub> (min <sup>-1</sup> )	k <sub>3</sub> (mL/min)
COOH PNP 20_1	1.86×10 <sup>-12</sup>	$3.23\times10^{-19}$
COOH PNP 20_2	2.55×10 <sup>-12</sup>	$2.54 \times 10^{-19}$
COOH PNP 20_3	$1.56 \times 10^{-12}$	$2.78 \times 10^{-19}$
COOH PNP 100_1	$7.52 \times 10^{-13}$	$2.16 \times 10^{-19}$
COOH PNP 100_2	8.21×10 <sup>-13</sup>	$0.64 \times 10^{-19}$
COOH PNP 100_3	11.5×10 <sup>-13</sup>	$2.45 \times 10^{-19}$
Amidine PNP 20_1	5.73×10 <sup>-14</sup>	$3.09 \times 10^{-19}$
Amidine PNP 20_2	5.01×10 <sup>-14</sup>	$3.15 \times 10^{-19}$
Amidine PNP 20_3	2.51×10 <sup>-14</sup>	$3.25\times10^{-19}$
Amidine PNP 120_1	$3.69 \times 10^{-15}$	$1.69 \times 10^{-19}$
Amidine PNP 120_2	2.23×10 <sup>-15</sup>	$2.05 \times 10^{-19}$
Amidine PNP 120_3	$0.92 \times 10^{-15}$	$1.53 \times 10^{-19}$

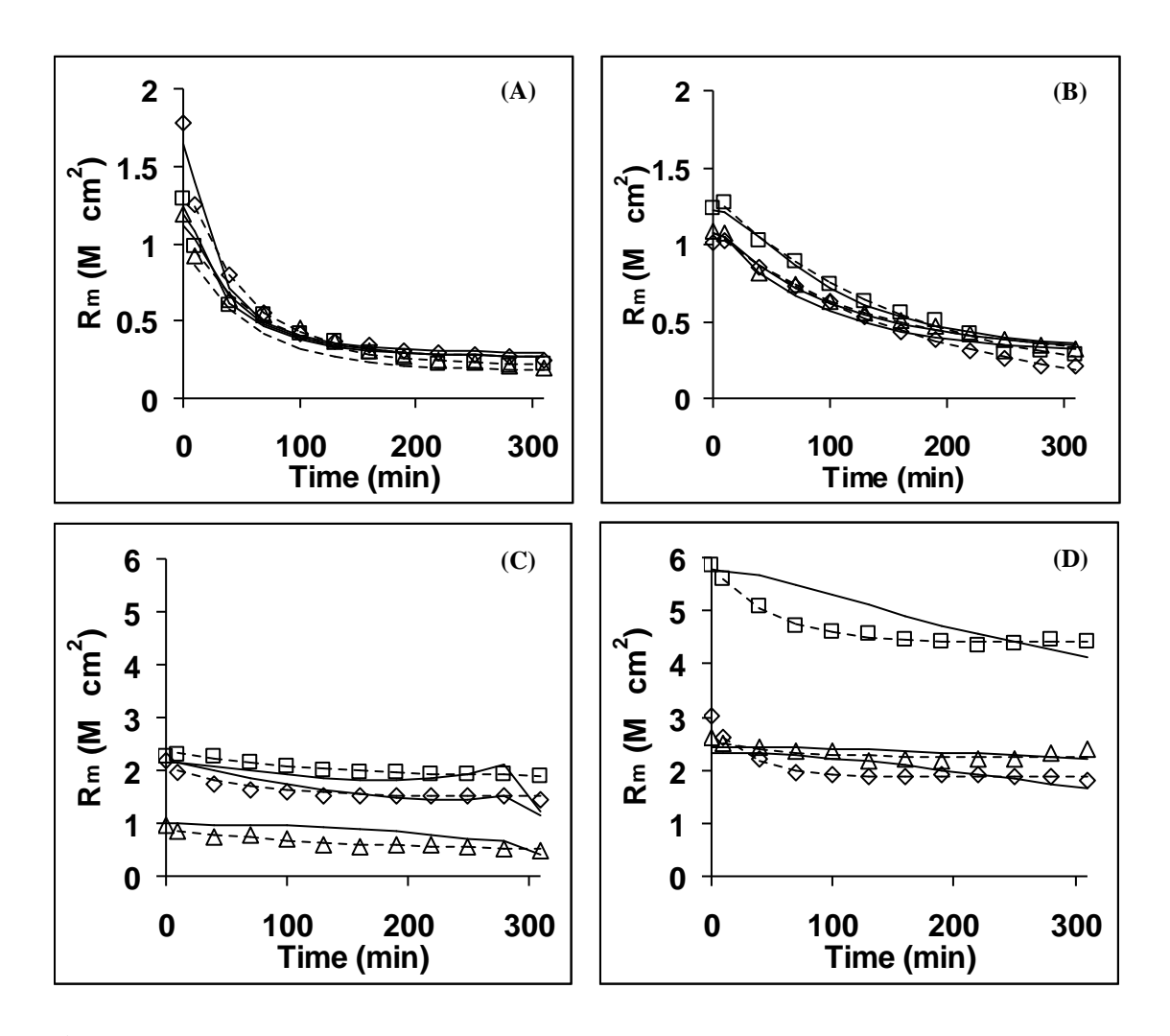


**Figure 6.1:**  $R_m$  profiles over time during tBLM interaction with 100 µg/mL PNP in 10 mM KCl. (A): COOH PNP (20 nm), (B): COOH PNP (100 nm), (C): Amidine PNP (23 nm) and (D): Amidine PNP (120 nm).  $R_m$  was extracted from EIS data fit by equivalent circuit model. Three replicates were done, labeled as open diamonds, squares and triangles. All dashed and solid curves were fit  $R_m$  by the empirical exponential model and by the mechanistic model, respectively.

The attraction between ENM and the lipid head and/or tail groups is the dominant physical driving force for ENM adsorption onto tBLM surface to form complexes [159]. The complexes formed from ENM adsorbing onto tBLM surface could either displace lipids or remove and capture lipids, resulting in diverse trends of  $R_m$  trajectories. The

continuous decrease in  $R_m$  observed when the tBLM was exposed to PNP is consistent with lipid removal being the dominant event. However, an alternative mechanistic explanation might also explain the experimentally observed trend. For example, nanoparticle induced BLM surface reconstruction marked by a change in local lipid packing density has been shown in both experimental studies [129] and molecular dynamics simulations [152]. Alternatively, insertion of single carbon nanotubes has been reported to trigger alternation in the local packing of lipid molecules, with enhanced diffusion coefficient of small molecules through the BLM [152]. These mechanisms would also be consistent with monotonic decreasing  $R_m$  in the presence of PNP. Other interesting behavior of BLM in response to nanoparticle exposure have been reported, including transition of lipid vesicles from the usual sphere structure into stable pearls necklaces [172].

To further validate the mechanistic model, its ability to simulate/predict a nanoparticle-induced initial increase in  $R_m$ , followed by a decrease was evaluated. The model predicts that the shape of the  $R_m$  time trajectories is controlled by the relative rates of two processes: (1) nanoparticle adsorption and resulting lipid displacement, which tends to increase  $R_m$ , and (2) lipid capture by nanoparticles, which tends to decrease  $R_m$ . When nanoparticle adsorption and lipid displacement initially dominate lipid capture, the mechanistic model predicts an initial increase in  $R_m$ . The model was fit to experimental  $R_m$  trajectories obtained for various types of functionalized PGL nanoparticles. Figure 6.2 shows experimental  $R_m$  profiles extracted from EIS data in open symbols, and mechanistic model simulated  $R_m$  profiles in solid lines in the presence of functionalized PGL nanoparticles (COOH PGL, OH PGL or NH<sub>2</sub> PGL). The mechanistic model was

able to predict  $R_m$  trajectories that included an initial  $R_m$  increase followed by a decrease (Figure 6.2 (A) and (B)). The initial increase is attributed to nanoparticle-induced lipid displacement, resulting in defect area reduction and a corresponding increase in  $R_m$ .

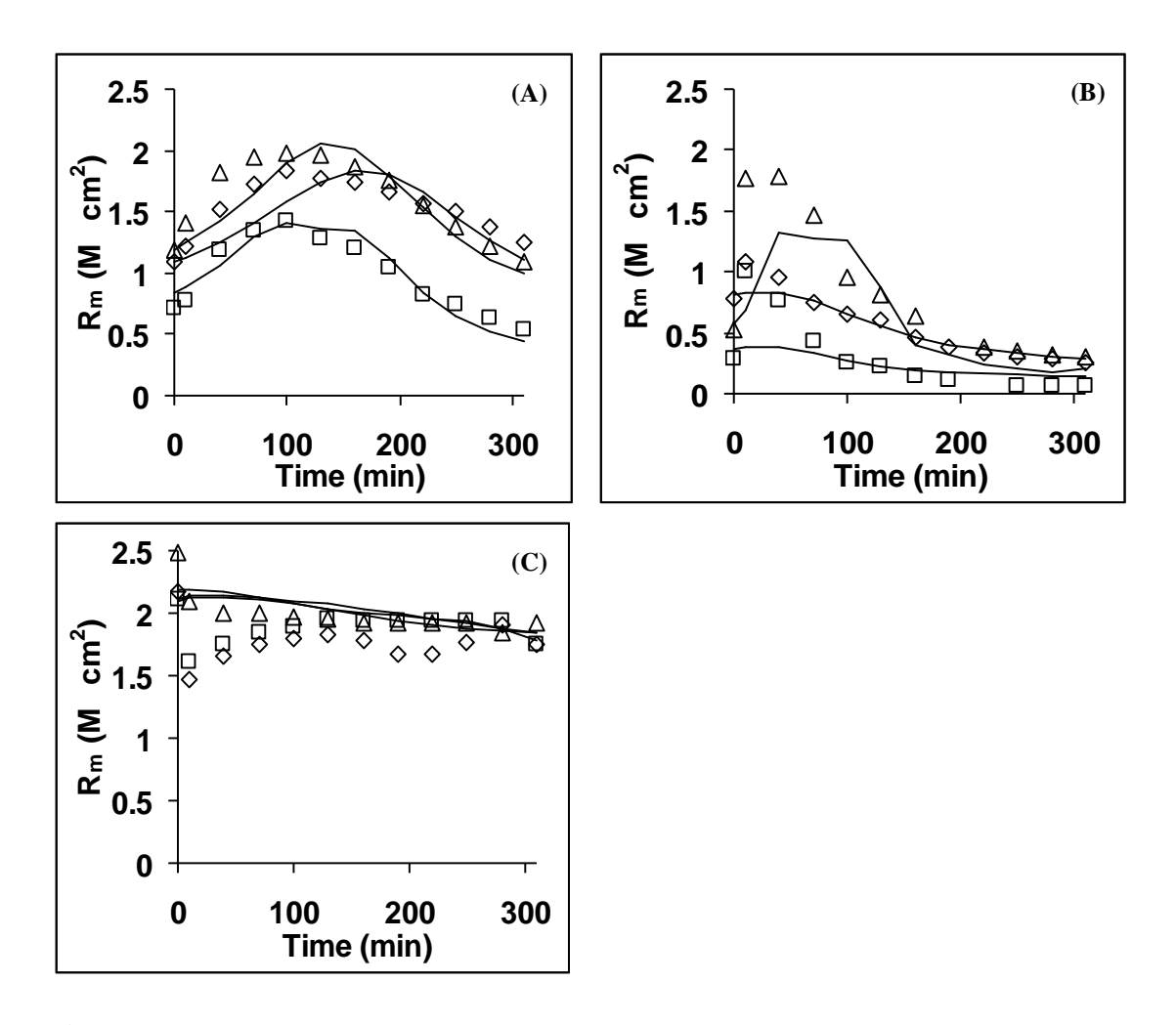


**Figure 6.2:**  $R_m$  profiles over time during tBLM interaction with 100 µg/mL functionalized PGL in 100 mM KCl. (A): OH PGL (128 nm), (B): COOH PGL (100 nm) and (C): NH<sub>2</sub> PGL (94 nm).  $R_m$  was extracted from EIS data fit by equivalent circuit model. Three replicates were done, labeled as open diamonds, squares and triangles. All solid curves were fit  $R_m$  by the mechanistic model.

This result may also be consistent with negatively charged nanoparticles inducing surface reconstruction, where anionic nanoparticles interacted preferentially with  $N^+$  terminus of the lipid bilayers, increasing lipid packing density [129]. Similar to our two-

kinetic model, a two-step microstructure model composed of insertion  $(k_+)$  and desorption  $(k_-)$  kinetics was reported to successfully predict the association kinetics of Ergosta-5,7,9(11),22-tetraen-3 $\beta$ -ol with model lipid bilayers [173].

To our knowledge, this mechanistic model is the first one that has been shown to simulate a variety of ENM induced various  $R_{\rm m}$  trajectories, including a continuous decrease and an increase followed by a decrease and. In addition, the model has few constants, allowing differences in experimental trends to be interpreted in terms of physically meaningful rate constants for ENM adsorption to the tBLM ( $k_2$ ) and for lipid removal from the tBLM ( $k_3$ ), as illustrated below.

**Table 6.2:** Kinetic constants of functionalized PGL. The number after PGL shows the replication.

ENM	k <sub>2</sub> (min <sup>-1</sup> )	k <sub>3</sub> (mL/min)
OH-PGL_1	$0.80 \times 10^{-12}$	$7.31 \times 10^{-21}$
OH-PGL_2	$1.90 \times 10^{-12}$	$9.47 \times 10^{-21}$
OH-PGL_3	$1.22 \times 10^{-12}$	$8.94 \times 10^{-21}$
NH <sub>2</sub> -PGL_1	$2.52 \times 10^{-13}$	$2.60 \times 10^{-21}$
NH <sub>2</sub> -PGL_2	$2.24 \times 10^{-13}$	$6.55 \times 10^{-21}$
NH <sub>2</sub> -PGL_3	$2.79 \times 10^{-13}$	$5.86 \times 10^{-21}$
COOH-PGL_1	$1.37 \times 10^{-12}$	$2.15 \times 10^{-20}$
COOH-PGL_2	$2.19 \times 10^{-12}$	$3.85 \times 10^{-20}$
COOH-PGL_3	$0.94 \times 10^{-12}$	$2.23 \times 10^{-20}$

Table 6.2 shows kinetic constants obtained by fitting the mechanistic model to experimental data for functionalized PGL nanoparticles. Both OH PGL and COOH PGL show adsorption rate constant on the order of  $10^{-12}$  min<sup>-1</sup>, allowing  $R_m$  to initially increase for 100 min and 40 min in Figure 6.2 (A) and (B), respectively. The difference in duration time of the  $R_m$  increase results from large lipid removal rate constant of COOH

PGL. The lipid removal rate constant for COOH PGL is nearly one order of magnitude higher than that for  $NH_2$  and OH PGL. On the contrary,  $NH_2$  PGL shows the lowest binding rate constant due to its negative charge on surface, resulting in an abrupt decay in  $R_m$  trajectories of Figure 6.2 (C).

Bi-exponential functions have been used in studying permeation kinetics of druglike bases across the lipid bilayer in order to simulate two phases of fluorescence responses including an initial increase and then a decrease [174]. Such models could presumably predict an initial increase in R<sub>m</sub> followed by a decrease. However, such exponential models lack a mechanistic basis that allows differences in responses to be interpreted in terms of molecular interactions between the ENM and lipid bilayer. The two kinetic parameters in our model describe the relative rates of binding and lipidcapture processes, whose balance determines the shape of the R<sub>m</sub> time trajectories. A similar mechanistic approach may also enable development of a simple kinetic model that predicts ENM fate upon interaction with other types of biomembranes, including planar BLM or cell plasma membranes. Results of such models could be validated in part using molecular dynamics models, which have predicted, for example, that a spherical particle may first adheres to a lipid bilayer, then become partially coated by lipids and finally rupture the membrane [166, 175]. Whether the interaction favors ENM adsorption or lipid removal is dependent on the competition between bending energy and stretching energy [159]. For example, very small nanoparticles strongly adsorbed and embedded into lipid bilayer surface due to overwhelming bending energy cost while nanoparticles caused defect formation and became wrapped in captured lipids. The model also helps explain various patterns of R<sub>m</sub> change over time by correlating meaningful physical

processes. These binding/adsorption and lipid removal events predicted by the mechanistic model were also consistent with molecular dynamics simulations based on Cooke coarse-grained model, showing ENM induced ruptured ENM-BLM morphology when ENM interact with BLM [36]. An alternative mechanism that is consistent with our experimental trends and can potentially explain an increase or decrease of  $R_m$  is that nanoparticles could either induce BLM phase transition either to the gel state above the phase-transition temperature transition to the liquid-crystalline state below the phase transition temperature [176].

## **6.5.2.** Statistical analysis

In Chapter 3, we demonstrated that the PNP-tBLM interactions could be statistically distinguished based on the PNP's size and surface group. The approach used hierarchical clustering analysis of best-fit constants from an empirical exponential decay model fit to the  $R_m$  vs. time curves obtained during PNP-tBLM interactions (Figure 3.5). Based on that result, we hypothesized that hierarchical clustering analysis of kinetic parameters extracted from the mechanistic model could distinguish functionalized PNP in different sizes. The two constants  $k_2$  and  $k_3$  were analyzed using hierarchical clustering procedures in R software (Version 2.13.2: The R foundation for statistical computing) for each replicate. Figure 6.3 shows dendrogram of hierarchical clustering using  $k_2$  and  $k_3$ , which displays the Euclidean distance versus clustered objects and measures similarity between samples and clusters. As in Figure 3.5, each replicate of PNP having same functional surface group and the same size clustered together. The height scale in Figure 6.3 is larger than that in Figure 3.5, indicating that the mechanistic model provided higher

resolution for distinguishing ENM. The similarity between ENM can be measured more sensitively using the mechanistic model.

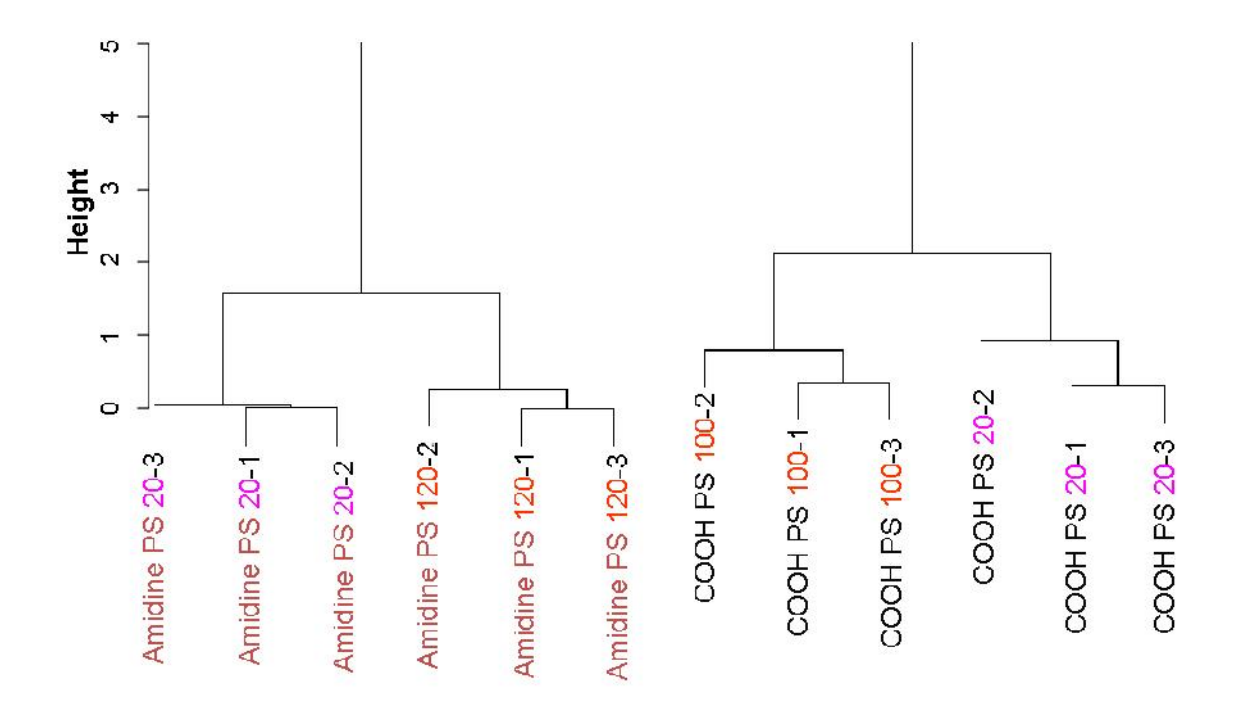


**Figure 6.3:** Hierarchical clustering dendrogram of COOH (20 and 100 nm) and amidine PNP (23 nm and 120 nm) interaction with tBLM. Distances between objects when forming the clusters are calculated by Euclidean distance. Analysis of parameters  $k_2$  and  $k_3$  extracted from mechanistic model was performed by evaluating distances between clusters using Ward's method.

We also tested whether hierarchical clustering of  $k_2$  and  $k_3$  constants could distinguish functionalized PGL nanoparticles, some of whose interaction with the tBLM gave an initial increase in  $R_m$  followed by a decrease. The dendrogram in Figure 6.4 clearly shows three clustered groups for OH, COOH, NH<sub>2</sub> PGL, respectively. Negatively charged NH<sub>2</sub> PGL first clustered with neutrally OH PGL, followed by COOH PGL. This result illustrates that the mechanistic model enables hierarchical clustering analysis to be applied both to ENM that give monotonically decreasing  $R_m$  vs time curves that could alternatively be described using an empirical exponential model as well as ENM that give

an initial increase in  $R_m$ , followed by a decrease. This latter class of ENM cannot be reasonably described by a simple exponential model.

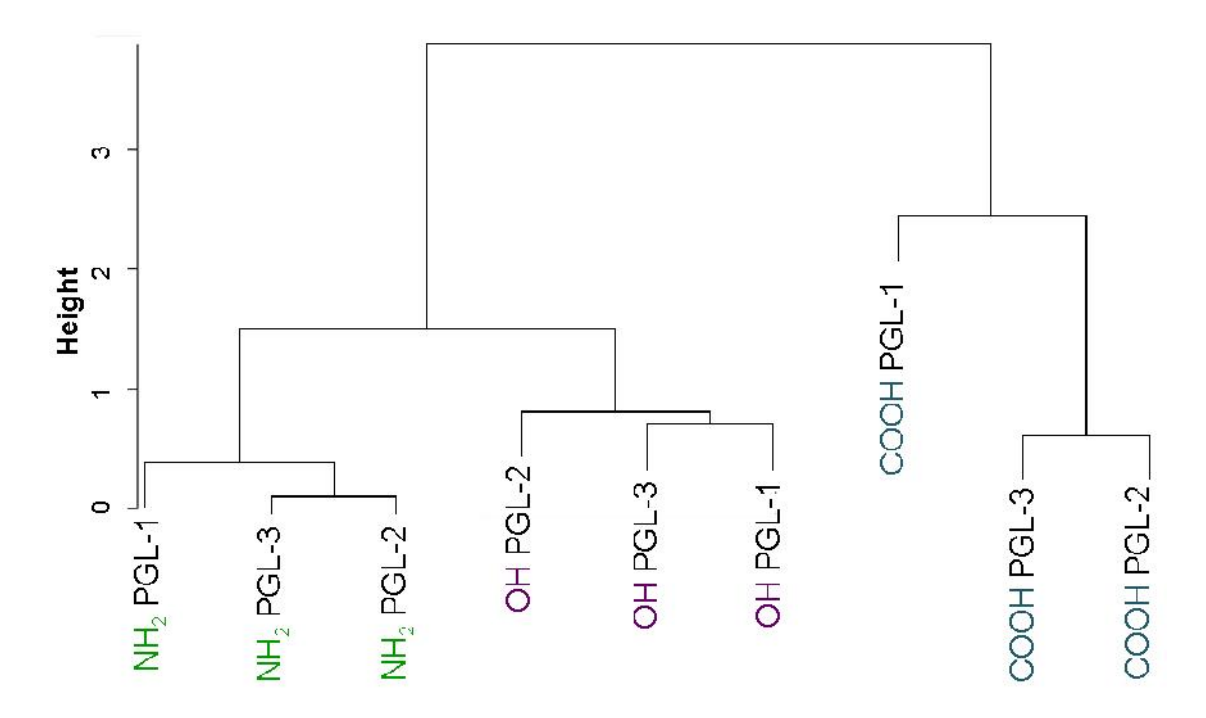


**Figure 6.4:** Hierarchical clustering dendrogram of COOH, OH, and NH<sub>2</sub> PGL interaction with tBLM. Distances between objects when forming the clusters are calculated by Euclidean distance. Analysis of parameters k<sub>2</sub> and k<sub>3</sub> extracted from mechanistic model was performed by evaluating distances between clusters using the Ward's method.

The mechanistic model has been shown to reproduce two distinct trends in  $R_m$  vs time curves observed during tBLM exposure to tBLM. However, other patterns of  $R_m$  trajectories are possible. For example, we previously reported minor, but continuous increase in  $R_m$ , triggered by exposure of a tBLM to PEG terminated silica-core nanoparticles [22]. The model can describe such a trend (results not shown) by further reducing  $k_3$  below that used to obtain the initial increase followed by a decrease (e.g., Figure 6.2 (A)). The model could also be adapted to simulate other experimental  $R_m$  changes by adjusting  $k_2$  and  $k_3$ , or even adding additional mechanistic detail to the model. In this way, it may be possible to use tBLM-exposure experiments as a tool to interpret

patterns of ENM-biomembrane interactions. The tBLM method is readily scalable using microelectrodes and robotic fluid delivery, so that the method could eventually be used as a high-throughput screening tool for ENM libraries to identify ENM candidates that provide desired properties regarding toxicity, suitability for delivering drugs across biomembranes, etc.

## **6.6. Conclusions**

A simple mechanistic model has been developed that depicts dynamic interactions between ENM and tBLM including ENM-tBLM binding/adsorption and lipid displacement/removal. The model was validated by comparing its predictions to R<sub>m</sub> vs time curves obtained using EIS during exposure of a tBLM to functionalized PNP and PGL. Differences in ENM size or surface functional groups resulted in differences in  $R_{\rm m}$ profiles, a monotonically decreasing curve, and an initial increase followed by a decrease. The model was able to reasonably describe all the observed trends, demonstrated the model's robustness in describing kinetics of ENM-tBLM interactions. Best-fit values of key kinetic constants for ENM adsorption to the tBLM (k2) and ENM removal of lipid from the tBLM (k<sub>3</sub>) were used for hierarchical clustering analysis. The results indicated that the ENM could be classified by size and surface functional group, and that clustering based on the mechanistic model's kinetic parameters gave a higher resolution than clustering based on an empirical exponential model. This finding confirmed the hypotheses that the mechanistic model can predict diverse trends of ENM-tBLM interactions and that its parameters can be used to distinguish ENM via their kinetics of tBLM interaction. The novel methods presented here could be adapted to high throughput applications for a wide range of ENM and synthetic BLM compositions to design ENM with desired functional and biosafety profiles.

## 7. CONCLUSIONS

The growing market for ENM-enhanced products has driven interest in developing ENM that have a desired set of functional properties, can be economically produced, and are nontoxic. The work presented in this dissertation mainly focused on developing electrochemical, electrophysiological and mathematical methods to characterize the interactions between ENM and biomembranes, discriminate ENM effects, and predict kinetic mechanisms of how ENM interact with biomembranes. We applied a bottom-up, biomimetic approach based on two types of biomembrane platforms, tBLM and pBLM, to explore the effect of the ENM's composition, size, surface charge and functional group on its ability to induce ion flow across biomembranes.

Each of the BLM platforms offers distinct advantages. The tBLM method measures total transmembrane ion flux across a macroscopic patch of biomembrane, whereas the pBLM method leverages well established electrophysiology tools to characterize ENM-induced membrane perturbations with single-pore sensitivity. The tBLM method offers higher biomembrane stability and uses less-expensive equipment, whereas the pBLM method reports molecular-level pore formation with millisecond time resolution. Both platforms are potentially adaptable to high-throughput applications via integration of microfluidics and microsystem array architectures. Coupled with statistical analysis, both methods are able to distinguish ENM effects on BLM resistances using an empirical exponential model, which is consistent with our hypothesis.

Both approaches are based on molecular interactions between ENM and BLM, the assay results are sensitive to the solution chemistry. For example, the electrochemical methods require a sufficiently high ionic strength to conduct current and obtain a

reasonable signal to noise ratio but not so high as to induce ENM aggregation. Because ENM aggregation is strongly affected by ionic strength, electrolyte composition must be considered into context of ion conductivity, ENM dispersion stability, and biological relevance. In general, BLM-based assays can be performed at much lower electrolyte concentrations than is possible in *in-vivo* and *in-vitro* assays, which often suffer from ENM aggregation. Furthermore, BLM-based assays that were originally developed to study ion channel proteins, toxins, and other agents that disrupt cell membranes appear to be useful for ENM when proper consideration is given to key factors including electrolyte concentration and BLM composition.

Results of this study have established for the first time that nanostructured biomimetic interfaces containing a synthetic BLM can distinguish between nanoparticles based on their size and surface functional group. This result suggests that biomembrane methods might be well suited to screen ENM libraries for nanoparticles that have desirable biotoxicity or drug-delivery properties. A mechanistic kinetic model was constructed to depict the interactions between ENM and tBLM. The kinetic rate constants including  $k_2$ , which describes the ENM adsorption rate, and  $k_3$ , which describes to the lipid capture rate, were evaluated using experimental  $R_{\rm m}$  trajectories for a variety of ENM. The model successfully predicted all the observed  $R_{\rm m}$  trends, including a continuous decrease and an initial increase followed by a decrease. The finding validated the model's ability to describe dynamics of ENM-tBLM interactions using two kinetic constants. These constants have the potential to provide physical insight into ENM-biomembrane interactions. Both  $k_2$  and  $k_3$  are affected by ENM physiochemical properties including size, surface charge, core materials and functional groups as well as

BLM properties, e.g. BLM composition and BLM intrinsic curvature. Future work is warranted to explore the utility of the model to elucidate interactions between ENM and biomembranes and to correlate the properties of ENM with their effect on biomembranes. Additional structure could also be added to the model, allowing it to capture additional dimensions of ENM-biomembrane interactions and to predict quantitative structure-activity relationships for rational ENM design. Such knowledge would aid in development of guidelines for design and screening of ENM for special applications. For example, in targeted drug delivery applications, the model could guide efforts to develop ENM that simultaneously exhibit a desired biomembrane translocation efficacy and an attractive toxicity profile. In this way, the research could facilitate nanomedicine formulation technologies and computer-aided drug design.

The integrated experimental and mechanistic modeling methods we developed have demonstrated robustness and versatility in characterizing biomembrane-ENM interaction. They are also they are adaptable to high throughput mode for screening ENM libraries. The knowledge obtained from this work provides insights into both tunable ENM formulation and targeted molecular interactions.

# **REFERENCES**

#### REFERENCES

- [1] I. Brigger, C. Dubernet, P. Couvreur, Nanoparticles in cancer therapy and diagnosis, Advanced Drug Delivery Reviews, 54 (2002) 631-651.
- [2] J.F. Hicks, D.T. Miles, R.W. Murray, Quantized double-layer charging of highly monodisperse metal nanoparticles, Journal of the American Chemical Society, 124 (2002) 13322-13328.
- [3] N.J. Walker, J.R. Bucher, A 21st century paradigm for evaluating the health hazards of nanoscale materials?, Toxicol Sci, 110 (2009) 251-254.
- [4] D.B. Warheit, Debunking Some Misconceptions about Nanotoxicology, Nano Letters, 10 (2010) 4777-4782.
- [5] G. Oberdorster, A. Maynard, K. Donaldson, V. Castranova, J. Fitzpatrick, K. Ausman, J. Carter, B. Karn, W. Kreyling, D. Lai, S. Olin, N. Monteiro-Riviere, D. Warheit, H. Yang, Principles for characterizing the potential human health effects from exposure to nanomaterials: elements of a screening strategy, Particle and Fibre Toxicology, 2 (2005) 8.
- [6] I.L. Hsiao, Y.J. Huang, Titanium oxide shell coatings decrease the cytotoxicity of ZnO nanoparticles, Chem Res Toxicol, 24 (2011) 303-313.
- [7] N. Li, J.R. Harkema, R.P. Lewandowski, M. Wang, L.A. Bramble, G.R. Gookin, Z. Ning, M.T. Kleinman, C. Sioutas, A.E. Nel, Ambient ultrafine particles provide a strong adjuvant effect in the secondary immune response: implication for traffic-related asthma flares, Am J Physiol Lung Cell Mol Physiol, 299 (2010) 18.
- [8] A. Nel, T. Xia, L. Madler, N. Li, Toxic potential of materials at the nanolevel, Science, 311 (2006) 622-627.
- [9] C. Buzea, Pacheco, II, K. Robbie, Nanomaterials and nanoparticles: Sources and toxicity, Biointerphases, 2 (2007) MR17-MR71.
- [10] A. Kroll, M.H. Pillukat, D. Hahn, J. Schnekenburger, Current in vitro methods in nanoparticle risk assessment: Limitations and challenges, European Journal of Pharmaceutics and Biopharmaceutics, 72 (2009) 370-377.
- [11] A.E. Nel, L. Madler, D. Velegol, T. Xia, E.M.V. Hoek, P. Somasundaran, F. Klaessig, V. Castranova, M. Thompson, Understanding biophysicochemical interactions at the nano-bio interface, Nature Materials, 8 (2009) 543-557.
- [12] J. Rejman, V. Oberle, I.S. Zuhorn, D. Hoekstra, Size-dependent internalization of particles via the pathways of clathrin-and caveolae-mediated endocytosis, Biochemical Journal, 377 (2004) 159-169.

- [13] P.J. Borm, D. Robbins, S. Haubold, T. Kuhlbusch, H. Fissan, K. Donaldson, R. Schins, V. Stone, W. Kreyling, J. Lademann, J. Krutmann, D. Warheit, E. Oberdorster, The potential risks of nanomaterials: a review carried out for ECETOC, Part Fibre Toxicol, 3 (2006) 11.
- [14] C. Rossi, J. Chopineau, Biomimetic tethered lipid membranes designed for membrane-protein interaction studies, European Biophysics Journal with Biophysics Letters, 36 (2007) 955-965.
- [15] S.D. Conner, S.L. Schmid, Regulated portals of entry into the cell, Nature, 422 (2003) 37-44.
- [16] H.T. Tien, A.L. Ottova, Membrane Biophysics as viewed from experimental bilayer lipid membranes, 1 ed., Elsevier, Amsterdam; New York, 2000.
- [17] S.B. Hladky, D.A. Haydon, Ion transfer across lipid membranes in the presence of gramicidin A: I. Studies of the unit conductance channel, Biochimica et Biophysica Acta (BBA) Biomembranes, 274 (1972) 294-312.
- [18] R. Margalit, A. Shanzer, A study of Li+-selective permeation through lipid bilayer membranes mediated by a new ionophore (AS701), Biochim Biophys Acta, 649 (1981) 441-448.
- [19] R. Schonherr, M. Hilger, S. Broer, R. Benz, V. Braun, Interaction of Serratia marcescens hemolysin (ShlA) with artificial and erythrocyte membranes. Demonstration of the formation of aqueous multistate channels, Eur J Biochem, 223 (1994) 655-663.
- [20] S. Terrettaz, M. Mayer, H. Vogel, Highly electrically insulating tethered lipid bilayers for probing the function of ion channel proteins, Langmuir, 19 (2003) 5567-5569.
- [21] S.R. Jadhav, Y. Zheng, R.M. Garavito, R.M. Worden, Functional characterization of PorB class II porin from Neisseria meningitidis using a tethered bilayer lipid membrane, Biosensors & Bioelectronics, 24 (2008) 831-835.
- [22] Y. Liu, Z. Zhang, Q. Zhang, G.L. Baker, R.M. Worden, Biomembrane disruption by silica-core nanoparticles: Effect of surface functional group measured using a tethered bilayer lipid membrane, Biochimica et Biophysica Acta (BBA) Biomembranes, 1838 (2014) 429-437.
- [23] A. Hirano-Iwata, K. Aoto, A. Oshima, T. Taira, R.T. Yamaguchi, Y. Kimura, M. Niwano, Free-Standing Lipid Bilayers in Silicon Chips-Membrane Stabilization Based on Microfabricated Apertures with a Nanometer-Scale Smoothness, Langmuir, 26 (2010) 1949-1952.
- [24] A. Hirano-Iwata, A. Oshima, T. Nasu, T. Taira, Y. Kimura, M. Niwano, Stable lipid bilayers based on micro- and nano-fabrication, Supramolecular Chemistry, 22 (2010) 406-412.

- [25] S. Kresak, T. Hianik, R.L.C. Naumann, Giga-seal solvent-free bilayer lipid membranes: from single nanopores to nanopore arrays, Soft Matter, 5 (2009) 4021-4032.
- [26] R.C. Murdock, L. Braydich-Stolle, A.M. Schrand, J.J. Schlager, S.M. Hussain, Characterization of nanomaterial dispersion in solution prior to In vitro exposure using dynamic light scattering technique, Toxicological Sciences, 101 (2008) 239-253.
- [27] I. Firkowska, S. Giannona, G. Gursky, A. Nikitin, A. Surovaya, N. Kasyanenko, D. Afanasieva, G.B. Khomutov, Y. Nechipurenko, S. Grokhovsky, Y.M. Yevdokimov, D. Cai, K. Kempa, Z. Ren, S. Penadés, J.M.d.l. Fuente, L.M. Liz-Marzán, J. Pérez-Juste, M.J.R. Vázquez, J. Rivas, B. Ballou, L.A. Ernst, S. Andreko, D.V. Andreeva, G.B. Sukhorukov, A.A. Yaroslavov, M.V. Kitaeva, V.V. Klechkovskaya, V.V. Volkov, K. Kempa, Nanomaterials for application in medicine and biology, Springer Netherlands, 2008.
- [28] R. Naumann, S.M. Schiller, F. Giess, B. Grohe, K.B. Hartman, I. Kärcher, I. Köper, J. Lübben, K. Vasilev, W. Knoll, Tethered Lipid Bilayers on Ultraflat Gold Surfaces, Langmuir, 19 (2003) 5435-5443.
- [29] L. Becucci, M.R. Moncelli, R. Naumann, R. Guidelli, Potassium ion transport by valinomycin across a Hg-supported lipid bilayer, J Am Chem Soc, 127 (2005) 13316-13323.
- [30] C. Steinem, A. Janshoff, H.J. Galla, M. Sieber, Impedance analysis of ion transport through gramicidin channels incorporated in solid supported lipid bilayers, Bioelectrochemistry and Bioenergetics, 42 (1997) 213-220.
- [31] A.E. Vallejo, C.A. Gervasi, Impedance analysis of ion transport through gramicidin channels in supported lipid bilayers, Bioelectrochemistry, 57 (2002) 1-7.
- [32] J.W. Robertson, M.G. Friedrich, A. Kibrom, W. Knoll, R.L. Naumann, D. Walz, Modeling ion transport in tethered bilayer lipid membranes. 1. Passive ion permeation, J Phys Chem B, 112 (2008) 10475-10482.
- [33] K. Boesze-Battaglia, R. Schimmel, Cell membrane lipid composition and distribution: implications for cell function and lessons learned from photoreceptors and platelets, J Exp Biol, 200 (1997) 2927-2936.
- [34] N. Mohandas, E. Evans, Mechanical properties of the red cell membrane in relation to molecular structure and genetic defects, Annu Rev Biophys Biomol Struct, 23 (1994) 787-818.
- [35] S.J. Marrink, A.H. de Vries, D.P. Tieleman, Lipids on the move: simulations of membrane pores, domains, stalks and curves, Biochim Biophys Acta, 1 (2009) 149-168.
- [36] N. Alexander, L. Ying, H. Wen-Che, C. Charlie, M.B. Yaghoubi, M. Corey, L. Lin, W. William, W. Paul, M.J. Andrew, D. Phillip, P.D. Jonathan, W.R. Mark, Engineered nanomaterial interactions with bilayer lipid membranes: screening platforms to assess

- nanoparticle toxicity, International Journal of Biomedical Nanoscience and Nanotechnology 3(2013) 52-83.
- [37] P. Mueller, D.O. Rudin, H. Titien, W.C. Wescott, Reconstitution of cell membrane structure in vitro and its transformation into an excitable system, Nature, 194 (1963) 979-980.
- [38] M. Montal, P. Mueller, FORMATION OF BIMOLECULAR MEMBRANES FROM LIPID MONOLAYERS AND A STUDY OF THEIR ELECTRICAL PROPERTIES, Proceedings of the National Academy of Sciences of the United States of America, 69 (1972) 3561-3566.
- [39] R.L. Robinson, A. Strickholm, Oxidized cholesterol bilayers. Dependence of electrical properties on degree of oxidation and aging, Biochimica et Biophysica Acta (BBA) Biomembranes, 509 (1978) 9-20.
- [40] E. Ralston, L.M. Hjelmeland, R.D. Klausner, J.N. Weinstein, R. Blumenthal, Carboxyfluorescein as a probe for liposome-cell interactions effect of impurities, and purification of the dye, Biochimica et Biophysica Acta (BBA)-Biomembranes, 649 (1981) 133-137.
- [41] M.J. Hope, M.B. Bally, L.D. Mayer, A.S. Janoff, P.R. Cullis, Generation of multilamellar and unilamellar phospholipid vesicles, Chemistry and Physics of Lipids, 40 (1986) 89-107.
- [42] L.D. Mayer, M.J. Hope, P.R. Cullis, Vesicles of variable sizes produced by a rapid extrusion procedure, Biochimica et Biophysica Acta (BBA)-Biomembranes, 858 (1986) 161-168.
- [43] D.A. Wyllie, Single-Channel Recording, in: W. Walz, A. Boulton, G. Baker (Eds.) Patch-Clamp Analysis, vol. 35, Humana Press, 2002, pp. 69-109.
- [44] I. Axon Instruments, The Axon guide for electrophysiology & biophysics laboratory techniques, Axon Instruments, 1993.
- [45] M. Trojanowicz, A. Mulchandani, Analytical applications of planar bilayer lipid membranes, Analytical and Bioanalytical Chemistry, 379 (2004) 347-350.
- [46] G.Z. Xu, B. Shi, E.J. McGroarty, H.T. Tien, Channel-closing activity of porins from Escherichia coli in bilayer lipid membranes, Biochim Biophys Acta, 862 (1986) 57-64.
- [47] M.R.R. de Planque, S. Aghdaei, T. Roose, H. Morgan, Electrophysiological Characterization of Membrane Disruption by Nanoparticles, Acs Nano, 5 (2011) 3599-3606.
- [48] D.P. Nikolelis, T. Hianik, U.J. Krull, Biosensors based on thin lipid films and liposomes, Electroanalysis, 11 (1999) 7-15.

- [49] B.I. Escher, R.P. Schwarzenbach, Partitioning of substituted phenols in liposomewater, biomembrane-water, and octanol-water systems, Environmental Science & Technology, 30 (1996) 260-270.
- [50] B.I. Escher, R.P. Schwarzenbach, J.C. Westall, Evaluation of liposome-water partitioning of organic acids and bases. 1. Development of a sorption model, Environmental Science & Technology, 34 (2000) 3954-3961.
- [51] M.T. Muller, A.J.B. Zehnder, B.I. Escher, Liposome-water and octanol-water partitioning of alcohol ethoxylates, Environmental Toxicology and Chemistry, 18 (1999) 2191-2198.
- [52] M. Sila, S. Au, N. Weiner, Effects of Triton X-100 concentration and incubation temperature on carboxyfluorescein release from multilamellar liposomes, Biochimica et Biophysica Acta (BBA) Biomembranes, 859 (1986) 165-170.
- [53] B. Raguse, V. Braach-Maksvytis, B.A. Cornell, L.G. King, P.D.J. Osman, R.J. Pace, L. Wieczorek, Tethered lipid bilayer membranes: Formation and ionic reservoir characterization, Langmuir, 14 (1998) 648-659.
- [54] N. Kohli, B.L. Hassler, L. Parthasarathy, R.J. Richardson, R.Y. Ofoli, R.M. Worden, I. Lee, Tethered lipid bilayers on electrolessly deposited gold for bioelectronic applications, Biomacromolecules, 7 (2006) 3327-3335.
- [55] G. Woodhouse, L. King, L. Wieczorek, B. Cornell, Kinetics of the competitive response of receptors immobilised to ion-channels which have been incorporated into a tethered lipid bilayer, Farday Discussions, 111 (1998) 247-258.
- [56] G. Krishna, J. Schulte, B.A. Cornell, R.J. Pace, P.D. Osman, Tethered Bilayer Membranes Containing Ionic Reservoirs: Selectivity and Conductance, Langmuir, 19 (2003) 2294-2305.
- [57] R. Campos, R. Kataky, Electron transport in supported and tethered lipid bilayers modified with bioelectroactive molecules, J Phys Chem B, 116 (2012) 3909-3917.
- [58] S.H. Park, S.G. Oh, J.Y. Mun, S.S. Han, Effects of silver nanoparticles on the fluidity of bilayer in phospholipid liposome, Colloids and Surfaces B-Biointerfaces, 44 (2005) 117-122.
- [59] A. Verma, F. Stellacci, Effect of Surface Properties on Nanoparticle-Cell Interactions, Small, 6 (2010) 12-21.
- [60] S.P. Hong, A.U. Bielinska, A. Mecke, B. Keszler, J.L. Beals, X.Y. Shi, L. Balogh, B.G. Orr, J.R. Baker, M.M.B. Holl, Interaction of poly(amidoamine) dendrimers with supported lipid bilayers and cells: Hole formation and the relation to transport, Bioconjugate Chemistry, 15 (2004) 774-782.

- [61] B.D. Chithrani, W.C.W. Chan, Elucidating the Mechanism of Cellular Uptake and Removal of Protein-Coated Gold Nanoparticles of Different Sizes and Shapes, Nano Letters, 7 (2007) 1542-1550.
- [62] K. Donaldson, V. Stone, C.L. Tran, W. Kreyling, P.J.A. Borm, Nanotoxicology, Occupational and Environmental Medicine, 61 (2004) 727-728.
- [63] D.B. Warheit, How meaningful are the results of nanotoxicity studies in the absence of adequate material characterization?, Toxicological Sciences, 101 (2008) 183-185.
- [64] G.J. Brug, A.L.G. van den Eeden, M. Sluyters-Rehbach, J.H. Sluyters, The analysis of electrode impedances complicated by the presence of a constant phase element, Journal of Electroanalytical Chemistry and Interfacial Electrochemistry, 176 (1984) 275-295.
- [65] Z. Lukacs, Evaluation of model and dispersion parameters and their effects on the formation of constant-phase elements in equivalent circuits, Journal of Electroanalytical Chemistry, 464 (1999) 68-75.
- [66] A.J. Bard, L.R. Faulkner, Electrochemical methods: fundamentals and applications., Second ed., John Wiley & Sons, New York, 2001.
- [67] A.J. García-Sáez, P. Schwille, Surface analysis of membrane dynamics, Biochimica et Biophysica Acta (BBA) Biomembranes, 1798 (2010) 766-776.
- [68] S.R. Jadhav, D.X. Sui, R.M. Garavito, R.M. Worden, Fabrication of highly insulating tethered bilayer lipid membrane using yeast cell membrane fractions for measuring ion channel activity, Journal of Colloid and Interface Science, 322 (2008) 465-472.
- [69] P. Borm, F.C. Klaessig, T.D. Landry, B. Moudgil, J. Pauluhn, K. Thomas, R. Trottier, S. Wood, Research strategies for safety evaluation of nanomaterials, part V: role of dissolution in biological fate and effects of nanoscale particles, Toxicol Sci, 90 (2006) 23-32.
- [70] D. Napierska, L.C.J. Thomassen, D. Lison, J.A. Martens, P.H. Hoet, The nanosilica hazard: another variable entity, Particle and Fibre Toxicology, 7 (2010).
- [71] C.E. Ashley, E.C. Carnes, G.K. Phillips, D. Padilla, P.N. Durfee, P.A. Brown, T.N. Hanna, J. Liu, B. Phillips, M.B. Carter, N.J. Carroll, X. Jiang, D.R. Dunphy, C.L. Willman, D.N. Petsev, D.G. Evans, A.N. Parikh, B. Chackerian, W. Wharton, D.S. Peabody, C.J. Brinker, The targeted delivery of multicomponent cargos to cancer cells by nanoporous particle-supported lipid bilayers, Nat Mater, 10 (2011) 389-397.
- [72] S.-H. Wu, Y. Hung, C.-Y. Mou, Mesoporous silica nanoparticles as nanocarriers, Chemical Communications, 47 (2011) 9972-9985.

- [73] Z. Li, J.C. Barnes, A. Bosoy, J.F. Stoddart, J.I. Zink, Mesoporous silica nanoparticles in biomedical applications, Chemical Society Reviews, 41 (2012) 2590-2605.
- [74] M. Ding, F. Chen, X.L. Shi, B. Yucesoy, B. Mossman, V. Vallyathan, Diseases caused by silica: mechanisms of injury and disease development, International Immunopharmacology, 2 (2002) 173-182.
- [75] C.J. Johnston, K.E. Driscoll, J.N. Finkelstein, R. Baggs, M.A. O'Reilly, J. Carter, R. Gelein, G. Oberdorster, Pulmonary chemokine and mutagenic responses in rats after subchronic inhalation of amorphous and crystalline silica, Toxicological Sciences, 56 (2000) 405-413.
- [76] M. Park, W. Annema, A. Salvati, A. Lesniak, A. Elsaesser, C. Barnes, G. McKerr, C.V. Howard, I. Lynch, K.A. Dawson, A.H. Piersma, W.H. de Jong, In vitro developmental toxicity test detects inhibition of stem cell differentiation by silica nanoparticles, Toxicology and Applied Pharmacology, 240 (2009) 108-116.
- [77] H. Zhang, D.R. Dunphy, X. Jiang, H. Meng, B. Sun, D. Tarn, M. Xue, X. Wang, S. Lin, Z. Ji, R. Li, F.L. Garcia, J. Yang, M.L. Kirk, T. Xia, J.I. Zink, A. Nel, C.J. Brinker, Processing Pathway Dependence of Amorphous Silica Nanoparticle Toxicity: Colloidal vs Pyrolytic, Journal of the American Chemical Society, 134 (2012) 15790-15804.
- [78] Y. Roiter, M. Ornatska, A.R. Rammohan, J. Balakrishnan, D.R. Heine, S. Minko, Interaction of nanoparticles with lipid membrane, Nano Letters, 8 (2008) 941-944.
- [79] S.K. Banerji, M.A. Hayes, Examination of nonendocytotic bulk transport of nanoparticles across phospholipid membranes, Langmuir, 23 (2007) 3305-3313.
- [80] N.R. Yacobi, L. DeMaio, J.S. Xie, S.F. Hamm-Alvarez, Z. Borok, K.J. Kim, E.D. Crandall, Polystyrene nanoparticle trafficking across alveolar epithelium, Nanomedicine-Nanotechnology Biology and Medicine, 4 (2008) 139-145.
- [81] C.M. Sayes, K.L. Reed, D.B. Warheit, Assessing toxicity of fine and nanoparticles: Comparing in vitro measurements to in vivo pulmonary toxicity profiles, Toxicological Sciences, 97 (2007) 163-180.
- [82] A. Villanueva, M. Canete, A.G. Roca, M. Calero, S. Veintemillas-Verdaguer, C.J. Serna, M.D. Morales, R. Miranda, The influence of surface functionalization on the enhanced internalization of magnetic nanoparticles in cancer cells, Nanotechnology, 20 (2009).
- [83] S. Patil, A. Sandberg, E. Heckert, W. Self, S. Seal, Protein adsorption and cellular uptake of cerium oxide nanoparticles as a function of zeta potential, Biomaterials, 28 (2007) 4600-4607.

- [84] O. Harush-Frenkel, N. Debotton, S. Benita, Y. Altschuler, Targeting of nanoparticles to the clathrin-mediated endocytic pathway, Biochem Biophys Res Commun, 353 (2007) 26-32.
- [85] H.J. Kitto, E. Schwartz, M. Nijemeisland, M. Koepf, J.J.L.M. Cornelissen, A.E. Rowan, R.J.M. Nolte, Post-modification of helical dipeptido polyisocyanides using the 'click' reaction, Journal of Materials Chemistry, 18 (2008) 5615-5624.
- [86] X. Lu, F. Sun, J. Wang, J. Zhong, Q. Dong, A Facile Route to Prepare Organic/Inorganic Hybrid Nanomaterials by 'Click Chemistry', Macromolecular Rapid Communications, 30 (2009) 2116-2120.
- [87] K.L. Prime, G.M. Whitesides, Self-assembled organic monolayers: model systems for studying adsorption of proteins at surfaces, Science (New York, N.Y.), 252 (1991) 1164-1167.
- [88] M.E. Orazem, B. Tribollet, Electrochemical Impedance Spectroscopy, John Wiley & Sons, Inc, 2008.
- [89] V. Freger, S. Bason, Characterization of ion transport in thin films using electrochemical impedance spectroscopy. I. Principles and theory, Journal of Membrane Science, 302 (2007) 1-9.
- [90] G. Valincius, T. Meskauskas, F. Ivanauskas, Electrochemical impedance spectroscopy of tethered bilayer membranes, Langmuir, 28 (2012) 977-990.
- [91] G.W. Milligan, M.C. Cooper, A study of standardization of variables in cluster analysis, Journal of Classification, 5 (1988) 181-204.
- [92] H. Shimodaira, An approximately unbiased test of phylogenetic tree selection, Systematic Biology, 51 (2002) 492-508.
- [93] G.M. Ljung, G.E.P. Box, On a measure of lack of fit in time series models, Biometrika, 65 (1978) 297-303.
- [94] J.P. Royston, Algorithm AS 181: The W Test for Normality, Journal of the Royal Statistical Society. Series C (Applied Statistics), 31 (1982) 176-180.
- [95] M.S. Bartlett, Properties of Sufficiency and Statistical Tests, Proceedings of the Royal Society of London. Series A, Mathematical and Physical Sciences, 160 (1937) 268-282.
- [96] G.B. Sukhorukov, E. Donath, H. Lichtenfeld, E. Knippel, M. Knippel, A. Budde, H. Möhwald, Layer-by-layer self assembly of polyelectrolytes on colloidal particles, Colloids and Surfaces A: Physicochemical and Engineering Aspects, 137 (1998) 253-266.

- [97] R. Naumann, D. Walz, S.M. Schiller, W. Knoll, Kinetics of valinomycin-mediated K+ ion transport through tethered bilayer lipid membranes, Journal of Electroanalytical Chemistry, 550 (2003) 241-252.
- [98] T.N. Tun, A.T.A. Jenkins, An electrochemical impedance study of the effect of pathogenic bacterial toxins on tethered bilayer lipid membrane, Electrochemistry Communications, 12 (2010) 1411-1415.
- [99] P.N. Yaron, B.D. Holt, P.A. Short, M. Lösche, M.F. Islam, K.N. Dahl, Single wall carbon nanotubes enter cells by endocytosis and not membrane penetration, Journal of nanobiotechnology, 9 (2011) 45.
- [100] K.J. Kwak, G. Valincius, W.C. Liao, X. Hu, X. Wen, A. Lee, B. Yu, D.J. Vanderah, W. Lu, L.J. Lee, Formation and finite element analysis of tethered bilayer lipid structures, Langmuir, 26 (2010) 18199-18208.
- [101] A.L. Plant, M. Gueguetchkeri, W. Yap, Supported phospholipid/alkanethiol biomimetic membranes: insulating properties, Biophys J, 67 (1994) 1126-1133.
- [102] J. Kang, P.A. Rowntree, Gold Film Surface Preparation for Self-Assembled Monolayer Studies, Langmuir, 23 (2007) 509-516.
- [103] G. Dutta, K. Jo, H. Lee, B. Kim, H.Y. Woo, H. Yang, Time-dependent decrease in the enhanced electrocatalytic activities observed after three different pretreatments of gold electrodes, Journal of Electroanalytical Chemistry, 675 (2012) 41-46.
- [104] J.L. Goldstein, M.S. Brown, R.G. Anderson, D.W. Russell, W.J. Schneider, Receptor-mediated endocytosis: concepts emerging from the LDL receptor system, Annual review of cell biology, 1 (1985) 1-39.
- [105] S.R. Jadhav, A.J. Needler, R.M. Worden, Interaction of polyamidoamine dendrimers with glassy carbon supported bilayer lipid membranes, in: NSTI Nanotech, vol. 1, Boston, 2008, pp. 336-339.
- [106] S.P. Hong, P.R. Leroueil, E.K. Janus, J.L. Peters, M.M. Kober, M.T. Islam, B.G. Orr, J.R. Baker, M.M.B. Holl, Interaction of polycationic polymers with supported lipid bilayers and cells: Nanoscale hole formation and enhanced membrane permeability, Bioconjugate Chemistry, 17 (2006) 728-734.
- [107] J.M. Chen, J.A. Hessler, K. Putchakayala, B.K. Panama, D.P. Khan, S. Hong, D.G. Mullen, S.C. DiMaggio, A. Som, G.N. Tew, A.N. Lopatin, J.R. Baker, M.M.B. Holl, B.G. Orr, Cationic Nanoparticles Induce Nanoscale Disruption in Living Cell Plasma Membranes, Journal of Physical Chemistry B, 113 (2009) 11179-11185.
- [108] H.C. Tian, J. Zhou, B. Qiao, Y. Liu, J.M. Xia, Y.J. Yuan, Lipidome profiling of Saccharomyces cerevisiae reveals pitching rate-dependent fermentative performance, Appl Microbiol Biotechnol, 87 (2010) 1507-1516.

- [109] G.J. Mahler, M.B. Esch, E. Tako, T.L. Southard, S.D. Archer, R.P. Glahn, M.L. Shuler, Oral exposure to polystyrene nanoparticles affects iron absorption, Nat Nano, 7 (2012) 264-271.
- [110] E. Acosta, Bioavailability of nanoparticles in nutrient and nutraceutical delivery, Current Opinion in Colloid & Interface Science, 14 (2009) 3-15.
- [111] R. Singh, J.W. Lillard, Jr., Nanoparticle-based targeted drug delivery, Exp Mol Pathol, 86 (2009) 215-223.
- [112] J. McCarthy, X. Gong, D. Nahirney, M. Duszyk, M. Radomski, Polystyrene nanoparticles activate ion transport in human airway epithelial cells, Int J Nanomedicine, 6 (2011) 1343-1356.
- [113] Y. Liu, W. Li, F. Lao, L. Wang, R. Bai, Y. Zhao, C. Chen, Intracellular dynamics of cationic and anionic polystyrene nanoparticles without direct interaction with mitotic spindle and chromosomes, Biomaterials, 32 (2011) 8291-8303.
- [114] T. Xia, M. Kovochich, M. Liong, J.I. Zink, A.E. Nel, Cationic polystyrene nanosphere toxicity depends on cell-specific endocytic and mitochondrial injury pathways, ACS Nano, 2 (2008) 85-96.
- [115] N.R. Yacobi, N. Malmstadt, F. Fazlollahi, L. DeMaio, R. Marchelletta, S.F. Hamm-Alvarez, Z. Borok, K.J. Kim, E.D. Crandall, Mechanisms of alveolar epithelial translocation of a defined population of nanoparticles, Am J Respir Cell Mol Biol, 42 (2010) 604-614.
- [116] A. Negoda, K.-J. Kim, E.D. Crandall, R.M. Worden, Polystyrene nanoparticle exposure induces ion-selective pores in lipid bilayers, Biochimica et Biophysica Acta (BBA) Biomembranes, 1828 (2013) 2215-2222.
- [117] S. Alonso-Romanowski, L.M. Gassa, J.R. Vilche, An investigation by EIS of gramicidin channels in bilayer lipid membranes, Electrochimica Acta, 40 (1995) 1561-1567.
- [118] E. Sackmann, Supported Membranes: Scientific and Practical Applications, Science, 271 (1996) 43-48.
- [119] P.R. Leroueil, S.Y. Hong, A. Mecke, J.R. Baker, B.G. Orr, M.M.B. Holl, Nanoparticle interaction with biological membranes: Does nanotechnology present a janus face?, Accounts of Chemical Research, 40 (2007) 335-342.
- [120] H.J. Johnston, M. Semmler-Behnke, D.M. Brown, W. Kreyling, L. Tran, V. Stone, Evaluating the uptake and intracellular fate of polystyrene nanoparticles by primary and hepatocyte cell lines in vitro, Toxicol Appl Pharmacol, 242 (2010) 66-78.

- [121] M.M. Angrish, A.D. Jones, J.R. Harkema, T.R. Zacharewski, Aryl hydrocarbon receptor-mediated induction of Stearoyl-CoA desaturase 1 alters hepatic fatty acid composition in TCDD-elicited steatosis, Toxicol Sci, 124 (2011) 299-310.
- [122] Y. Tu, M. Lv, P. Xiu, T. Huynh, M. Zhang, M. Castelli, Z. Liu, Q. Huang, C. Fan, H. Fang, R. Zhou, Destructive extraction of phospholipids from Escherichia coli membranes by graphene nanosheets, Nat Nano, 8 (2013) 594-601.
- [123] B.W. Ninham, Long-range vs. short-range forces. The present state of play, The Journal of Physical Chemistry, 84 (1980) 1423-1430.
- [124] R. Lipowsky, H.-G. Döbereiner, Vesicles in contact with nanoparticles and colloids Europhysics Letters, 43 (1998) 6.
- [125] A.H. Bahrami, M. Raatz, J. Agudo-Canalejo, R. Michel, E.M. Curtis, C.K. Hall, M. Gradzielski, R. Lipowsky, T.R. Weikl, Wrapping of nanoparticles by membranes, Advances in Colloid and Interface Science, 208 (2014) 214-224.
- [126] M. Deserno, W.M. Gelbart, Adhesion and Wrapping in Colloid–Vesicle Complexes, The Journal of Physical Chemistry B, 106 (2002) 5543-5552.
- [127] M. Deserno, T. Bickel, Wrapping of a spherical colloid by a fluid membrane, Europhys. Lett., 62 (2003) 767-774.
- [128] T. Cassier, A. Sinner, A. Offenhäuser, H. Möhwald, Homogeneity, electrical resistivity and lateral diffusion of lipid bilayers coupled to polyelectrolyte multilayers, Colloids and Surfaces B: Biointerfaces, 15 (1999) 215-225.
- [129] B. Wang, L. Zhang, S.C. Bae, S. Granick, Nanoparticle-induced surface reconstruction of phospholipid membranes, Proceedings of the National Academy of Sciences, 105 (2008) 18171-18175.
- [130] H. Schindler, Planar lipid-protein membranes: strategies of formation and of detecting dependencies of ion transport functions on membrane conditions, Methods Enzymol., 171 (1989) 225-253.
- [131] M.J. Snowden, B. Vincent, The temperature-controlled flocculation of crosslinked latex particles, Journal of the Chemical Society, Chemical Communications, (1992) 1103-1105.
- [132] M.Y. Lin, H.M. Lindsay, D.A. Weitz, R.C. Ball, R. Klein, P. Meakin, Universal reaction-limited colloid aggregation, Phys Rev A, 41 (1990) 2005-2020.
- [133] M.Y. Lin, H.M. Lindsay, D.A. Weitz, R. Klein, R.C. Ball, P. Meakin, Universal diffusion-limited colloid aggregation, Journal of Physics-Condensed Matter, 2 (1990) 3093-3113.

- [134] R.A. Lauten, A.-L. Kjøniksen, B. Nyström, Colloid Polymer Interactions and Aggregation in Aqueous Mixtures of Polystyrene Latex, Sodium Dodecyl Sulfate, and a Hydrophobically Modified Polymer: A Dynamic Light Scattering Study, Langmuir, 17 (2001) 924-930.
- [135] M.J. Madou, From MEMS to Bio-MEMS and Bio-NEMS: Manufacturing Techniques and Applications, III ed., CRC Press 2011.
- [136] A. Mecke, I.J. Majoros, A.K. Patri, J.R. Baker, M.M.B. Holl, B.G. Orr, Lipid bilayer disruption by polycationic polymers: The roles of size and chemical functional group, Langmuir, 21 (2005) 10348-10354.
- [137] A. Loidl-Stahlhofen, T. Hartmann, M. Schottner, C. Rohring, H. Brodowsky, J. Schmitt, J. Keldenich, Multilamellar liposomes and solid-supported lipid membranes (TRANSIL): Screening of lipid-water partitioning toward a high-throughput scale, Pharmaceutical Research, 18 (2001) 1782-1788.
- [138] J. Chen, J.A. Hessler, K. Putchakayala, B.K. Panama, D.P. Khan, S. Hong, D.G. Mullen, S.C. DiMaggio, A. Som, G.N. Tew, A.N. Lopatin, J.R. Baker, M.M.B. Holl, B.G. Orr, Cationic Nanoparticles Induce Nanoscale Disruption in Living Cell Plasma Membranes, The Journal of Physical Chemistry B, 113 (2009) 11179-11185.
- [139] Y. Huang, Y. Liu, B.L. Hassler, R.M. Worden, A.J. Mason, A Protein-Based Electrochemical Biosensor Array Platform for Integrated Microsystems, Biomedical Circuits and Systems, IEEE Transactions on, 7 (2013) 43-51.
- [140] M. Trojanowicz, Miniaturized biochemical sensing devices based on planar bilayer lipid membranes, Fresenius J Anal Chem, 371 (2001) 246-260.
- [141] C. Stagni, C. Guiducci, L. Benini, B. Ricco, S. Carrara, B. Samori, C. Paulus, M. Schienle, M. Augustyniak, R. Thewes, CMOS DNA Sensor Array With Integrated A/D Conversion Based on Label-Free Capacitance Measurement, Solid-State Circuits, IEEE Journal of, 41 (2006) 2956-2964.
- [142] S. Cosnier, Biomolecule immobilization on electrode surfaces by entrapment or attachment to electrochemically polymerized films. A review, Biosens Bioelectron, 14 (1999) 443-456.
- [143] F.A. Henn, T. Thompson, Synthetic lipid bilayer membranes, Annual review of biochemistry, 38 (1969) 241-262.
- [144] P. Kim, N. Kohl, B. Hassler, N. Dotson, A. Mason, R.M. Worden, R. Ofoli, An electrochemical interface for integrated biosensors, in: Sensors, 2003. Proceedings of IEEE, vol. 2, 2003, pp. 1036-1040 Vol.1032.
- [145] C. Yang, Y. Huang, B.L. Hassler, R.M. Worden, A.J. Mason, Amperometric Electrochemical Microsystem for a Miniaturized Protein Biosensor Array, IEEE Trans. Biomedical Circ. Systems, 3 (2009) 160-168.

- [146] M.H. Criqui, R.D. Langer, D.M. Reed, Dietary alcohol, calcium, and potassium. Independent and combined effects on blood pressure, Circulation, 80 (1989) 609-614.
- [147] F.M. Sacks, L.P. Svetkey, W.M. Vollmer, L.J. Appel, G.A. Bray, D. Harsha, E. Obarzanek, P.R. Conlin, E.R. Miller, D.G. Simons-Morton, N. Karanja, P.-H. Lin, M. Aickin, M.M. Most-Windhauser, T.J. Moore, M.A. Proschan, J.A. Cutler, Effects on Blood Pressure of Reduced Dietary Sodium and the Dietary Approaches to Stop Hypertension (DASH) Diet, New England Journal of Medicine, 344 (2001) 3-10.
- [148] C. Yang, S.R. Jadhav, R.M. Worden, A.J. Mason, Compact Low-Power Impedance-to-Digital Converter for Sensor Array Microsystems, IEEE J. Solid State Circuits, 44 (2009) 2844-2855.
- [149] M. Rehák, M. Šnejdárková, M. Otto, Self-assembled lipid bilayers as a potassium sensor, Electroanalysis, 5 (1993) 691-694.
- [150] S. Paddison, Proton conduction mechanisms at low degrees of hydration in sulfonic acid-based polymer electrolyte membranes, Annual Review of Materials Research, 33 (2003) 289-319.
- [151] X. Mu, D. Rairigh, X. Liu, A.J. Mason, Rapid impedance measurement of tethered bilayer lipid membrane biosensors, Conf Proc IEEE Eng Med Biol Soc, 9 (2011) 6091188.
- [152] J. Liu, A.J. Hopfinger, Identification of possible sources of nanotoxicity from carbon nanotubes inserted into membrane bilayers using membrane interaction quantitative structure--activity relationship analysis, Chem Res Toxicol, 21 (2008) 459-466.
- [153] R.L. Robinson, A. Strickholm, Oxidized cholesterol bilayers. Dependence of electrical properties on degree of oxidation and aging, Biochim Biophys Acta, 509 (1978) 9-20.
- [154] C. Danelon, J.B. Perez, C. Santschi, J. Brugger, H. Vogel, Cell membranes suspended across nanoaperture arrays, Langmuir, 22 (2006) 22-25.
- [155] S. Sofou, J.L. Thomas, Stable adhesion of phospholipid vesicles to modified gold surfaces, Biosensors and Bioelectronics, 18 (2003) 445-455.
- [156] X.J. Han, A. Studer, H. Sehr, I. Geissbuhler, M. Di Berardino, F.K. Winkler, L.X. Tiefenauer, Nanopore arrays for stable and functional free-standing lipid bilayers, Advanced Materials, 19 (2007) 4466-4470.
- [157] W. Romer, C. Steinem, Impedance analysis and single-channel recordings on nanoblack lipid membranes based on porous alumina, Biophysical Journal, 86 (2004) 955-965.

- [158] A. Studer, X. Han, F.K. Winkler, L.X. Tiefenauer, Formation of individual protein channels in lipid bilayers suspended in nanopores, Colloids Surf B Biointerfaces, 73 (2009) 325-331.
- [159] C.E. Musol, SIMULATION STUDY OF LIPID BILAYER/NANOPARTICLE INTERACTIONS, in: Physics, vol. PhD, Michigan State University, 2013.
- [160] S. Nangia, R. Sureshkumar, Effects of Nanoparticle Charge and Shape Anisotropy on Translocation through Cell Membranes, Langmuir, 28 (2012) 17666-17671.
- [161] J.B. Klauda, R.M. Venable, J.A. Freites, J.W. O'Connor, D.J. Tobias, C. Mondragon-Ramirez, I. Vorobyov, A.D. MacKerell, Jr., R.W. Pastor, Update of the CHARMM all-atom additive force field for lipids: validation on six lipid types, J Phys Chem B, 114 (2010) 7830-7843.
- [162] B. Jojart, T.A. Martinek, Performance of the general amber force field in modeling aqueous POPC membrane bilayers, J Comput Chem, 28 (2007) 2051-2058.
- [163] D. Poger, W.F. Van Gunsteren, A.E. Mark, A new force field for simulating phosphatidylcholine bilayers, J Comput Chem, 31 (2010) 1117-1125.
- [164] D.P. Tieleman, The molecular basis of electroporation, BMC Biochem, 5 (2004) 10.
- [165] M. Tarek, Membrane electroporation: a molecular dynamics simulation, Biophys J, 88 (2005) 4045-4053.
- [166] V.V. Ginzburg, S. Balijepailli, Modeling the thermodynamics of the interaction of nanoparticles with cell membranes, Nano Letters, 7 (2007) 3716-3722.
- [167] X. Jiang, E.B. Vogel, M.R. Smith, G.L. Baker, "Clickable" Polyglycolides: Tunable Synthons for Thermoresponsive, Degradable Polymers, Macromolecules, 41 (2008) 1937-1944.
- [168] I.R. Cooke, K. Kremer, M. Deserno, Tunable generic model for fluid bilayer membranes, Physical Review E, 72 (2005) 011506.
- [169] H.T. Tien, A.L. Ottova, The lipid bilayer concept and its experimental realization: from soap bubbles, kitchen sink, to bilayer lipid membranes, Journal of Membrane Science, 189 (2001) 83-117.
- [170] A.R. Blythe, Electrical resistivity measurements of polymer materials, Polymer Testing, 4 (1984) 195-209.
- [171] Y. Liu, R.M. Worden, Size dependent disruption of tethered lipid bilayers by functionalized polystyrene nanoparticles, Biochimica et Biophysica Acta (BBA) Biomembranes, In press.

- [172] Y. Yu, S. Granick, Pearling of Lipid Vesicles Induced by Nanoparticles, Journal of the American Chemical Society, 131 (2009) 14158-14159.
- [173] L.M. Estronca, M.J. Moreno, W.L. Vaz, Kinetics and thermodynamics of the association of dehydroergosterol with lipid bilayer membranes, Biophys J, 93 (2007) 4244-4253.
- [174] K. Eyer, F. Paech, F. Schuler, P. Kuhn, R. Kissner, S. Belli, P.S. Dittrich, S.D. Kramer, A liposomal fluorescence assay to study permeation kinetics of drug-like weak bases across the lipid bilayer, J Control Release, 173 (2014) 102-109.
- [175] T. Ruiz-Herrero, E. Velasco, M.F. Hagan, Mechanisms of Budding of Nanoscale Particles through Lipid Bilayers, The Journal of Physical Chemistry B, 116 (2012) 9595-9603.
- [176] A.F. Xie, R. Yamada, A.A. Gewirth, S. Granick, Materials science of the gel to fluid phase transition in a supported phospholipid bilayer, Phys Rev Lett, 89 (2002) 21.